Design and Synthesis of Lanthanide Single-Molecule Magnets Using the Schiff Base Approach

By

Thomas Lacelle

Thesis Submitted to the Faculty of Graduate and Postdoctoral Studies in partial fulfillment of the requirements for the Master of Science degree in Chemistry

Department of Chemistry and Biomolecular Sciences

Faculty of Science

University of Ottawa

Abstract:

Single-Molecule Magnets (SMMs) are discrete molecules that exhibit slow relaxation of magnetization. Unlike conventional magnets that rely on the long range magnetic ordering in the form of domains, these molecules act as magnets independently, that is without the influence of neighbouring molecules. SMMs have intrigued physicists and chemists alike for over twenty years with their potential future applications in data storage quantum computing, and with this communal interest there has been significant collaboration between the two fields of research. SMMs have brought forth an opportunity for coordination chemists to muster their creativity and synthetic expertise in the rational design and development of these magnetic materials. From these new and fascinating compounds, both experimental and theoretical physicists have sought to develop and refine our understanding of the aspects of these molecular magnets in order to improve their performance at higher temperatures.

In this work, new topologies for lanthanide complexes are explored using a novel Schiff base ligand. The magnetic properties of dinuclear, tetranuclear and octanuclear lanthanide complexes are discussed and correlated to their structural properties. The rational design of tetrazine-based Schiff base ligands for magnetic studies is also discussed in hopes of developing high performance SMMs.

Acknowledgements:

First and foremost I would like to thank Professor Muralee Murugesu for taking me on as a student and giving me this opportunity to further my skills as a synthetic chemist and to contribute to the field of molecular magnetism. I would like to thank both Ilia Korobkov and Bulat Gabidullin for their crystallographic expertise as well as Dr. Wolfgang Wernsdorfer and his postdoctoral fellow Yanhua Lan for performing the micro-SQUID measurements. I would also like to thank members of the Murugesu group, new and old, for all their support and time spent together. Being surrounded by such wise and ambitious colleagues helped me find passion in my work. Over the course of these two years I have made friends from all across the department of chemistry. The graduate students here show such comradery and my experience with them has been invaluable. I hope that the friendships I have made here at the University of Ottawa will last throughout my entire lifetime.

Table of Contents

List of Abbreviations (in order of appearance):

SMM Single-Molecule Magnet

χ_{obs} observed susceptibility

χ_{para} paramagnetic susceptibility

χ_{dia} diamagnetic susceptibility

N Avagadro's number

g Landé g factor

β Bohr Magneton

k Boltzmann's constant

T Temperature

S Spin ground state

C Curie constant

θ Weiss constant

M Magnetization

E_n Energy level

H Applied magnetic field

J Magnetic exchange coupling constant

S_T Total spin

L Total orbital angular momentum quantum number

J Total angular momentum quantum number

m_J energy state for mixed spin and orbital angular momentum

SQUID Superconducting Quantum Interference Device

DC Direct current

AC Alternating current

χ' In-phase susceptibility

χ" Out-of-phase susceptibility

φ Phase shift

τ Relaxation time

m_s spin energy state

EPR Electron Paramagnetic Resonance

ZFS Zero-Field Splitting

D Axial Zero-Field Splitting Parameter

E Rhombic Zero-Field Splitting Parameter

QTM Quantum Tunneling of the Magnetization

SIM Single-Ion Magnet

IEDDA Inverse-Electron-Demand Diels Alder

K_c Comproportionation constant

U_{eff} Energy barrier

τ_0 Pre-exponential factor

FTIR Fourier Transform Infrared Spectroscopy

ATR Attenuated Total Reflectance

NMR Nuclear Magnetic Resonance

δ Chemical shift

CCDC Cambridge Crystallographic Data Center

ν Frequency

χ_s Adiabatic susceptibility

χ_T Isothermal susceptibility

α Relaxation time distribution parameter

XRPD X-Ray Powder Diffraction

Chapter 1: Introduction

1.1 Principles of Magnetism. The basic principles of magnetism have been extensively studied and can be found in the early works of Olivier Kahn and John Hasbrouck Van Vleck.[1] While there are multiple subcategories of magnetic behaviour there are two basic types of magnetism: paramagnetism and diamagnetism. Paramagnetism occurs in materials which possess a net spin and/or orbital angular momentum, which most often arises from unpaired electrons. In the presence of a magnetic field paramagnetic materials will align their magnetic moments parallel to the magnetic field vector. When this external magnetic field is removed, the paramagnetic material loses this magnetic ordering and reverts to its disordered state. Diamagnetism occurs in all materials as it originates from the paired electrons within the material. Application of a magnetic field to a diamagnetic material induces a magnetic field opposing the applied field, resulting in the material being repelled by the applied field. The susceptibility of diamagnetic materials to magnetic fields is orders of magnitude lower than that of paramagnetic materials. When the magnetic susceptibility of a paramagnetic compound is measured, the diamagnetic susceptibility can be approximated using Pascal's constants and subtracted from the observed susceptibility to obtain the paramagnetic susceptibility of the material:

$$\chi_{obs} = \chi_{para} + \chi_{dia} \qquad (Eq\ 1.1)$$

1.2 Magnetic Interactions. Below a certain temperature there are three types of magnetic interactions that can occur in materials: ferromagnetism, antiferromagnetism and ferrimagnetism (Figure 1.1). Materials that exhibit ferromagnetism retain the alignment of their magnetic moment induced by an applied field even when the applied field is removed. This is the phenomenon that is responsible for permanent magnets. Materials that exhibit antiferromagnetism have their magnetic moments

antiparallel to each other such that there is no net magnetic moment. Ferrimagnetism, much like antiferromagnetism, occurs when a material has antiparallel alignment of magnetic moments, but these moments differ in magnitude. This results in a net magnetic moment in relation to ferromagnetism. The temperature at which ferromagnets and ferrimagnets can no longer retain their magnetization is known as the Curie temperature and the temperature at which a material no longer exhibits antiferromagnetic behaviour is known as the Néel temperature. Above these temperatures each of these types of materials behave as paramagnets.

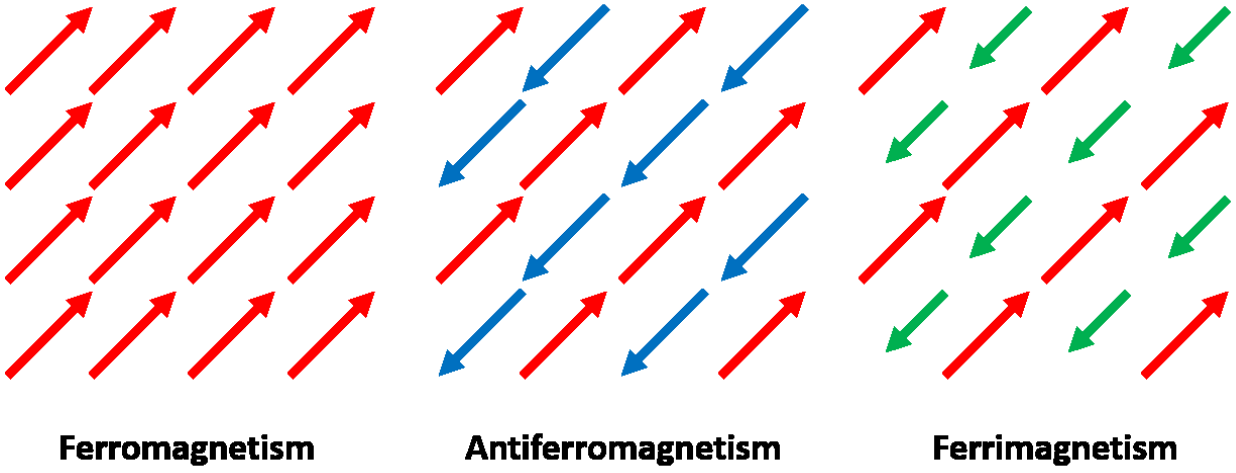

Figure 1.1. Types of magnetic interactions

1.3 Curie-Weiss Law. The magnetic susceptibility of materials is inversely proportional to temperature. The rate at which the magnetic susceptibility increases with decreasing temperature is expressed through the Curie Law:

$$\chi = \frac{Ng^2\beta^2}{3kT}S(S+1) = \frac{C}{T} \qquad (Eq\ 1.2)$$

where χ is the molar susceptibility, N is Avogadro's number, g is the Landé g factor, β is the Bohr magneton, k is Boltzmann's constant, T is the absolute temperature, S is the spin ground state and C is

the Curie constant. In order to represent magnetic interactions (i.e. ferromagetism or antiferromagnetism) an additional parameter θ is introduced which is known as the Weiss constant. When the value of θ is positive a ferromagnetic interaction is present. When θ is negative an antiferromagnetic interaction is present. By implementing this new term we arrive at the Curie-Weiss law:

$$\chi = \frac{Ng^2\beta^2}{3kT} S(S+1) \frac{1}{T-\theta} = \frac{C}{T-\theta} \qquad (Eq\ 1.3)$$

1.4 The van Vleck Equation. In order to model the magnetic susceptibility of a compound based on the populations of thermal excited states the van Vleck equation is used. To derive the van Vleck equation we first start with the general equation for magnetization, which is expressed as the rate of change of spin state energies, E, with respect to applied magnetic field, H:

$$M = \frac{\delta E}{\delta H} \qquad (Eq\ 1.4)$$

In order to obtain a weighted distribution for the occupied energy levels, E_n, the Boltzmann distribution is implemented:

$$M = \frac{N \sum_n \left(-\frac{\delta E_n}{\delta H}\right) e^{\left(-\frac{E_n}{kT}\right)}}{\sum_n e^{\left(-\frac{E_n}{kT}\right)}} \qquad (Eq\ 1.5)$$

In the presence of weak magnetic fields the energy levels can be represented in the form of a power series:

$$E_n = E_n^0 + E_n^1 H + E_n^2 H^2 + \cdots + E_n^x H^x \qquad (Eq\ 1.6)$$

Here E_n^0 represents the nth energy level with no applied field. The successive terms are the first order Zeeman term, the second order Zeeman term and so on. Since the applied field is small the higher order

terms contribute successively less to the overall series. After the second and third order Zeeman terms the successive terms in the power series become negligible and so only the first three terms are considered here.

By taking the partial derivative with respect to the applied field of the first three terms we get:

$$\frac{\delta E_n}{\delta H} = E_n^1 + 2E_n^2 H \qquad (Eq\ 1.7)$$

Since the ratios of the first and second order Zeeman terms to kT are also small the exponential term can be approximated by:

$$e^{\left(-\frac{E_n}{kT}\right)} = \left(1 - \frac{E_n^1 H}{kT}\right) e^{\left(-\frac{E_n^0}{kT}\right)} \qquad (Eq\ 1.8)$$

Substitution of Eq. 1.7 and Eq. 1.8 into Eq. 1.5 we obtain:

$$M = \frac{N \sum_n (-E_n^1 - 2E_n^2 H)\left(1 - \frac{E_n^1 H}{kT}\right) e^{\left(-\frac{E_n^0}{kT}\right)}}{\sum_n \left(1 - \frac{E_n^1 H}{kT}\right) e^{\left(-\frac{E_n^0}{kT}\right)}} \qquad (Eq\ 1.9)$$

Under zero applied field $\sum_n E_n^1 e^{\left(-\frac{E_n^0}{kT}\right)} = 0$. By dividing each side by the applied field an expression for the molar susceptibility is obtained, formally known as the van Vleck equation:

$$\chi = \frac{M}{H} = \frac{N \sum_n \left(\frac{(E_n^1)^2}{kT} - 2E_n^2\right) e^{\left(-\frac{E_n^0}{kT}\right)}}{\sum_n e^{\left(-\frac{E_n^0}{kT}\right)}} \qquad (Eq\ 1.10)$$

In the case of a system containing two spin carriers the coupling between the two spin carriers must be accounted for in the form of the following Hamiltonian:

$$\widehat{H} = -2J(\hat{S}_1 \cdot \hat{S}_2) \qquad (Eq\ 1.11)$$

The incorporation of the exchange coupling to the van Vleck equation yields the Heisenberg-Dirac van Vleck equatio:

$$\chi = \frac{Ng^2\beta^2}{3kT}\frac{\sum S_T(S_T+1)(2S_T+1)e^{\left(\frac{J(S_T(S_T+1)-S_1(S_1+1)-S_2(S_2+1)}{kT}\right)}}{\sum(2S_T+1)e^{\left(\frac{J(S_T(S_T+1)-S_1(S_1+1)-S_2(S_2+1)}{kT}\right)}} \qquad (Eq\ 1.12)$$

Where S_T is the total spin state and S_1 and S_2 are the two spin states of the spin carriers. The Heisenberg-Dirac van Vleck equation is an important tool for modelling the magnetic susceptibility of exchange-coupled systems such as dinuclear metal complexes.

1.5 Lanthanides and Molecular Magnetism. Lanthanide ions behave very differently from transition metal ions largely due to their valence electrons being situated within the 4f orbitals. The 4f electrons are shielded by the outer 6s and 5d electrons which makes the 4f orbital energy levels relatively unperturbed by ligand field effects. This yields all of the 4f orbitals to be (almost) degenerate regardless of the coordination environment of the lanthanide ions. A consequence of this orbital degeneracy is a large, unquenched orbital angular momentum that leads to high single-ion magnetic anisotropy for most lanthanide ions. The most obvious exceptions to this phenomenon are the diamagnetic lanthanide ions: La^{III} and Lu^{III} whose 4f orbitals are completely empty and completely filled, respectively. In addition to these ions, Gd^{III} has all of its 4f orbitals half-filled, resulting in zero orbital angular momentum and an isotropic electron density distribution. The last and most interesting exception is Eu^{3+} where even though the ion possesses a non-zero spin ground state and unequally occupied 4f orbitals the spin and orbital angular momenta are equal in magnitude and cancel each other out. This ultimately results in a total angular momentum of zero and gives Eu^{III} a diamagnetic ground state. This mixing of the spin and orbital angular momentum makes the total spin angular momentum quantum number, S, a poor metric for describing the magnetic properties of lanthanides. By taking the vector sum of S and the total orbital

angular momentum quantum number, L, a quantum number representing the total angular momentum, J, is obtained:

$$J = |L - S| \; when \; orbitals \; less \; than \; half \; filled$$

$$J = |L + S| \; when \; orbitals \; greater \; than \; half \; filled$$

For an ion with total angular momentum J there are 2J+1 m_J microstates:

$$For \; Ce^{III}, J = \frac{5}{2}, m_j = -\frac{5}{2}, -\frac{3}{2}, -\frac{1}{2}, +\frac{1}{2}, +\frac{3}{2}, +\frac{5}{2}$$

The ground state electronic characteristics of all of the Ln^{III} ions are given in Table 1.1.

Table 1.1. Electronic Characteristics of the 4f ions.

Ln^{III}	Electron Configuration	Spin Angular Momentum, S	Orbital Angular Momentum, L	Total Angular Momentum, J	Ground Term Symbol, $^{2S+1}L_J$
La^{III}	$[Xe]4f^0$	0	0	0	$^1S_0$
Ce^{III}	$[Xe]4f^1$	1/2	3	5/2	$^2F_{5/2}$
Pr^{III}	$[Xe]4f^2$	1	5	4	$^3H_4$
Nd^{III}	$[Xe]4f^3$	3/2	6	9/2	$^4I_{9/2}$
Pm^{III}	$[Xe]4f^4$	2	6	4	$^5I_4$
Sm^{III}	$[Xe]4f^5$	5/2	5	5/2	$^6H_{5/2}$
Eu^{III}	$[Xe]4f^6$	3	3	0	$^7F_0$
Gd^{III}	$[Xe]4f^7$	7/2	0	7/2	$^8S_{7/2}$
Tb^{III}	$[Xe]4f^8$	3	3	6	$^7F_6$
Dy^{III}	$[Xe]4f^9$	5/2	5	15/2	$^6H_{15/2}$
Ho^{III}	$[Xe]4f^{10}$	2	6	8	$^5I_8$
Er^{III}	$[Xe]4f^{11}$	3/2	6	15/2	$^4I_{15/2}$
Tm^{III}	$[Xe]4f^{12}$	1	5	6	$^3H_6$
Yb^{III}	$[Xe]4f^{13}$	1/2	3	7/2	$^2F_{7/2}$
Lu^{III}	$[Xe]4f^{14}$	0	0	0	$^1S_0$

1.6 Magnetic Measurements. In order to assess the magnetic properties of materials the magnetic susceptibility of those materials can be measured by Superconducting Quantum Interference Device

(SQUID) magnetometry. A SQUID magnetometer is a highly sensitive instrument that detects changes in magnetic field. In a similar fashion to a classic electrical inductor, these changes in magnetic field are measured by the variation of current within a superconducting coil as the sample is passed through the coil. The sample can be cooled using compressed liquid helium to obtain temperatures as low as 1.8 K. This allows for the variable temperature measurement of magnetic susceptibility. The SQUID magnetometer can measure magnetic susceptibility in two ways: using direct current (DC) or alternating current (AC) measurements. These measurements generate a static or oscillating magnetic field in the superconducting coil, respectively. The DC measurements allow for the determination of magnetic saturation of the sample as well as the bulk susceptibility. The AC measurements probe the magnetization relaxation dynamics of the sample, giving values for both in-phase and out-of-phase magnetic susceptibility.

1.7 DC Measurements. One of the most common interpretations of magnetic susceptibility is the χT *vs.* T plot. Since magnetic susceptibility is inversely proportional to temperature it can be difficult to determine if a sample exhibits ferromagnetic or antiferromagnetic interactions based off a χ *vs.* T plot. By plotting the χT product against T the inverse dependence of χ with T is removed from the curve and deviations from paramagnetic behaviour are readily observed (Figure 1.2). In a ferromagnetic material, an upturn in the χT *vs.* T plot is observed at low temperature. Conversely, a downturn is observed in an antiferromagnetic material at low temperature.

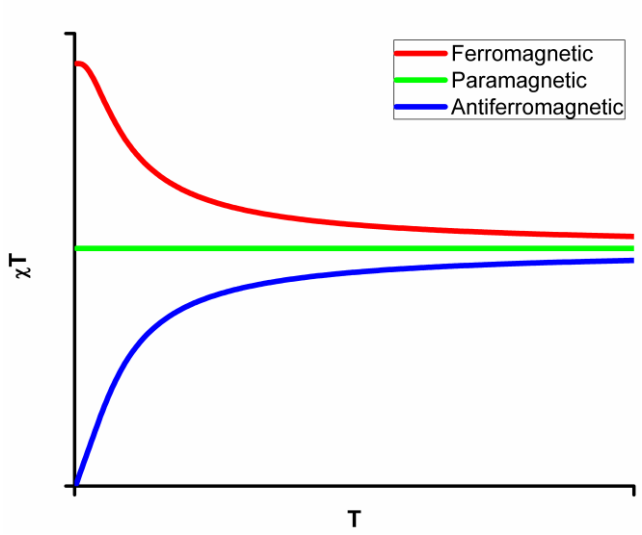

Figure 1.2. Graphical representation of magnetic interactions observed in a χT *vs.* T plot

Another common set of plots is the magnetization (M) *vs.* applied field (H) plots (Figure 1.3). From these plots the saturation of magnetization can be observed which can elucidate the spin ground state of the sample as well as the g factor based on the equation: $M = g \cdot S$. A similar plot to the M *vs.* H plot is the reduced magnetization plot or the M *vs.* H/T plot (Figure 1.3). This plot highlights any intrinsic magnetic anisotropy in the sample. In a similar fashion to the χT *vs.* T plot the temperature dependence of the magnetization is removed from the curves. If the sample is magnetically isotropic then all of the isothermal curves will overlap onto one master curve, otherwise there is non-negligible magnetic anisotropy present.

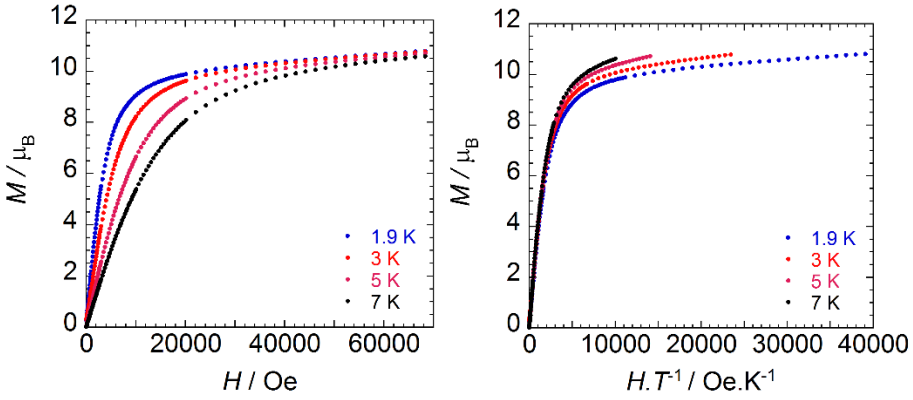

Figure 1.3. Examples of M *vs.* H (left) and M *vs.* H/T (right) plots at varying temperatures

1.8 AC measurements. During an AC measurement an oscillating magnetic field is subjected to the sample at a known frequency. The SQUID magnetometer then measures three quantities: the in-phase susceptibility (χ'), the out-of-phase susceptibility (χ'') and the phase shift (φ). χ' represents the magnetic moment in the sample that is in alignment with the oscillating magnetic field. χ'' represents the magnetic moment that lags behind the oscillating magnetic field. φ represents the degree of separation between the in-phase and out-of-phase signals based on the oscillating field frequency. Observation of temperature and frequency dependent out-of-phase susceptibility confirms remnant magnetization and slow magnetic relaxation, which is indicative of magnet-like behaviour (Figure 1.4). The ac frequencies at which the out-of-phase susceptibilities are maximized can be used to determine the relaxation time, τ.

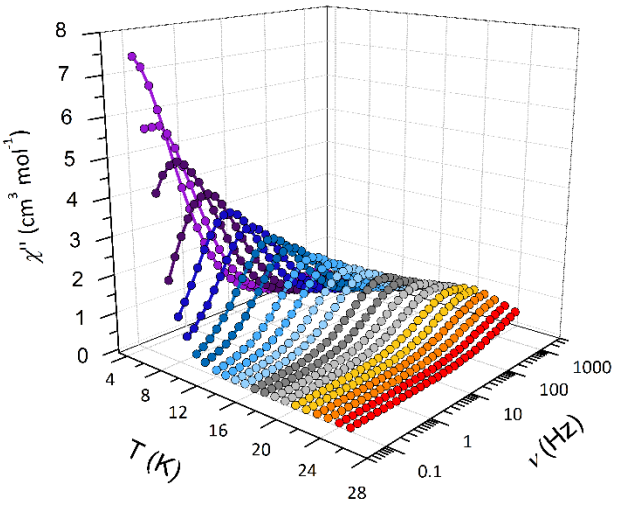

Figure 1.4. Temperature and frequency dependence of out-of-phase susceptibility observed in an SMM.

Another AC measurement that can be performed is magnetic hysteresis. After a sample is magnetized from increasing the applied magnetic field the magnetic field is reversed. If the sample behaves as magnet the retention of magnetization will result in a magnetic hysteresis loop (Figure 1.5). When the applied field reaches back to zero the value of the magnetization left over is called the remnant magnetization. The magnitude of the magnetic field required to demagnetize the magnet (i.e. M = 0) is called the coercive field.

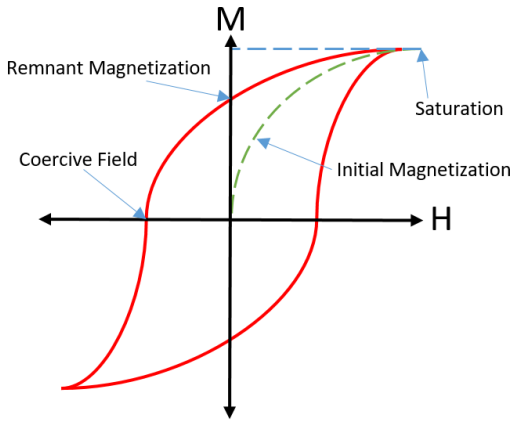

Figure 1.5. Schematic representation of magnetic hysteresis

1.9 The Zeeman Effect. With the exclusion of zero-field splitting the basics of the Zeeman Effect will now be discussed. In the absence of an applied magnetic field the m_s states in a given system are degenerate. However when a magnetic field is introduced the m_s states that are aligned with the magnetic field are lowered in energy. Conversely the m_s states that are aligned against the magnetic field are raised in energy by an equal proportion. The degree of separation between the $+m_s$ and $-m_s$ states is given by the equation:

$$E = -m_s g \beta H_0$$

Where E is the energy of the spin state, g is the Landé g factor and β is the Bohr magneton and H_0 is the applied magnetic field. A schematic diagram of the Zeeman Effect for a ½ total spin system is depicted in Figure 1.6.

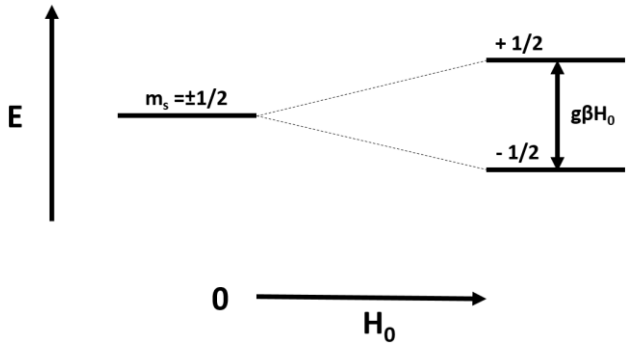

Figure 1.6. Zeeman splitting diagram for an S = ½ system

For an S = 1 system the three fold degeneracy is removed in a similar fashion to the S = ½ system but now there is an m_s = 0 state where the energy is neither raised nor lowered. This is due to the magnetic moments of the two spins cancelling each other out, resulting in no net influence from the magnetic field (Figure 1.7).

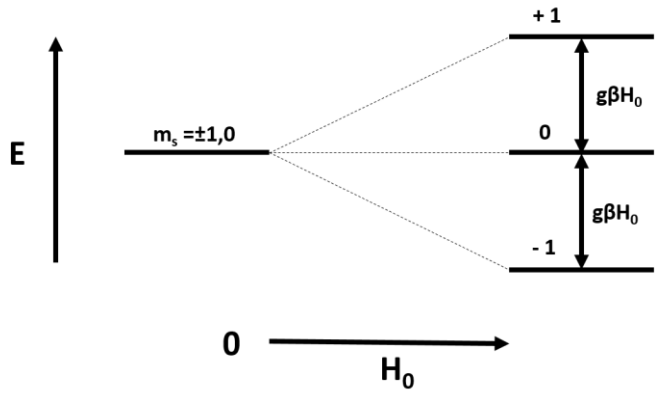

Figure 1.7. Zeeman splitting diagram for an S = 1 system

This pattern continues for the successive *S* = 3/2, 2, 5/2, 3 and 7/2 states with each state separated from the most adjacent states by $g\beta H_0$. It is important to note that the larger values of m_s will be separated further than those of smaller m_s values. As an example, Figure 1.8 shows that the m_s = +3/2 state is separated from the -3/2 state by $3g\beta H_0$ while the m_s = +1/2 states are only separated by $g\beta H_0$.

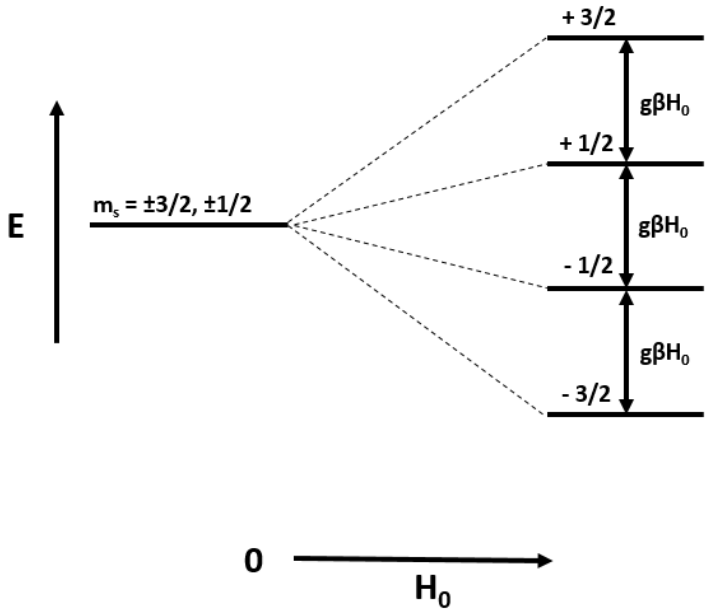

Figure 1.8. Zeeman splitting diagram for an *S* = 3/2 system

While the example given is for the splitting of the spin states for an electron the Zeeman Effect removes the degeneracy of nuclear spin states as well, which is the key operating principles in Nuclear Magnetic Resonance spectroscopy. Even systems that possess no spin angular momentum but do possess degenerate m_I states are susceptible to the Zeeman Effect since the system still possesses a magnetic moment. For this reason singlet oxygen in the $^1\Delta_g$ state gives an observable transition in an electron paramagnetic resonance (EPR) spectrum.[2]

1.10 Zero-Field Splitting. Zero-Field Splitting (ZFS) is a phenomenon that can exist in systems with S ≥ 1 where the degeneracy of spin states is lifted without the influence of an external magnetic field. Zero-Field Splitting arises from two interactions: the spin-spin coupling between unpaired electrons and the mixing of ground and excited spin states through spin-orbit coupling.[3] Zero-Field Splitting is represented by the following spin Hamiltonian[4]:

$$\hat{H} = D\left\{\hat{S}_z^2 - \frac{1}{3}S(S+1)\right\} + E\left(\hat{S}_x^2 - \hat{S}_y^2\right)$$

Where D is the "axial" ZFS parameter and E is the "rhombic" ZFS parameter. The signs of these parameters dictate how the energy of these spin states are shifted. When D is positive the energy of the non-zero $\pm m_s$ states are raised and when D is negative the energy of the non-zero $\pm m_s$ states are lowered. In the case of an integer spin system the E parameter then removes the degeneracy of each set of $\pm m_s$ states. These effects are demonstrated in Figure 1.9 for an S = 1 spin system.

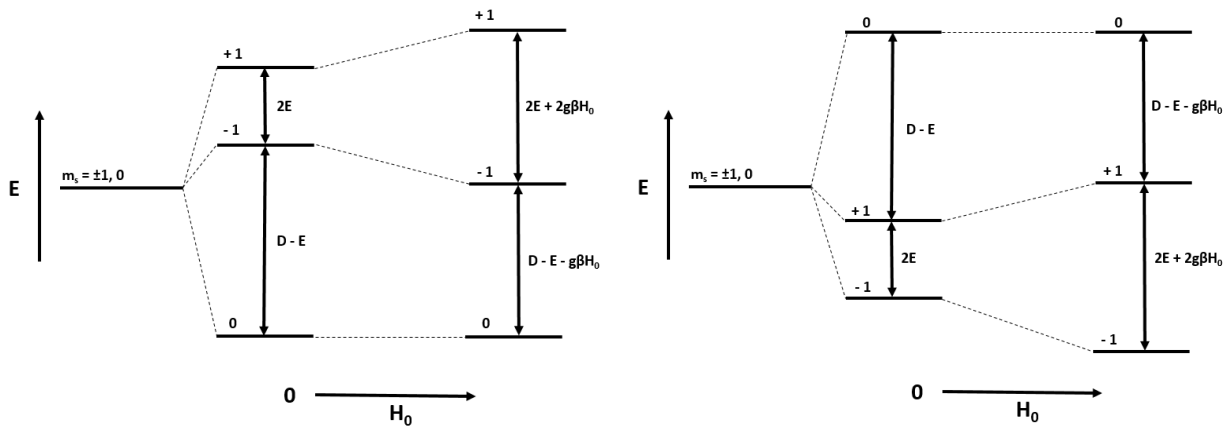

Figure 1.9. Zeeman diagrams for S= 1 spin systems incorporating ZFS where D>0, E>0 (left) and D<0, E>0, (right)

In the case of half-integer spin systems an interesting phenomenon occurs where the E parameter does not remove the degeneracy of each set of $\pm m_s$ states. This effect is a consequence of the Kramers theorem. One of the implications of the Kramers theorem is that the ground state of a system with a half-integer spin will always have at least a two-fold degeneracy regardless of symmetry, crystal field effects or spin-orbit coupling.[5] This is demonstrated in Figure 1.10 where both the ±1/2 and ±3/2 states remain at the same energy at zero field even in the presence of a non-zero E parameter. These two states are often referred to as Kramers doublets.

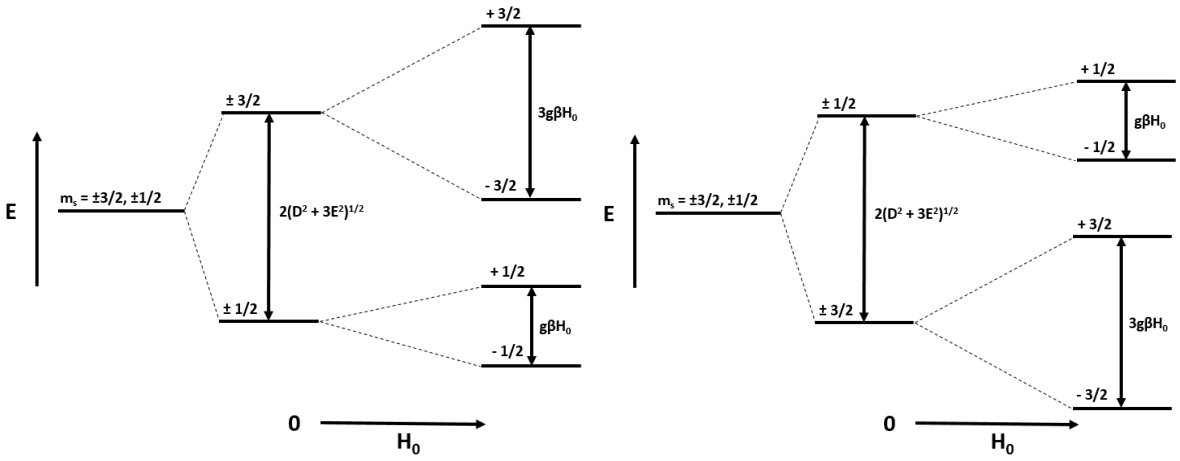

Figure 1.10. Zeeman diagrams for S= 3/2 spin systems incorporating ZFS where D>0, E>0 (left) and D<0, E>0, (right).

1.11 The Barrier for Relaxation of Magnetization. In order for a material to retain its magnetization there must exist a finite energy barrier that separates the $+M_s$ and $-M_S$ states, otherwise the spins could freely and randomly reorient themselves. The magnitude of this energy barrier has been traditionally defined as $E = |D|S^2$ for an integer spin system and $E = |D|(S^2 - \frac{1}{4})$ for a half-integer spin system, where D is the axial ZFS parameter and S is the spin ground state.[6] The barrier for magnetization reversal can be represented in the form of a double-well potential energy diagram (Figure 1.11).

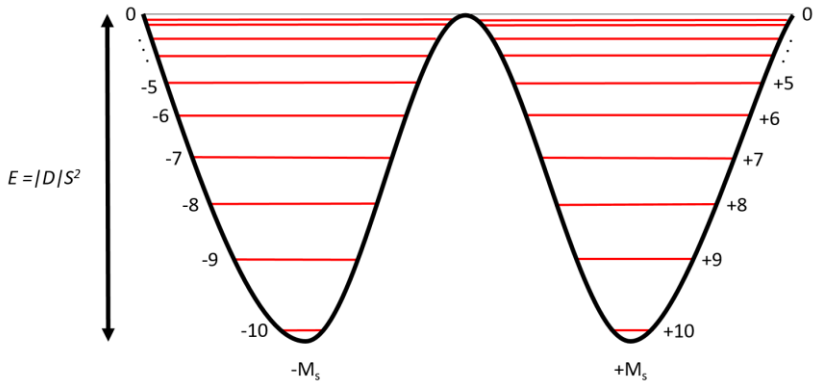

Figure 1.11. Double-well potential energy diagram for an S = 10 spin system.

When a magnetic field is applied the $-M_s$ states are stabilized and the $+M_s$ states are destabilized, which causes a shift towards the $-M_s$ states. When the magnetic field is removed more spins are in the $-M_s$ states (i.e. oriented along the applied field) than in the $+M_s$ states (i.e. oriented against the magnetic field). In order for the spins to reach equilibrium, that is for the $+M_s$ and $-M_s$ states to become equally occupied again, the spins must relax back by overcoming the energy barrier. Ideally if the energy barrier is large enough then the spins would remain in one orientation permanently. The energy barrier is responsible for the retention of magnetization in magnetic materials. It would seem intuitive then that the blocking temperature of a magnet should be directly correlated to the energy barrier for that magnet. However this is often not the case as SMMs with energy barriers on the order of hundreds of Kelvin have often been shown to have blocking temperatures of less than 2 K. One major reason for the poor correlation between these two quantities is quantum tunneling of the magnetization.

1.12 Quantum Tunneling of the Magnetization. Quantum tunneling of the magnetization (QTM) is currently one of the greatest challenges to overcome in the design of SMMs. In a similar fashion to how a particle with quantized energy levels can pass through a finite potential energy barrier and appear on the other side, the spin on an electron can transition between the $-m_s$ and $+m_s$ states due to the mixing of the electron spin wavefunctions. This allows the spins to ignore the energy barrier and essentially flip between spin states indiscriminately, causing fast relaxation and a reduced coercive field. There are two types of QTM: direct quantum tunneling and thermally-assisted quantum tunneling. As outlined in Figure 1.12, the spin could travel directly through the barrier or the spin might have to reach a thermally populated state and then cross over the barrier.

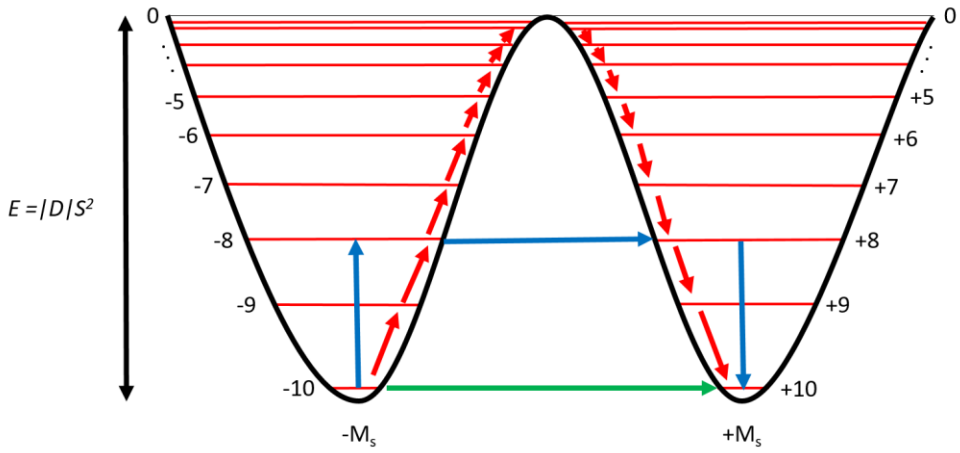

Figure 1.12. Double-well potential energy diagram depicting direct QTM (green), thermally-assisted QTM (blue) and thermal relaxation (red).

In 3d polynuclear SMMs quantum tunnelling occurs through transitions between m_s states. In the case of lanthanides the m_j states are often well separated by spin-orbit coupling and QTM occurs primarily through hyperfine interactions. These crossings in spin state are often observed in hysteresis measurements at low temperature in the form of steps (Figure 1.13).

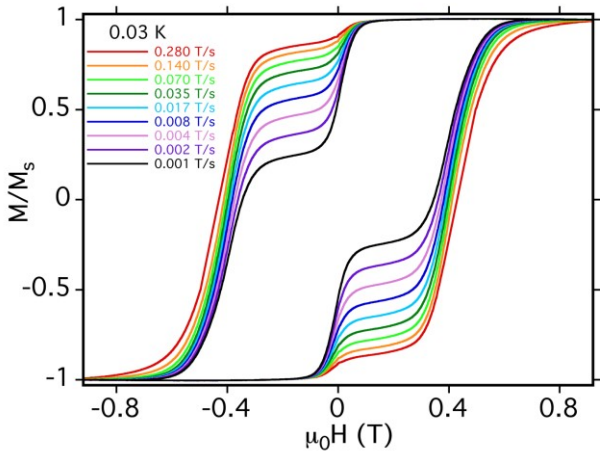

Figure 1.13. Quantum tunneling of the magnetization at zero field depicted in a magnetic hysteresis plot.

There are three strategies currently employed to minimize QTM. The first is to promote strong exchange coupling between spin centers. The second is to rely on Kramers theorem and only employ metal ions with half-integer total spin. The third is to restrict the metal ion(s) to a high symmetry environment that prevents the mixing of wavefunctions. The problem with the last approach is that even subtle vibrations of atoms will distort the symmetry of the molecule and permit transitions of spin states through vibronic coupling.

1.13 History of Single-Molecule Magnets. The first discovery of SMM behaviour was reported by Sessoli et al. in 1993,[7] which was found in a manganese cluster with the formula $[Mn_{12}O_{12}(OCMe)_{16}(H_2O)_4]$, more commonly referred to as Mn_{12} acetate (Figure 1.14). The structure consists of four tetrahedral Mn^{IV} ions surrounded by eight octahedral Mn^{III} ions. The Mn^{III} and Mn^{IV} ions are antiferromagnetically coupled to each other to give an S = 10 spin ground state. Upon removal of an applied magnetic field it was found that the Mn_{12} acetate molecule retained its magnetization, demonstrating the first magnet-like behaviour derived from a discrete molecule.

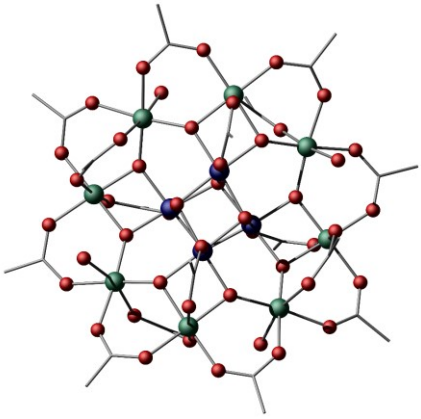

Figure 1.14. Crystal Structure of Mn_{12} acetate with oxidation states of manganese ions depicted (Ref. 7). Colour code: Blue (Mn^{IV}), Green (Mn^{III}), Red (O). Hydrogen atoms are omitted for clarity. All unfilled vertices are carbon atoms.

What came from this discovery was the idea that single molecules could be used to retain information in the form of magnetization in a similar manner to current magnetic data storage technologies. We are now approaching the fundamental limit of information density where the smallest possible unit of data storage is a single molecule. The use of SMMs for ultra-high density data storage is the ultimate goal for these materials, although their applications are not limited to this. SMMs are also being investigated for their potential in spintronic devices and next generation MRI contrast agents.[8]

Currently the largest drawback to using SMMs in devices is the temperature at which they operate. While the Mn_{12} acetate molecule exhibits slow relaxation of the magnetization the temperature at which this phenomenon is observed is below 3 K. This threshold temperature at which a molecule can no longer retain its magnetization is referred to as the blocking temperature (T_B). It became immediately apparent that in order for SMMs to become applicable to devices the blocking temperature of these materials would need to be improved.

Over the years strategies for designing high blocking temperature SMMs have progressively developed. Initial attempts to raise the blocking temperature in SMMs were based on simply increasing the spin ground state of the molecule. This lead to the rational design of polymetallic clusters possessing high degrees of nuclearity. In 2006, SMM behaviour was observed in a Mn_{19} cluster with a record-breaking spin ground state of $S = 83/2$,[9] but regardless of the enormous spin ground state magnetic hysteresis was only observed below 0.5 K, an even lower blocking temperature than that of Mn_{12} acetate. This revelation lead to the conclusion that simply having a large spin ground state was not sufficient and that the magnetic anisotropy of the spin carriers also played an equal, if not more important, role in designing high blocking temperature SMMs.

In 2003, the first single-ion magnet (SIM) was discovered with the formula [TBA][$LnPc_2$] (where TBA = tetrabutylammonium, Ln = Tb^{III} or Dy^{III}, Pc = phthalocyanine) (Figure 1.15). These complexes exhibit D_{4d} symmetry and the Tb^{III} analogue shows magnetic hysteresis up to 1.7 K.[10] In 2005, a study was conducted on these two complexes to elucidate the mechanism of quantum tunnelling of the magnetization observed in the hysteresis loop measurements.[11] The observed steps in the hysteresis were attributed to hyperfine interactions between the unpaired electrons and the spin of the lanthanide nucleus.

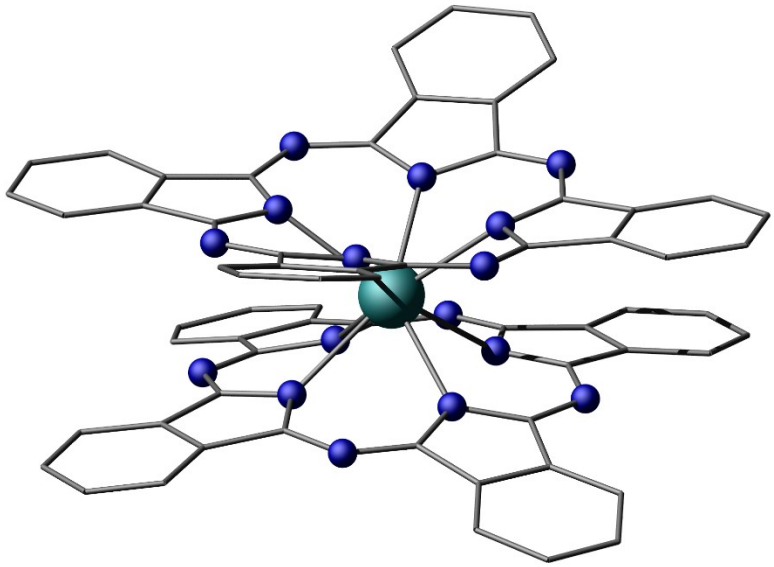

Figure 1.15. $[TbPc_2]^-$ complex (Ref. 10). Colour code: Aqua (Tb), Blue (N). Hydrogen atoms are omitted for clarity. All unfilled vertices are carbon atoms.

This study revealed how detrimental quantum tunneling of the magnetization was to the remnant magnetization of single-ion magnets. Regardless of the incredibly large barrier of 374 K this barrier was simply shortcut through the aid of hyperfine interactions.

In 2011 Rinehart et al. reported a family dinuclear lanthanide complexes bridged by a dinitrogen radical ligand of the formula $[K(18\text{-Crown-6})(THF)_2]$ $[Ln_2N_2\{N(SiMe_3)_2\}_4(THF)_2]$ (Ln = Y, Gd, Dy, Tb) (Figure 1.16).[12] The terbium analogue of the complex exhibited hysteresis up to 14 K, a new record for the blocking temperature of SMMs. This large blocking temperature was attributed to the strong exchange coupling between the Tb^{III} ion and the unpaired electron in the dinitrogen radical. This study demonstrated that exchange coupling can mitigate quantum tunneling processes at zero field. While this complex set a new precedent and sparked interest for radical-bridged SMMs, the drawback to this SMM is that the dinitrogen radical is highly reactive, making the complex incompatible with ambient aerobic conditions.

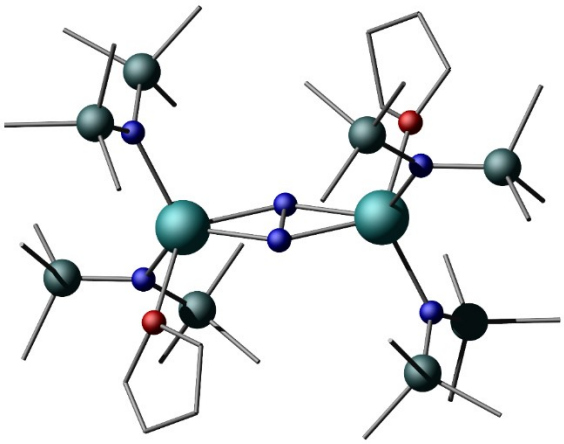

Figure 1.16. $[Tb_2N_2\{N(SiMe_3)_2\}_4(THF)_2]^-$ (Ref 12). Colour code: Aqua (Tb), Red (O), Blue (N) Aquamarine (Si). Hydrogen atoms are omitted for clarity. All unfilled vertices are carbon atoms.

In 2016, Tong and coworkers reported two sets of Dy^{III} single-ion magnets (Figure 1.17). The first set of magnets under the general formula $[Dy(Cy_3PO)_2(H_2O)_5]X_3$ (X = Cl, Br) possessed energy barriers of 472 (X = Cl) and 543 K (X = Br).[13] Magnetic hysteresis of the bromide analogue was observed up to 20 K, which is now the current record for the blocking temperature of SMMs. The second set of single-ion

magnets was reported later this year with the general formula [Dy(bbpen)X] (H_2bbpen = N,N'-bis(2-hydroxybenzyl)-N,N'-bis(2-methylpyridyl)ethylenediamine; X = Cl, Br) (Figure 1.17).[14] While the blocking temperature of these magnets were not quite as high as the previous set of SIMs, the bromide analogue not only tied the previous blocking temperature of 14 K but it also broke the record for the highest energy barrier with a value of 1025 K. The authors attributed these unprecedented magnetic properties to both the highly axial crystal field as well as the symmetry of the complexes. Both sets of compounds have slightly distorted D_{5h} symmetry in the form of a pentagonal bipyramidal coordination geometry. Subsequently, two additional pentagonal bipyramidal complexes were reported this year. Rajaraman and coworkers reported complexes of Dy^{III} and Er^{III} with the general formula $[Ln[(MePO(NHMe)_2)])_2(H_2O)_5]I_3$, where the Dy^{III} analogue possessed an energy barrier of 735 K and a blocking temperature of 12 K (Figure 1.17).[15] Winpenny and coworkers also presented a similar complex with the general formula $[Dy(O^tBu)_2(py)_5][BPh_4]$.[16] This complex has nearly doubled the current energy barrier record, set just this year, with a value of 1815 K. The rationale for the high performance for these magnets is that high-order symmetry forbids the mixing of wavefunctions, thereby suppressing the quantum tunneling of the magnetization. These findings also coincide with the theory that strong axial ligand fields with ions that have oblate electron density will generate large anisotropy and create a well-separated ground state.[17]

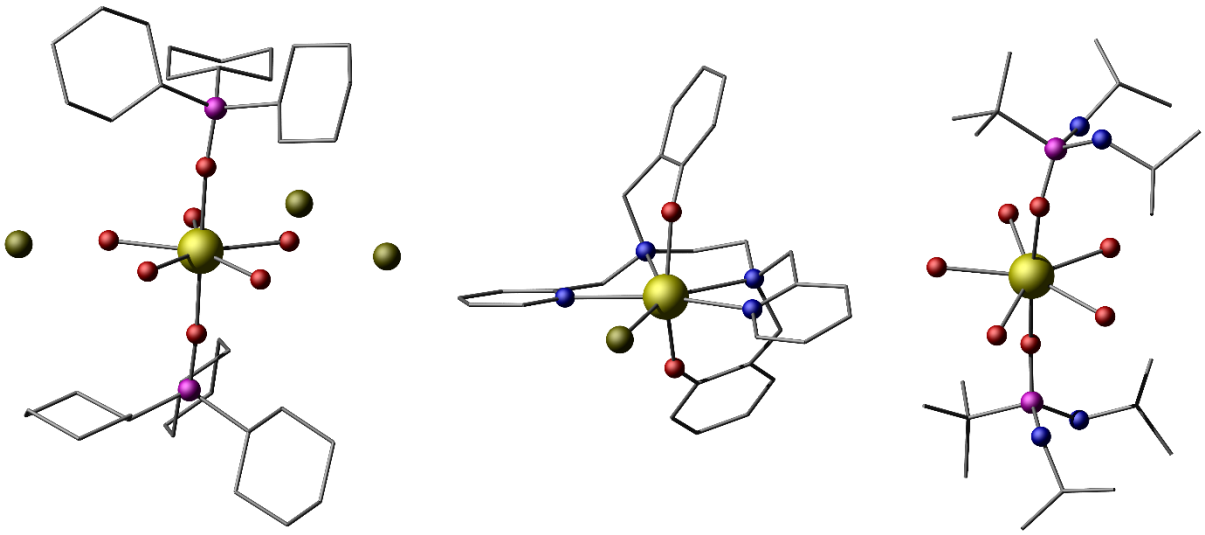

Figure 1.17. $[Dy(Cy_3PO)_2(H_2O)_5]Br_3$ (left, Ref. 13), [Dy(bbpen)Br] H_2bbpen = N,N'-bis(2-hydroxybenzyl)-N,N'-bis(2-methylpyridyl)ethylenediamine) (middle, Ref. 14) and $[Dy[(MePO(NHMe)_2)])_2(H_2O)_5]^{3+}$ (right Ref. 15). Colour code: Yellow (Dy), Red (O), Blue (N), Pink (P), Olive Green (Br). Hydrogen atoms are omitted for clarity. All unfilled vertices are carbon atoms.

From observing the literature and the history of SMMs it is clear that the quality of SMMs is determined by three main factors: high uniaxial anisotropy, strong magnetic exchange coupling and/or high local symmetry of the paramagnetic ion(s). Even though SIMs have recently shown the best performance among SMMs, their magnetic blocking is heavily reliant on symmetry and small perturbations will allow quantum tunneling to occur. Such perturbations can arise from the surface deposition of SMMs, which is a vital methodology for the implementation of SMMs into devices. So while metal ions in complexes with higher degrees of nuclearity often lack higher orders of symmetry the exchange interaction between neighbouring spins, if strong enough, can sufficiently separate the ground and excited spin states to produce high energy barriers for the relaxation of magnetization. Thus far the most promising approach for producing high energy barrier polynuclear SMMs is through radical exchange coupling with the metal ions.

1.14 The Fascinating Chemistry of 1,2,4,5-tetrazines. In order to promote radical exchange coupling an appropriate moiety must be chosen that is capable of holding an unpaired electron. One example of such a moiety is 1,2,4,5-tetrazine. Tetrazines are six-membered aromatic heterocycles with four nitrogen atoms and two carbon atoms within the conjugated ring. There are two known core-ring isomers of tetrazines that exist: 1,2,3,4-tetrazines and 1,2,4,5- tetrazines (Figure 1.18). 1,2,3,4-tetrazines have all four nitrogen atoms bonded to each other on one side of the ring while 1,2,4,5-tetrazines, the more symmetric isomer of the two, has two pairs of nitrogen atoms on opposite sides of the ring. By far the most common class of tetrazines are 1,2,4,5-tetrazines and the focus of this section will be entirely on 1,2,4,5-tetrazines. Henceforth in this work 1,2,4,5-tetrazines will be simply referred to as tetrazines.

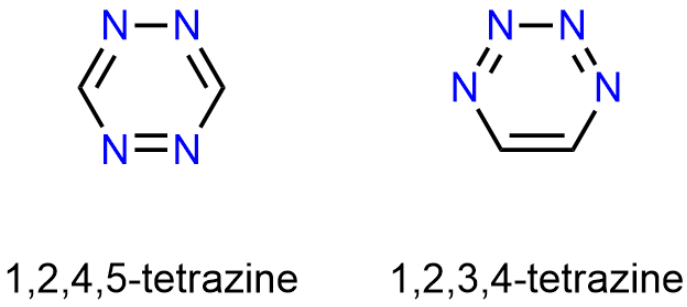

Figure 1.18. Two structural isomers of tetrazine.

Tetrazines were first discovered by Adolf Pinner in 1893 where he investigated the reactions between hydrazine and various nitriles.[18] There is no direct synthesis to tetrazines that is known. Instead the compound is always obtained by oxidizing the 1,2- or 1,4- dihydro derivatives. The most common and longest known method for synthesizing the dihydro derivatives is the Pinner synthesis or modifications thereof. This method initially involves the nucleophilic attack of the nitrile carbon with hydrazine to form amidrazones. Interestingly the mechanism for this method is still not fully understood

to this day. A mechanism for a modified synthesis was proposed by Audebert et al. entailing the use of sulfur to activate the hydrazine (Scheme 1.1).[19]

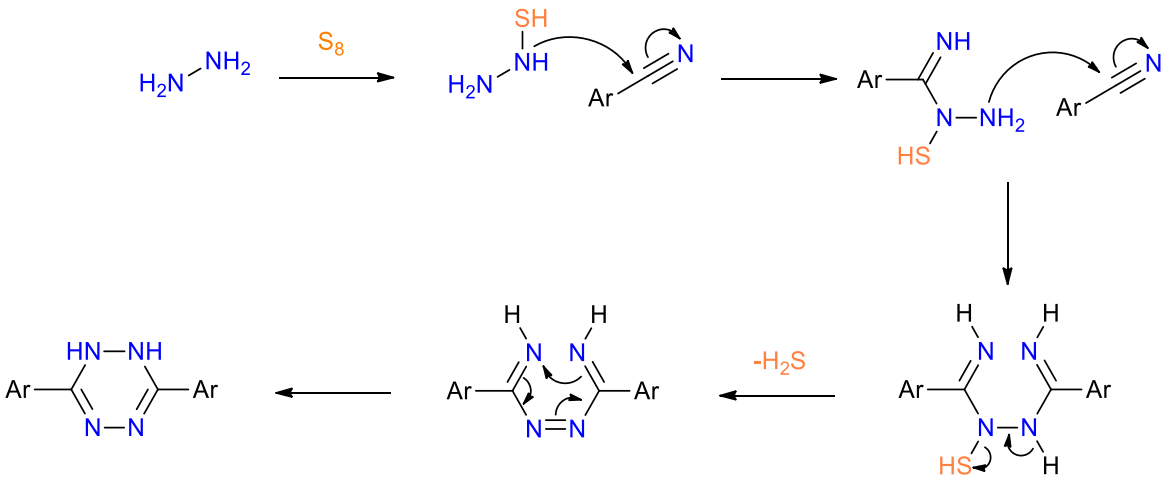

Scheme 1.1. Modified Pinner synthesis of tetrazines using sulfur.

Tetrazines possess a plethora of chemical properties that make them interesting to a wide variety of disciplines in chemistry. Many of these chemical properties arise from the highly electron-deficient π system of the tetrazine ring. The four nitrogen atoms within the ring lower the π^* orbital allowing tetrazines to be strong π-acceptors. Because of their low-lying π^* orbital tetrazines have shown prominence as electron deficient dienes in Inverse-Electron-Demand Diels-Alder (IEDDA) reactions (Scheme 1.2).[20] Such reactions often occur rapidly at room temperature in the absence of a catalyst to yield their pyridazine derivatives.

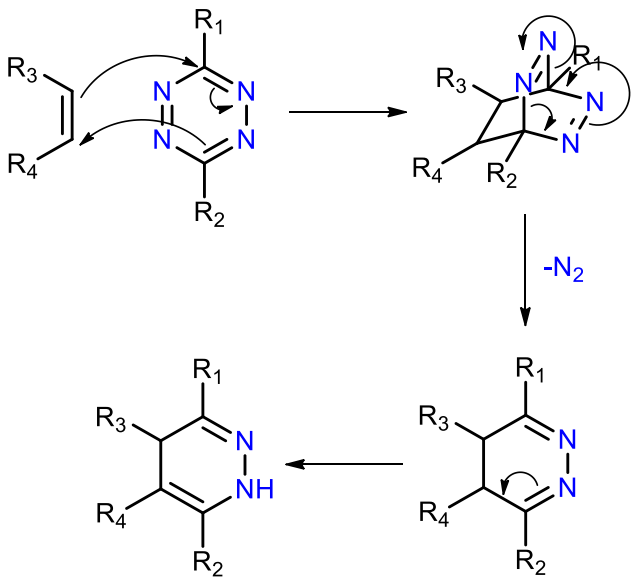

Scheme 1.2. IEDDA reactions of tetrazines.

The π-acidity associated with tetrazines has also led to the templation of supramolecular architectures through anion-π interactions. Both our group as well as Dunbar and coworkers have demonstrated the influence of anion-π interactions on the self-assembly of coordination polymers and discrete molecules respectively.[21]

Yet another consequence of the electron deficient ring is the redox activity of tetrazines. Indeed, the low-lying π^* orbital is also responsible for the facile one-electron reduction of tetrazines to form radical anions. In most cases, tetrazines exhibit a reversible one-electron reduction (typically E > -1.3 V *vs.* ferrocene) as well as a second, irreversible reduction process.[22] The irreversibility of the second reduction process is attributed to the immediate protonation of the doubly reduced tetrazine species to form 1,4-dihydro-tetrazines (Scheme 1.3).

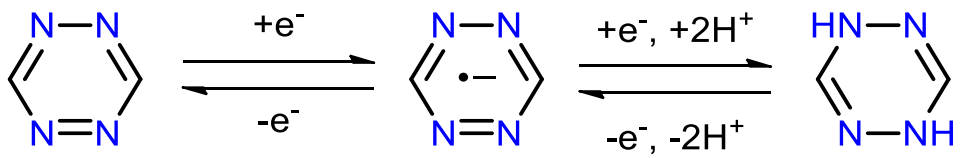

Scheme 1.3. One-electron redox processes of tetrazines

All of these unique properties of tetrazines offer great opportunity for materials scientists to explore the potential uses of these compounds. Tetrazines have already been shown to have a wide variety of applications. Such applications include, but are not limited to, energetic materials,[23] luminescence,[24] as well as bioconjugation.[25] Tetrazines have also been used quite recently by Samanta et al. for metal-free, visible light photocatalysis.[26]

The ultimate goal for this work is to explore the role of tetrazines in the design of novel magnetic materials. Due to the aforementioned redox activity, the anion radicals of tetrazines can be used as spin-bearing ligands in order to promote strong spin-spin coupling with lanthanide ions. Radical exchange coupling with lanthanides has been reported to reach up to 27 cm^{-1},[12b] but the strength of the coupling of tetrazine radicals to lanthanide ions has yet to be explored. Tetrazine radicals also possess a high degree of stability,[27] which can be represented as follows:

$$K_c = \frac{[M^{\bullet -}]}{[M^{2-}][M]} = 10^{\frac{\Delta E}{59\,mV}}$$

Where K_c is comproportionation constant and δE is the potential difference between the 0/•- and •-/2- redox couples. For tetrazines these values can be greater than 10^{20} whereas with other azine-type ligands such as 2,2'-bipyrimidine the values of K_c are often several orders of magnitude lower.[28]

1.15 Schiff Base Ligands and their Mark on Coordination Chemistry. In order to implement tetrazines into ligands in a strategic manner, the Schiff base motif was employed. Schiff bases are one of the most widely used families of organic compounds. Schiff bases were discovered by Hugo Schiff in 1864, where he published a brief paper entitled "A New Series of Organic Bases".[29] The straightforward synthesis of Schiff bases involves the nucleophilic attack of a carbonyl carbon by a primary amine (Scheme 1.4). From there a carbinolamine intermediate is formed which undergoes a protonation of the OH moiety. This generates a good leaving group which results in the loss of a water molecule. The remaining iminium cation is deprotonated by a base to yield the desired Schiff base compound.

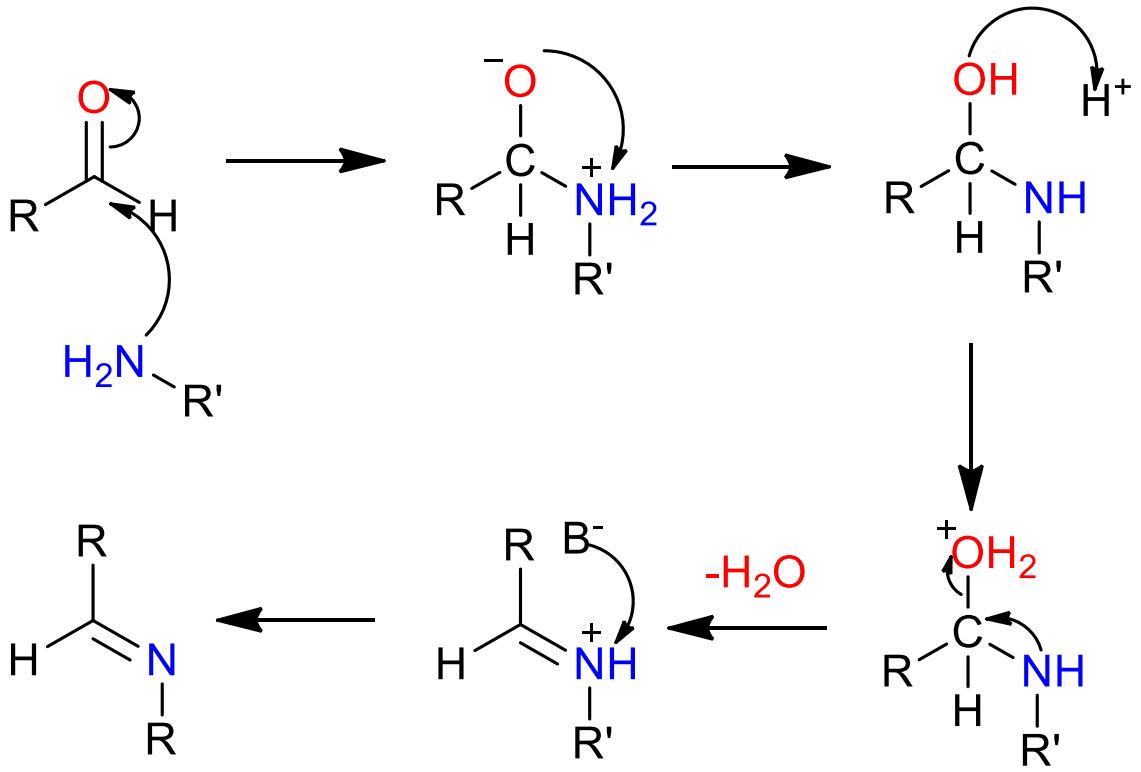

Scheme 1.4. General mechanism of the Schiff base condensation reaction

The chemistry of Schiff bases offers a wide variety of potential ligands through their high degree of tunability. The availability of numerous keto and amino precursors presents a great opportunity for

synthesizing imine compounds with varying structural properties. Careful selection of the precursors allows for the control of denticity, size/shape of binding sites, as well as any desired moieties to be incorporated into the ligand. The precursors for Schiff base compounds are often inexpensive and reactions yields tend to be high, making Schiff base ligands a reliable platform for coordination chemistry.

By exploiting the intrinsic anisotropy of the lanthanide ions, the redox activity of tetrazines and the versatility of Schiff bases one can foresee the rational design of radical-bridged lanthanide complexes. The fine tuning of the radical exchange coupling could be accomplished by the alteration of Schiff base ligand substituents. The incorporation or redox active moieties such as tetrazines puts a new spin on Schiff base coordination chemistry in the field of molecular magnetism.

1.16 References

1. (*a*) O. Kahn, Molecular Magnetism; 1st ed.; VCH Publishers Inc., New York, 1993; (*b*) J. H. van Vleck, The Theory of Electric and Magnetic Susceptibility; Oxford University Press, London, 1932.
2. A. Falick, B. Mahan and R. Myers, *J. Chem. Phys.*, 1965, **42**, 1837.
3. R. Boča, *Coord. Chem. Rev.*, 2004, **248**, 757.
4. A. Abragam and B. Bleaney, *Electron Paramagnetic Resonance of Transition Ions*, Dover Publications, Inc., Mineola, NY, 1986.
5. H. Kramers, *Proc. K. Ned. Akad. Wet.*, 1930, **33**, 959.
6. G. Christou, D. Gatteschi, D. Hendrickson and R. Sessoli, *MRS Bulletin*, 2000, **25**, 66.
7. (*a*) R. Sessoli, D. Gatteschi, A. Caneschi and M. A. Novak, *Nature*, 1993, **365**, 141; (*b*) R. Sessoli, H. L. Tsai, A. R. Schake, S. Wang, J. B. Vincent, K.Folting, D.Gatteschi, G.Christou and D.N.Hendrickson, *J. Am. Chem. Soc.*, 1993, **115**, 1804.

8. (*a*) L. Bogani and W. Wernsdorfer, *Nat. Mater.*, 2008, **7**, 179; (*b*) E. Coronado and M. Yamashita, *Dalton. Trans.*, 2016, **45**, 16553; (*c*) Y. Wang, W. Li, S. Zhou, D. Kong, H. Yang and L. Wu, *Chem. Commun.*, 2011, **47**, 3541; (*d*) G. Cucinotta, M. Perfetti, J. Luzon, M. Etienne, P. Car, A. Caneschi, G. Calvez, K. Bernot and R. Sessoli, *Angew. Chem. Int. Ed.*, 2012, **51**, 1606.
9. A. M. Ako, I. J. Hewitt, V. Mereacre, R. Clérac, W. Wernsdorfer, C. E. Anson, A. K. Powell, *Angew. Chem. Int. Ed.*, 2006, **45**, 4926.
10. N. Ishikawa, M. Sugita, T. Ishikawa, S.-Y. Koshihara, Y. Kaizu, *J. Am. Chem. Soc.*, 2003, **125**, 8694.
11. N. Ishikawa, M. Sugita and W. Wernsdorfer, *Angew. Chem. Int. Ed.*, 2005, **44**, 2931.
12. J. Rinehart, M. Fang, W. Evans and J. Long, *J. Am. Chem. Soc.*, 2011, **133**, 14236; J. Rinehart, M. Fang, W. Evans and J. Long, *Nature Chem.*, 2011, **3**, 538.
13. Y.-C. Chen, J.-L. Liu, L. Ungur, J. Liu, Q.-W. Li, L.-F. Wang, Z.-P. Ni, L. Chibotaru, X.-M. Chen and M.-L. Tong, *J. Am. Chem. Soc.*, 2016, **138**, 2829.
14. J. Liu, Y.-C. Chen, J.-L. Liu, V. Vieru, L. Ungur, J.-H. Jia, L. Chibotaru, Y. Lan, W. Wernsdorfer, S. Gao, X.-M. Chen and M.-L. Tong, *J. Am. Chem. Soc.*, 2016, **138**, 5441.
15. S. Gupta, T. Rajeshkumar, G. Rajaraman and R. Murugavel, *Chem. Sci.*, 2016, **7**, 5181.
16. Y.-S. Ding, N. Chilton, R. Winpenny and Y.-Z. Zheng, *Angew. Chem. Int. Ed.*, 2016, **128**, 1.
17. J. Rinehart, J. Long, *Chem. Sci.*, 2011, **2**, 2078.
18. A. Pinner, *Ber. Dtsch. Chem. Ges.* 1893, **26**, 2126.
19. P. Audebert, S. Sadki, F. Miomandre, G. Clavier, M. Vernieres, M. Saoud and P. Hapiot, *New. J. Chem.*, 2004, **28**, 387.
20. A.-C. Knall and C. Slugovc, *Chem. Soc. Rev.*, 2013, **42**, 5131.

21. D. Safin, A. Pialat, A. Leitch, N. Tumanov, I. Korobkov, Y. Filinchuk, J. Brusso and M. Murugesu, *Chem. Commun.*, 2015, **51**, 9547; H. Chifotides, I. Giles and K. Dunbar, *J. Am. Chem. Soc.*, 2013, **135**, 3039.
22. W. Kaim, *Coord. Chem. Rev.*, 2002, **230**, 127.
23. D. Chavez and M. Hiskey, *J. Energ. Mater.*, 1999, **17**, 357.
24. N. Shavaleev, S. Pope, Z. Bell, S. Faulkner and M. Ward, *Dalton. Trans.*, 2003, **5**, 808.
25. D. Roberts, B. Pilgrim, J. Cooper, T. Ronson, S. Zarra and J. Nitschke, *J. Am. Chem. Soc.*, 2015, **137**, 10068.
26. (*a*) S. Samanta, S. Das and P. Biswas, *J. Org. Chem.*, 2013, **78**, 11184; (*b*) S. Samanta and P. Biswas, *RSC Adv.*, 2015, **5**, 84328; (*c*) S. Samanta, S. Ray, A. Ghosh and P. Biswas, *RSC Adv.*, 2016, **6**, 39356.
27. (*a*) T. Troll, *Ibid.*, 1982, **27**, 1311; (*b*) W. Kaim, *J. Chem. Soc., Perkin Trans.*, 1985, **2**, 1633.
28. W. Kaim, S. Kohlmann, *Inorg. Chem.*, 1987, **26**, 68.
29. H. Schiff, *Justus Liebigs Ann. Chem.*, 1864, **131**, 118.

Chapter 2: Single-Molecule Magnet Behaviour in a Tetranuclear Dy^{III} Complex Formed from a Novel Tetrazine-Centered Hydrazone Schiff Base Ligand

There were two key features sought after in the initial design of a tetrazine-based Schiff base ligand: that two lanthanide ions could be encapsulated with one compartmental ligand and a central tetrazine ring to bridge the two lanthanides. With these aspects in mind a novel Schiff base ligand was formed from 3,6-bis(hydrazinyl)-1,2,4,5-tetrazine and *o*-vanillin. Two analogous tetranuclear lanthanide complexes were synthesized with the general formula **$[Ln_4(vht)_4(MeOH)_8](NO_3)_4 \cdot a$MeOH$\cdot b$$H_20$** where ($H_2$vht = 3,6-bis(vanillidenehydrazinyl)-1,2,4,5-tetrazine) and Ln = Dy^{III} (**1**), Gd^{III} (**2**). These complexes are characterized by several techniques; including single-crystal X-ray diffraction, SQUID magnetometry and single-crystal micro-SQUID hysteresis loop measurements. Elucidation of the crystal structure of the complexes shows that the lanthanide ions are bridged by a tetrazine ring, a rare bridging moiety for lanthanide ions. Magnetic studies reveal that both **1** and **2** show the presence of weak ferromagnetic exchange interactions between Ln ions , with **1** exhibiting Single-Molecule Magnet (SMM) behaviour with a magnetization reversal barrier of U_{eff} = 158 K ($\tau_0 = 1.06 \times 10^{-7}$ s).

2.1 Experimental

Materials. All manipulations were performed under aerobic conditions using chemicals and solvents from commercial sources (TCI, Alfa Aesar, and Strem Chemicals) and used as received without further purification.

Elemental Analysis, IR, NMR Spectroscopy. Elemental analysis was performed using an Isotope Cube elemental analyser. Infrared spectra were performed with a Varian 640 FTIR spectrometer equipped with an ATR in the 4000 cm^{-1} to 600 cm^{-1} range. NMR analyses were carried out using a Bruker Avance 400 spectrometer equipped with an automated sample holder and a 5 mm auto-tuning broadband probe with Z gradient.

Synthesis of 3,6-bis(vanillidenehydrazinyl)-1,2,4,5-tetrazine, H_2vht. The precursor, 3,6-bis(hydrazinyl)-1,2,4,5-tetrazine, was synthesized according to a previously reported procedure with slight modifications (Scheme 2.1).[1]

Triaminoguanidine hydrochloride (i): To a suspension of guanidine hydrochloride (40 g, 418.71 mmol) in 1,4-dioxane (240 mL) was added 79% hydrazine monohydrate solution (80 mL, 1300.36 mmol). The resulting mixture was stirred and refluxed for 4 hours. The mixture was then allowed to cool down to room temperature and placed in a -20°C freezer for 2 hours. The white precipitate was filtered, washed with 1,4-dioxane and dried under vacuum overnight to afford **i** as a white solid (53 g, 377.04 mmol, 90%).

1,2-Dihydro-3,6-bis(3,5-dimethyl-1H-pyrazol-1-yl)-1,2,4,5-tetrazine(ii): To a suspension of **i** (53 g, 377.04 mmol) was added dropwise acetylacetone (50 mL, 489.36 mmol) over 30 minutes. Upon addition an orange precipitate formed. The mixture was heated to 70°C for 4 hours. The mixture was then filtered, washed with water and recrystallized from ethanol to afford **ii** as a crystalline yellow solid (39 g, 143.22 mmol, 75%)

3,6-Bis(3,5-dimethyl-1H-pyrazol-1-yl)-1,2,4,5-tetrazine (iii): NO_2 gas was generated by subjecting copper turnings to concentrated HNO_3. The NO_2 gas was bubbled through a solution of **ii** (39 g, 143.22

mmol) in DMF (200 mL) for 1 hour. Upon addition of ice-cold water a red solid formed. The solid was filtered, washed with cold water and dried under vacuum to afford **iii** as a bright red solid (36.5 g, 136.06 mmol, 95%).

3,6-Bis(hydrazinyl)-1,2,4,5-tetrazine (iv): To a suspension of **iii** (36.5 g, 136.06 mmol) in acetonitrile (250 mL) was added 79% hydrazine monohydrate solution (18 mL, 292.58 mmol). The reaction mixture was then refluxed for 30 minutes. The mixture was cooled to room temperature and the solid was filtered and washed with acetonitrile to afford **iv** as a dark red solid (16 g, 112.58 mmol, 83%).

3,6-bis(vanillidenehydrazinyl)-1,2,4,5-tetrazine (v): To a suspension of 3,6-bis(hydrazinyl)-tetrazine (4.00 g, 0.028 mol) in methanol (500 mL) was added *o*-vanillin (9.47 g, 0.062 mol). The resulting reaction mixture was stirred under reflux over 18 hrs and then was allowed to cool to room temperature. The red precipitate was collected by filtration and washed with methanol. Recrystallization from DMF yields the DMF solvate of H_2vht as dark red needle-shaped crystals suitable for single-crystal X-ray diffraction. Crystalline material was collected by suction filtration and dried under vacuum prior to its use as ligand (5.85 g, 0.014 mol, 51%). ^{1}H NMR (DMSO-d_6, 400 MHz) δ 3.78 (s, 6H, OCH_3), 6.82 (t, J = 7.9 Hz, 2H, Ar), 6.96 (dd, J = 7.9 and 1.4 Hz, 2H, Ar), 7.10 (dd, J = 7.9 and 1.4 Hz, 2H, Ar), 8.41 (s, 2H, N=CH), 10.73 (s, 2H, NH), 12.05 (s, 2H, OH); ^{13}C (DMSO-d_6, 400 MHz) δ 160.0, 148.4, 147.0, 144.5, 120.8, 119.9, 119.5, 113.7, 56.3. IR (ATR, cm^{-1}): 3207 (br), 2980 (br), 1569 (m), 1538 (m), 1463 (m), 1417 (s), 1385 (m), 1366 (m), 1281 (w), 1247 (s), 1147 (m), 1094 (m), 1079 (m), 1043 (s), 982 (m), 940 (m), 885 (w), 856 (w), 833 (w), 781 (m), 736 (s), 633 (m), 585 (w), 565 (m). Anal. Calcd. for $C_{18}H_{18}N_8O_4$: C, 52.68; H, 4.42; N, 27.30. Found: C, 51.96; H, 4.54; N, 27.35.

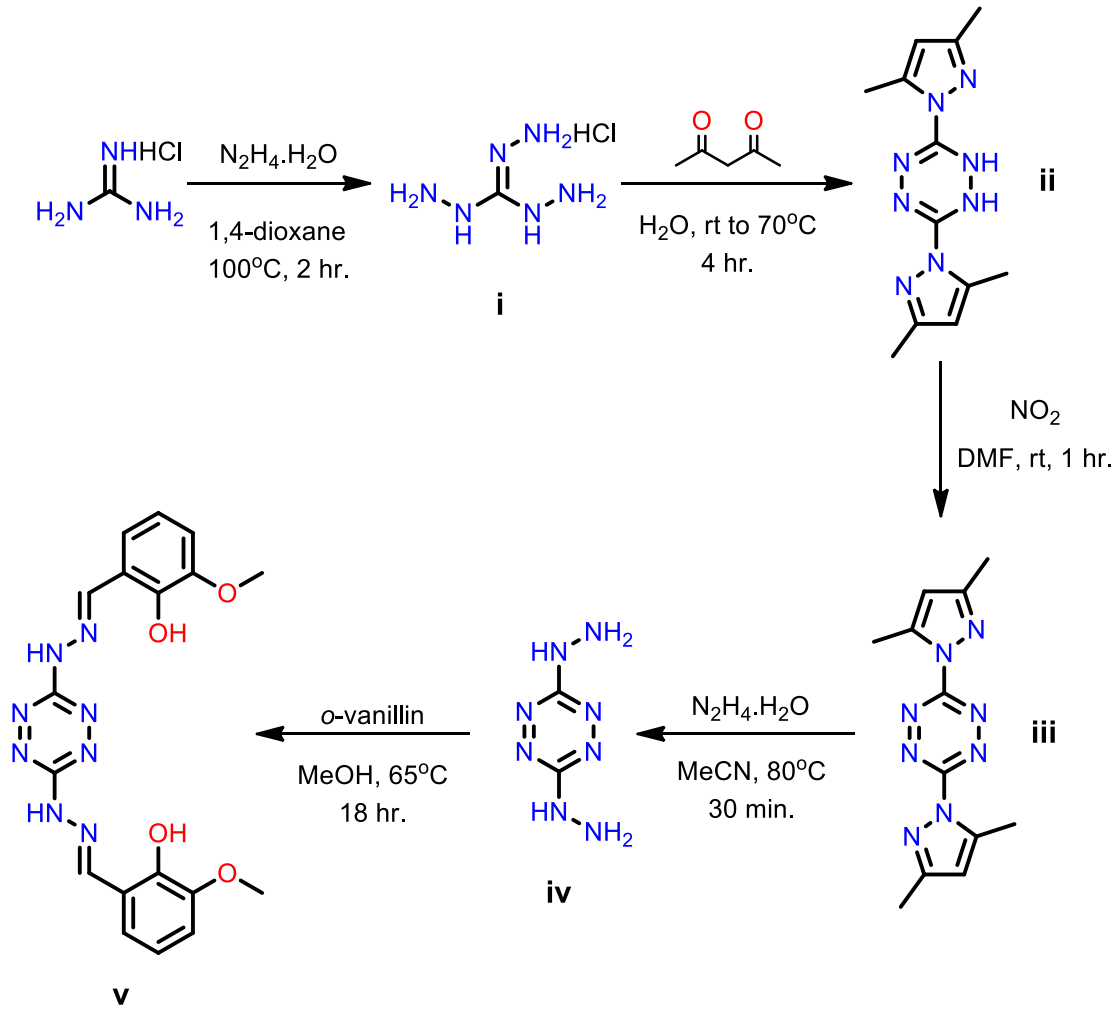

Scheme 2.1. Synthetic route for 3,6-bis(vanillidenehydrazinyl)-1,2,4,5-tetrazine (H_2vht).

Synthesis of $[Ln_4(vht)_4(MeOH)_8](NO_3)_4 \cdot a$MeOH$\cdot b H_20$ (Ln = Dy, *a* = 8.07, *b* = 0.65 (1), Gd, a = 8.19, b = 0.91 (2)). A room temperature suspension of $Ln(NO_3)_3 \cdot 6H_2O$ (114 mg for **1**, 113 mg for **2**, 0.25 mmol)) and H_2vht (51 mg, 0.125 mmol) was stirred for 5 min, after which NaN_3 (16 mg, 0.25 mmol) was added. The reaction mixture was stirred for another 30 minutes, filtered, and the filtrate was left to stand in a sealed vial. After 2 days, black block-shaped crystals suitable for single-crystal X-ray diffraction were obtained. Yield = 30 mg, 33%. IR for **1** and **2** (ATR, cm^{-1}): 3201 (br), 2941 (w), 2832 (w), 1603 (m), 1573 (m), 1524 (m), 1447 (m), 1397 (m), 1310 (m), 1283 (m), 1239 (m), 1220 (s), 1169 (m), 116, 1078 (m), 1055 (m), 1034 (m), 964 (m), 911 (w), 849 (m), 826 (w), 784 (w), 767 (w), 735 (s), 657 (m), 627 (m). IR for

2 (ATR, cm^{-1}): 3211 (br), 2941 (w), 2832 (w), 1606 (m), 1585 (m), 1530 (m), 1447 (m), 1397 (m), 1316 (m), 1287 (m), 1239 (m), 1220 (s), 1168 (m), 1114, 1077 (m), 1056 (m), 1013 (m), 967 (m), 910 (w), 851 (m), 826 (w), 784 (w), 768 (w), 737 (s), 659 (m), 630 (m). Elemental analysis for **1**; Expected: C, 34.59; H, 4.27; N, 16.49. Found: C, 34.21; H, 4.06; N, 16.97. Elemental analysis for **2**; Expected: C, 34.77; H, 4.32; N, 16.56. Found: C, 34.36; H, 4.10; N, 16.74.

Single-Crystal X-ray Diffraction Analysis. The crystals were mounted on a thin glass fibre using paraffin oil. Prior to data collection crystals were cooled to 200 K. Data were collected on a Bruker AXS SMART single-crystal diffractometer equipped with a sealed Mo tube source (λ = 0.71073 Å) APEX II CCD detector. Raw data collection and processing were performed with the APEX II software package from BRUKER AXS.[2] Semi empirical absorption corrections based on equivalent reflections were applied.[3] Direct methods yielded all non-H atoms, which were refined with anisotropic thermal parameters. All hydrogen atoms were calculated geometrically and were riding on their respective atoms. Crystallographic data for the ligand H_2vht, **1** and **2** are depicted in Table 2.1. CCDC numbers are as follows: 1518373 (**1**); 1518374 (**2**); 1518375 (H_2vht).

Table 2.1. Crystallographic data for H_2vht, **1** and **2**.

Compound	H_2vht	**1**	**2**
Empirical Formula	$C_{30}H_{46}N_{12}O_8$	$C_{88.07}H_{129.59}Dy_4N_{36}O_{44.72}$	$C_{88.19}H_{130.58}Gd_4N_{36}O_{45.10}$
Crystal system	Monoclinic	Triclinic	Triclinic
Space group	$P2_1/c$	P-1	P-1
a (Å)	11.7537(11)	11.8906(4)	11.9318(3)
b (Å)	21.3005(11)	15.1106(5)	15.1642(4)
c (Å)	7.0776(4)	18.9649(6)	18.9347(6)
α (°)	90	104.400(1)	104.855(2)
β (°)	91.253(3)	100.958(2)	101.124(2)
γ (°)	90	107.614(1)	107.478(2)
V (Å^3)	1771.52(16)	3012.97(17)	3020.17(15)
Z	2	1	1
ρ_{calc} (g cm^{-3})	1.318	1.607	1.619
λ (Å)	0.71073	0.71073	0.71073
T (K)	200(2)	200(2)	200(2)
μ (mm^{-1})	0.098	2.544	2.262
F (000)	748	1452	1472
Reflections Collected	19209	37780	16741
Independent Reflections	4400	10888	10839
Reflections with I > 2σ(I)	2129	8298	7398
Goodness of fit on F^2	1.008	1.065	1.019
R_1, wR_2 (I > 2σ(I))[a]	0.0706, 0.1132	0.0466, 0.1151	0.0507, 0.1123
R_1, wR_2 (all data)	0.1736, 0.1373	0.0702, 0.1365	0.0881, 0.1303

[a] $R = R_1 = \sum||F_o| - |F_c||/\sum|F_o|$; $wR_2 = \{\sum[w(F_o^2 - F_c^2)^2]/\sum[w(F_o^2)^2]\}^{1/2}$; $w = 1/[\sigma^2(F_o^2)+(ap)^2 + bp]$, where $p = [\max(F_o^2, 0) + 2F_c^2]/3$.

Magnetic Measurements. Magnetic susceptibility measurements were collected using a MPMS-XL7 Quantum Design SQUID magnetometer. Direct current (dc) susceptibility data measurements were performed at temperatures ranging from 1.9 to 300 K, and between applied fields of -5 to 5 T.

Measurements were performed on crushed polycrystalline samples of 24.6 and 23.4 mg for samples **1** and **2**, respectively. Each sample was wrapped in a polyethylene membrane. Alternating current (ac) susceptibility measurements were performed under an oscillating ac field of 3.78 Oe and ac frequencies ranging from 0.1 to 1500 Hz. Magnetization *vs.* field measurements were performed at 100 K in order to check for the presence of ferromagnetic impurities, which were found to be absent. Magnetic data were corrected for diamagnetic contributions using Pascal's constants.

2.2 Structural Details of H_2vht and 1. In order to give a detailed description of the structural characteristics of the free ligand, and to observe the effects of coordination, single-crystal X-ray diffraction was carried out on the H_2vht ligand in addition to NMR spectroscopy. The ligand crystallizes in the monoclinic $P2_1/c$ space group with all of the ligand atoms being nearly coplanar. The structure of the ligand consists of one central tetrazine ring and two identical hydrazone substituents derived from *o*-vanillin (Figure 2.1). The molecule exhibits centrosymmetry with the inversion center located directly in the center of the tetrazine ring. The two vanillidene moieties, in conjunction with the tetrazine ring, form four coordination pockets. These pockets are comprised of two large tridentate pockets consisting of N1, N4a and O1 and two smaller bidentate pockets formed by O1 and O2 from the vanillidene moieties. The larger pockets are well-suited to the encapsulation of lanthanide ions. The N-N bond lengths of 1.32 Å and C-N bond lengths of 1.34 Å are in agreement with previously reported tetrazine compounds.[4] The ^{1}H NMR spectrum of H_2vht consists of four singlets and three phenyl multiplets (Figure 2.2). The characteristic imine protons of the ligand give a singlet at 8.41 ppm. The methoxy groups of the ligand are depicted with a singlet at 3.78 ppm. The phenyl multiplets of the vanillidene moieties consist of two doublet of doublets and one triplet. The first doublet of doublets at 7.10 ppm is assigned

to the phenyl protons nearest to the imine functional group, while the second at 6.96 ppm is assigned to the phenyl protons nearest to the methoxy group. The phenyl triplet is assigned to the protons at the para position to the hydroxy groups. The remaining N-H and O-H protons are observed as singlets at 10.73 and 12.05 ppm, respectively.

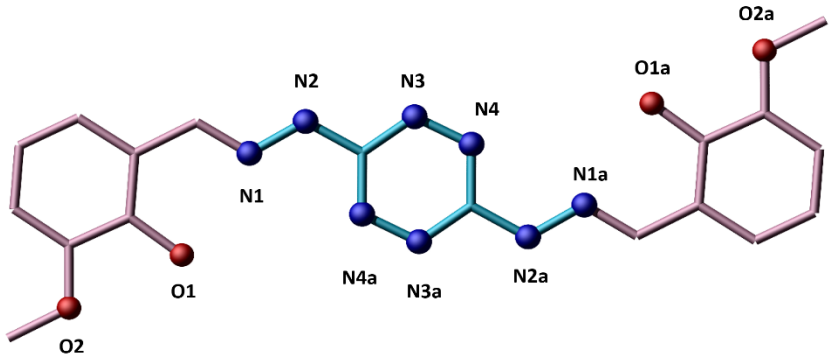

Figure 2.1. Crystal structure of H2vht (3,6-bis(vanillidenehydrazinyl)-1,2,4,5-tetrazine). Solvent molecules and hydrogen atoms were omitted for clarity. Symmetry equivalent atoms are denoted by an additional “a” in the label. Colour code: red (O), blue (N). All unfilled vertices are carbon atoms.

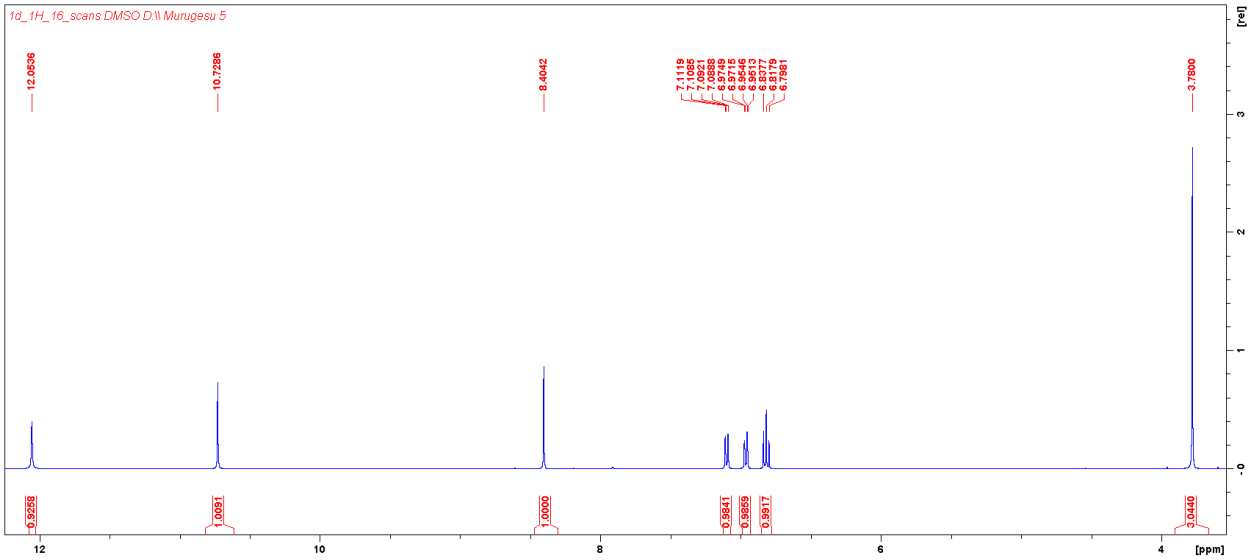

Figure 2.2. ^{1}H NMR spectrum of H_2vht in DSMO-d_6

Coordination of the deprotonated ligand to Dy^{III} or Gd^{III} yields two isostructural complexes, with the Dy^{III} complex (**1**) depicted in Figure 2. The complexes crystallize in the triclinic *P*-1 space group. For brevity, the Dy analogue will be described. Each Dy^{III} ion adapts a nine-coordinate motif, with three N-donors and six O-donors. For example, Figure 2.3 shows Dy1 is coordinated to two imine nitrogen atoms, N8 and N9, and one nitrogen from the tetrazine ring, N11. The *o*-vanillin side groups contribute oxygen atoms O1, O2, O3 and O5 to the coordination sphere of Dy1. Two oxygen atoms from two methanol molecules, O15 and O16, make up the remainder of the coordination sphere. Dy2 exhibits a similar coordination environment to Dy1. In order to formally assess the coordination geometry of the Dy^{III} ions a comparative technique was employed using the software SHAPE,[5] which allows for the calculation of continuous shape measures with crystallographic coordinates relative to ideal reference polyhedra. The comparison of thirteen reference polyhedra with the coordination polyhedra of Dy1 and Dy2 by SHAPE analysis (Table 2.2) reveals that Dy1 possesses a distorted spherical capped square antiprism (C_{4v}) geometry while Dy2 resembles a spherical tricapped trigonal prism (D_{3h}) (Figure 2.3).

While complexes **1** and **2** are tetranuclear overall, they are composed of two dinuclear subunits (Figure 2.3). These subunits are linked by two ligand molecules and bound by the vanillidene donor atoms. This bridging motif between subunits also provides two bridging modes between Dy1 and Dy2 in the form of phenoxide oxygen atoms, O1 and O3. With the two phenoxide atoms and the tetrazine ring there is a total of three bridging motifs between the Dy^{III} centers.

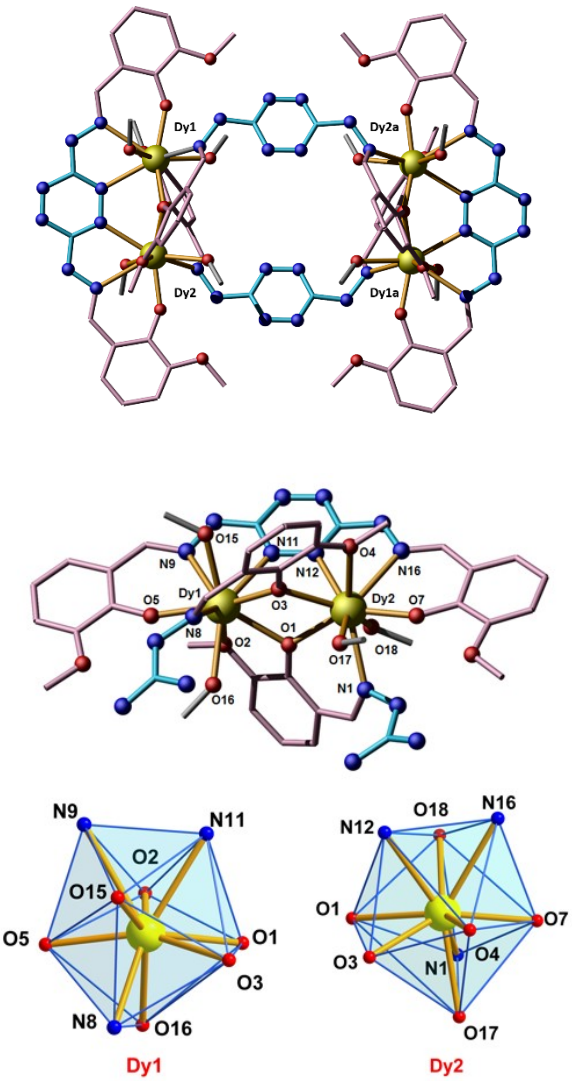

Figure 2.3. Molecular structure (top), dinuclear subunit (middle) and coordination polyhedra (bottom) for complex **1**. Colour code: yellow (Dy), red (O), blue (N). Hydrogen atoms are omitted for clarity. All unfilled vertices are carbon atoms.

Table 2.2. SHAPE constants for the Dy^{III} centers in **1**. The lowest SHAPE constants are highlighted in yellow.

SHAPE Code	Point Group	Description	Dy1	Dy2
EP-9	D_{9h}	Enneagon	35.622	35.650
OPY-9	C_{8v}	Octagonal pyramid	22.632	22.755
HBPY-9	D_{7h}	Heptagonal bipyramid	19.406	18.959
JTC-9	C_{3v}	Johnson triangular cupola J3	15.679	15.462
JCCU-9	C_{4v}	Capped cube J8	10.068	10.051
CCU-9	C_{4v}	Spherical-relaxed capped cube	9.444	9.327
JCSAPR-9	C_{4v}	Capped square antiprism J10	1.134	1.455
CSAPR-9	C_{4v}	Spherical capped square antiprism	0.650	0.893
JTCTPR-9	D_{3h}	Tricapped trigonal prism J51	1.964	1.875
TCTPR-9	D_{3h}	Spherical tricapped trigonal prism	0.944	0.780
JTDIC-9	C_{3v}	Tridiminished icosahedron J63	12.104	11.686
HH-9	C_{2v}	Hula-hoop	12.726	12.782
MFF-9	C_s	Muffin	1.376	1.419

In addition, the complex is also centrosymmetric, giving rise to symmetry equivalent atoms between subunits. While the dinuclear lanthanide complexes of Shavaleev and co-workers do possess a tetrazine bridge,[6] the lanthanide ions are bridged from across the tetrazine moiety. In the case of complexes **1** and **2**, the Ln^{III} ions are bridged by the tetrazine ring from the same side. This leads to an unprecedented bridging motif for lanthanide-based systems. Another distinguishing feature in our system is the large spatial separation between the dinuclear subunits with a Dy1-Dy2a distance of 10.49 Å and a Dy1-Dy1a distance of 11.21 Å. For comparison, the smallest intermolecular Dy···Dy distance for complex **1** is 10.43 Å. These distances are significantly larger than those of the Dy1-Dy2

subunit distances of 3.91 Å. Statistical analysis for all reported compounds with Dy^{III} ions bridged by moieties consisting of one or two atoms shows that the average intramolecular Dy···Dy distance is 3.83 Å. The Dy1-Dy2 distance of **1** is then slightly above the average intramolecular distances for similarly bridged compounds.

When comparing the free ligand to the coordinated tetrazine moiety, the latter exhibits a relatively large contortion of the tetrazine ring. The bond distance of the nitrogen atoms N11 and N12 in complex **1** is elongated to 1.36 Å while the opposite nitrogen atoms, N13 and N14, have a shorter bond distance of 1.27 Å (Figure 2.4). The coordination of Dy^{III} is likely the cause of this contortion, resulting in the ligand being forced outward from the metal ions.

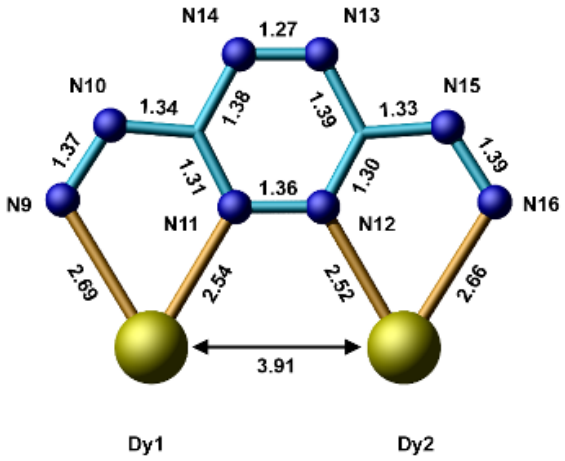

Figure 2.4. Bond distances of the central tetrazine moiety for **1** in Å. Colour code: yellow (Dy), blue (N). Hydrogen atoms are omitted for clarity. All unfilled vertices are carbon atoms.

2.3 Static Magnetic Susceptibility. The analysis of the crystal structure of compounds **1**-**2** (*vide supra*) suggests that the most likely intramolecular magnetic interactions would occur between Ln1 and Ln2 of each subunit. This is due to the close proximity of these metal ions (3.91 Å). Conversely, the two dinuclear subunits are well separated by distances of 10.49 Å and 11.21 Å, and thus are unlikely to

experience any significant interaction between spin carriers. Close inspection of the bridging between Ln ions within a single dimer reveals the potential for three superexchange pathways. Two of the pathways are mediated by phenoxide moieties of the H_2vht ligand, in a similar fashion to previously reported Schiff-base compounds,[7] while an additional bridging occurs through two nitrogen atoms (N11 and N12) of the tetrazine ring. It is important to note that dipole-dipole interactions will also likely contribute to the Ln^{III}-Ln^{III} coupling, in addition to the superexchange interactions like in most cases of lanthanide systems.

The temperature dependence of the χT product displays the presence of non-negligible ferromagnetic coupling between spin carriers (Figure 2.5). The room temperature values at 300 K are 55.81 and 30.81 cm^3 K mol^{-1} for **1** and **2**, respectively, which are in good agreement with the expected theoretical values of 56.68 and 31.52 cm^3 K mol^{-1}, for four non-interacting lanthanide ions (Dy^{III}: $^6H_{15/2}$, S = 5/2, L = 5, g = 4/3; Gd^{III}: $^8S_{7/2}$, S = 7/2, L = 0, g = 2). Upon lowering the temperature, the χT values of **1** and **2** remain relatively constant down to 12 K, before abruptly increasing to a maximum of 69.86 cm^3 K mol^{-1} for **1** and 33.73 cm^3 K mol^{-1} for **2** at 1.9 K. This sharp increase is indicative of intramolecular ferromagnetic coupling, which dominates the magnetic behaviour at low temperatures. In order to further probe the magnetic exchange interactions, we applied the van Vleck equation to Kambe's vector coupling scheme using the isotropic spin Hamiltonian:

$$\hat{\mathrm{H}} = -2J(\hat{\mathrm{S}}_{\boldsymbol{a}} \cdot \hat{\mathrm{S}}_{\boldsymbol{b}} + \hat{\mathrm{S}}_{\boldsymbol{a}} \cdot \hat{\mathrm{S}}_{\boldsymbol{b}})$$

with S_a = S_b = 7/2, allowing us to reproduce the χT curve of 2 (Figure 2.5). Due to the symmetry equivalence of the dimeric subunits and their spatial separation with respect to each other we decided

to model the exchange interactions of 2 with one *J* parameter. The full form of the Van Vleck equation for the system is written as follows:

$$\chi T = 2\left(\frac{Ng^2\beta^2}{3k}\frac{5580e^{\left(\frac{56J}{kT}\right)} + 3276e^{\left(\frac{42J}{kT}\right)} + 1650e^{\left(\frac{30J}{kT}\right)} + 720e^{\left(\frac{20J}{kT}\right)} + 252e^{\left(\frac{12J}{kT}\right)} + 60e^{\left(\frac{6J}{kT}\right)} + 6e^{\left(\frac{2J}{kT}\right)}}{105e^{\left(\frac{56J}{kT}\right)} + 78e^{\left(\frac{42J}{kT}\right)} + 55e^{\left(\frac{30J}{kT}\right)} + 36e^{\left(\frac{20J}{kT}\right)} + 21e^{\left(\frac{12J}{kT}\right)} + 10e^{\left(\frac{6J}{kT}\right)} + 3e^{\left(\frac{2J}{kT}\right)} + 1}\right)$$

The best-fit parameters obtained were $J = 0.009(3)$ cm^{-1} and $g = 1.982(1)$, testifying to the weak ferromagnetic interactions between lanthanide ions.[8] As noted above, these interactions likely originate from superexchange and dipole-dipole interactions. It is also important to note that there is a greater upturn in the χT product of **1**, which suggests that the interaction in **1** could be significantly larger than in **2**.

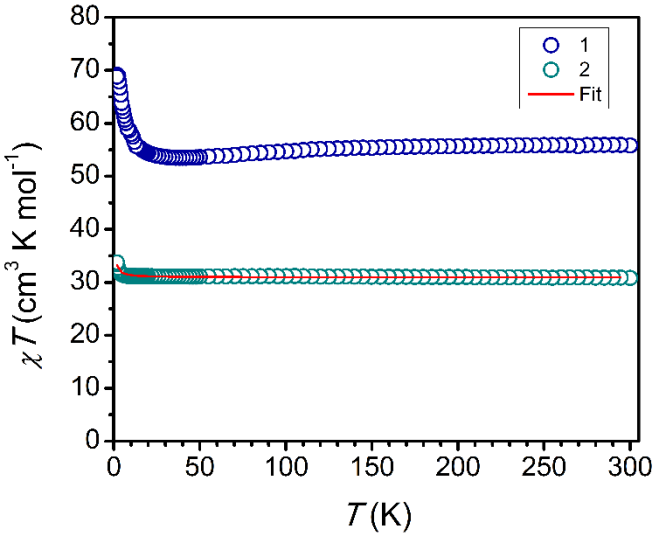

Figure 2.5. *χT vs. T* plot for **1** and **2** under applied dc fields of 1000 Oe. The solid line shows the best fit obtained through the magnetic model described in the text.

Furthermore, we examined the field (*H*) dependence of the magnetization (*M*), which shows a rapid increase of the magnetization at low fields up to 27.40 μ_B (**1**) and 25.49 μ_B (**2**) at 5 T and 2.0 and 1.9 K, respectively (Figure 2.6). This rapid increase in magnetization is expected for ferromagnetically coupled

systems.[8] The *M vs. HT*$^{-1}$ plots, at varying temperatures, show magnetization curves that are slightly deviated from one another, suggesting the presence of non-negligible magnetoanisotropy and/or low-lying excited states for compound **1** (Figure 2.7). On the other hand, the isotropic nature of **2** is confirmed through the superimposition of the analogous magnetization curves at differing temperatures (Figure 2.7).

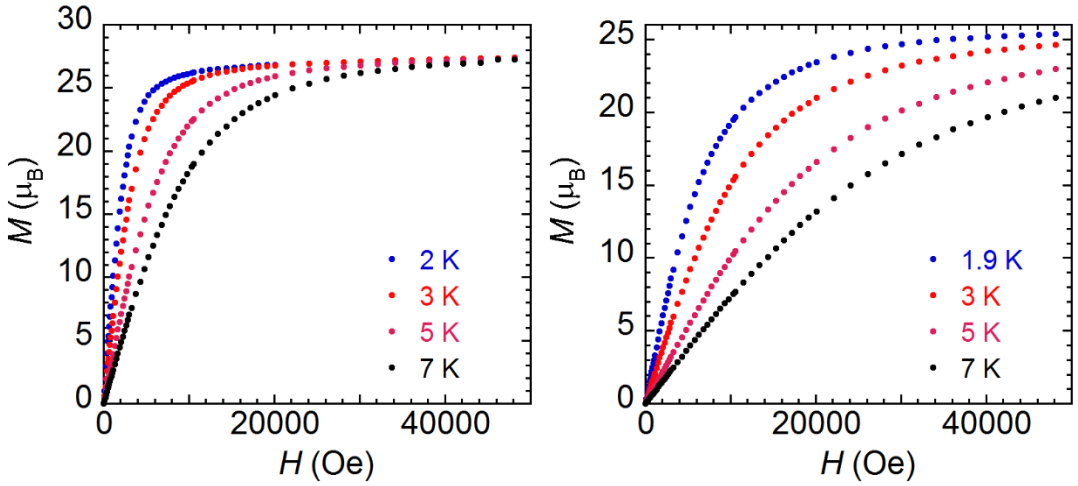

Figure 2.6. Field dependence of the magnetization, *M*, between 2 and 7 K for **1** (left) and 1.9 and 7 K for **2** (right).

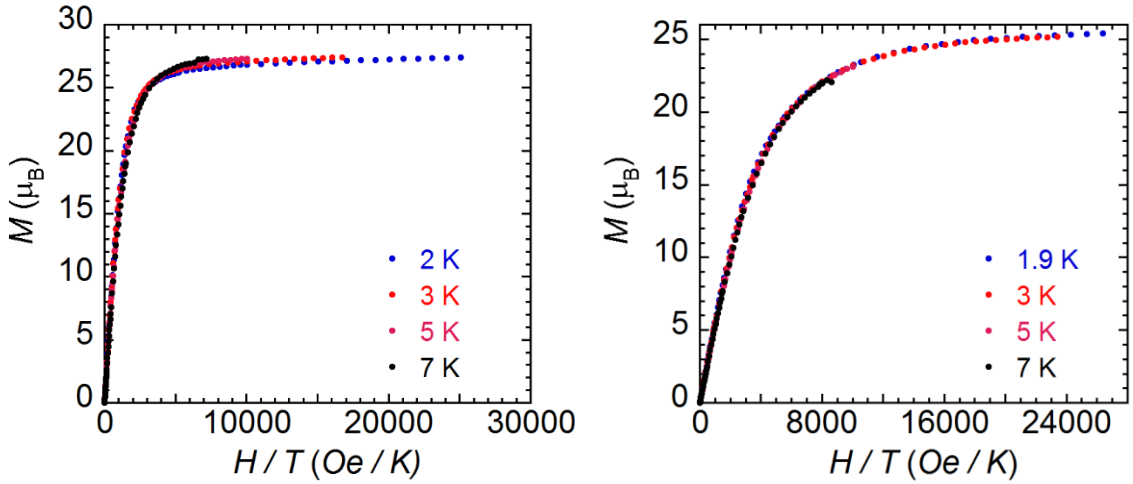

Figure 2.7. Reduced magnetization plots from 2 and 7 K for **1** (left) and 1.9 and 7 K for **2** (right).

2.4 Dynamic magnetic susceptibility. Due to the recent successes of discrete Dy-based complexes displaying record SMM properties,[9] we were prompted to investigate the dynamics of the magnetization of compound 1. The frequency dependence of the ac susceptibility was investigated under zero applied dc field (Figure 2.8). The temperature dependence of the ac susceptibility under zero dc field reveals an out-of-phase signal (χ'') with observable maxima. As the frequency is increased, the maxima are shifted to higher temperatures, confirming slow relaxation of the magnetization, characteristic of SMMs. The χ'' *vs.* ν data for 1 were fitted using a generalized Debye model for a single relaxation process:[10]

$$\chi'(\nu) = \chi_S + (\chi_T - \chi_S)\frac{1 + (2\pi\nu\tau)^{1-\alpha}\sin\left(\frac{\pi\alpha}{2}\right)}{1 + 2(2\pi\nu\tau)^{1-\alpha}\sin\left(\frac{\pi\alpha}{2}\right) + (2\pi\nu\tau)^{2(1-\alpha)}}$$

$$\chi''(\nu) = (\chi_T - \chi_S)\frac{(2\pi\nu\tau)^{1-\alpha}\cos\left(\frac{\pi\alpha}{2}\right)}{1 + 2(2\pi\nu\tau)^{1-\alpha}\sin\left(\frac{\pi\alpha}{2}\right) + (2\pi\nu\tau)^{2(1-\alpha)}}$$

Where χ_T and χ_S are the isothermal and adiabatic susceptibilities, respectively, τ is the relaxation time and α depicts the distribution of relaxation times. From these data, we can also observe frequency dependence in both the in-phase (χ') and out-of-phase (χ'') signals. Selected data, including τ and α values obtained from the fits of χ'' *vs.* ν are summarized in Table 2.3. The shifting of peak maxima confirms slow relaxation of the magnetization. The relaxation time (τ) is derived from the frequency dependent measurements between 5 and 18 K and plotted as a function of 1/*T* (Figure 2.9). Above 15 K, the relaxation follows a thermally activated mechanism, eliciting an energy barrier of 158 K and a pre-exponential factor (τ_0) of 1.06 x 10^{-7} s using the Arrhenius equation:$\tau = \tau_0 exp(U_{eff}/kT)$.

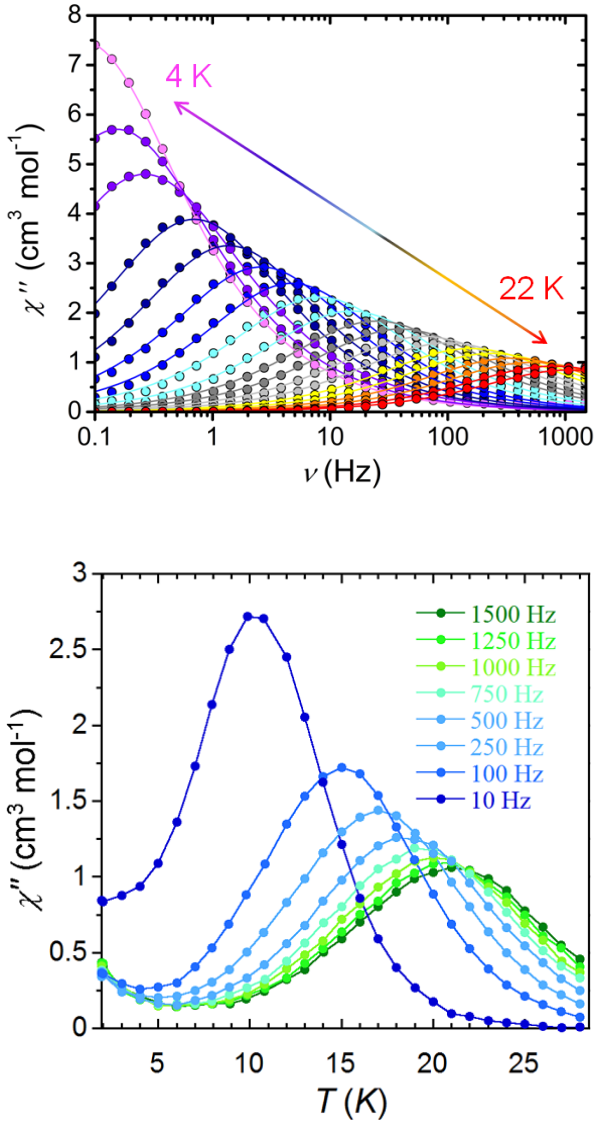

Figure 2.8. Out-of-phase magnetic susceptibility (χ'') *vs.* frequency (top) and out-of-phase magnetic susceptibility *vs.* temperature (bottom) for 1. The χ'' *vs.* ν data for **1** were fitted using a generalized Debye model for a single relaxation process.

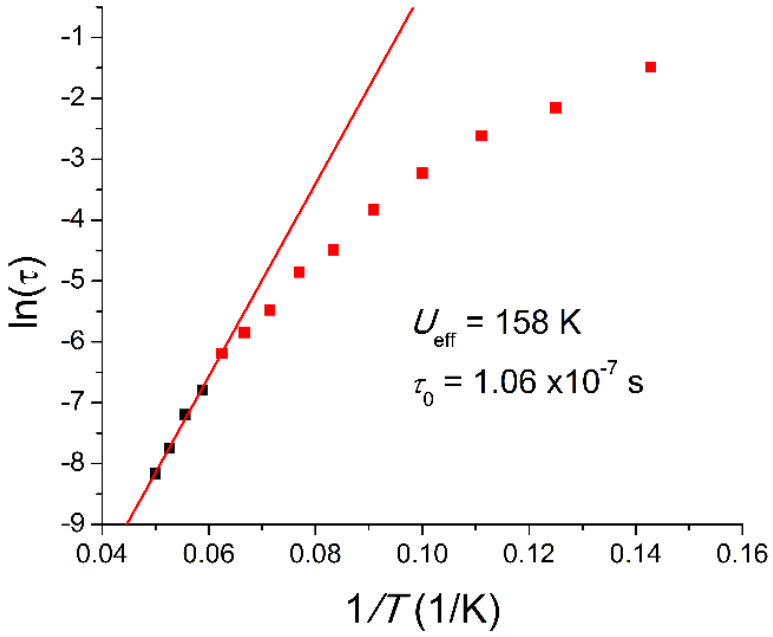

Figure 2.9. ln(τ) *vs.* 1/*T* Arrhenius plot for **1**.

A graphical representation of χ'' *vs.* χ' (Cole-Cole plot) for **1** was fitted using a generalized Debye model for a single relaxation process between 7 and 20 K (Figure 2.10). The semi-circular plots give a moderately narrow distribution of α parameters ranging from 0.25 to 0.41, which is consistent with α values obtained by fitting the frequency dependent data (Table 2.3).

To further investigate the low temperature magnetic behaviour of complex **1**, single-crystal relaxation measurements were carried out on a micro-SQUID array.[11] Below 0.5 K with a sweep rate of 0.14 T/s, the *M vs. H* sweeps exhibited hysteretic behaviour and a small opening could be observed up to a temperature of 4 K (Figure 2.11). The width of the magnetic hysteresis loop of **1** shows strong temperature, and moderate sweep rate, dependence. The S shape of the hysteresis loop and the step position located between 0-0.2 T is reminiscent of previously reported weakly coupled lanthanide

dimers. Such signature behaviours result from single-ion relaxation entangled with the neighbouring Dy ion relaxation within the molecule *via* weak intramolecular-exchanged biased interactions.[7b]

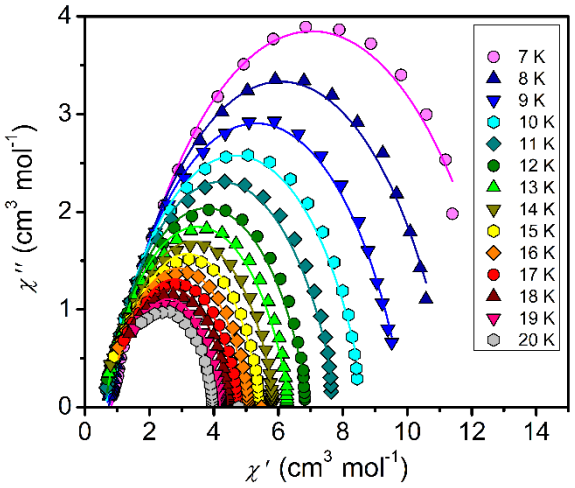

Figure 2.10. Cole-Cole plot for frequency dependent ac susceptibility data of **1**. Solid lines are the best fit to the generalized Debye model.

Table 2.3. Selected parameters obtained by fitting χ'' *vs.* ν plots of **1** using a generalized Debye model.

T / K	τ / s	τ std. dev. / s	α	α std. dev.
4.0	2.006	0.0997	0.320	0.008
5.0	1.033	0.0220	0.317	0.005
6.0	0.601	0.0075	0.331	0.003
7.0	0.228	0.0036	0.284	0.006
8.0	0.116	0.0018	0.277	0.006
9.0	0.062	9.0E-4	0.274	0.005
10.0	0.0338	7.6E-4	0.266	0.008
11.0	0.0197	5.0E-4	0.270	0.009
12.0	0.0105	2.9E-4	0.273	0.010
13.0	0.0064	2.0E-4	0.281	0.011
14.0	0.0040	1.3E-4	0.284	0.011
15.0	0.0025	8.0E-5	0.286	0.011
16.0	0.0016	5.1E-5	0.287	0.012
17.0	0.0010	3.1E-5	0.284	0.011
18.0	6.8E-4	2.0E-5	0.282	0.011
19.0	4.5E-4	1.4E-5	0.278	0.011
20.0	3.1E-4	1.0E-5	0.273	0.011
21.0	2.0E-4	9.6E-6	0.278	0.013

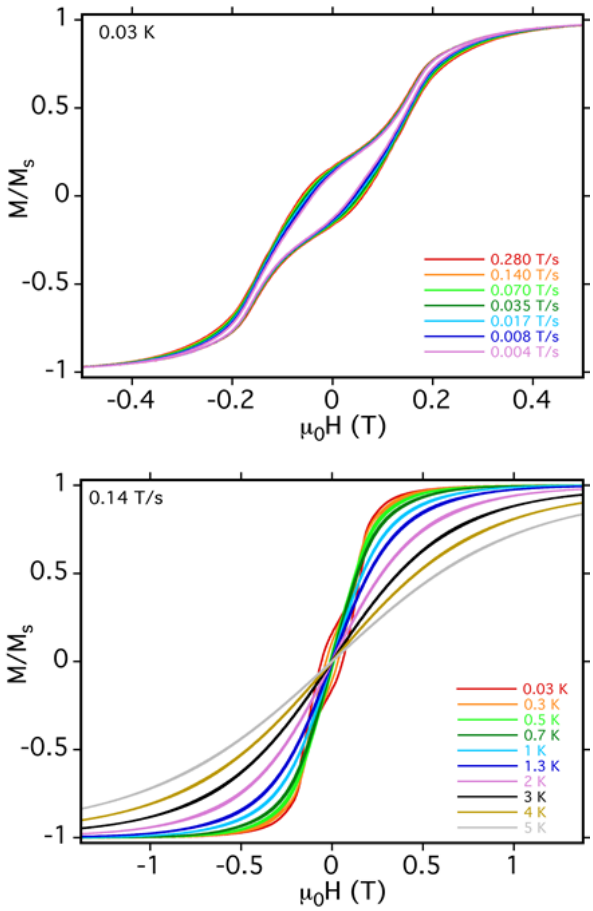

Figure 2.11. Single-crystal magnetic hysteresis loop measurements on a micro-SQUID array for **1** with varying sweep rate (top) and temperature (bottom).

Electrostatic modelling of the anisotropy axes in complex **1** was also carried out using Magellan.[12] In the case of low symmetry Dy^{III} complexes the ground Kramers doublet shows strong axiality and the *g*-tensor approaches that of the $m_j = 15/2$ levels, where $g_x = g_y = 0$ and $g_z = 20$.[13] The electron density distribution in Dy^{III} can be approximated by an oblate spheroid, and by solving for the electrostatic energy minimum with respect to the crystal field potential, the orientation of the magnetic anisotropy axes can be obtained. Carrying out this electrostatic modelling reveals near-collinear alignment of the

easy-axis vectors between Dy^{III} centers (Figure 2.12), with an angle of 7° between the Dy1 and Dy2 axes. The vectors lie along the direction of the anionic phenoxide atoms for each subunit, with deviations in the alignment of these vectors attributed to slight differences in coordination geometry between the Dy1 and Dy2 ions. While the easy axis vectors between the subunits align antiferromagnetically with each other the distance between the subunits is large enough to not interfere with the ferromagnetic interaction observed within the individual subunits.

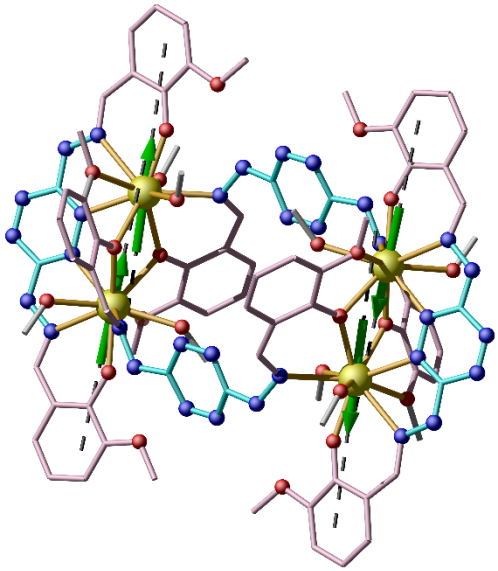

Figure 2.12. Anisotropy axes in the ground Kramers doublet (m_j = 15/2) for each Dy^{III} ion in 1. Axes modelled using Magellan software. Colour code: yellow (Dy), red (O), blue (N). Hydrogen atoms are omitted for clarity. All unfilled vertices are carbon atoms.

2.5 Conclusions. The structural and magnetic properties of two analogous tetranuclear lanthanide complexes consisting of two dimeric subunits are presented and discussed. The synthesis of these complexes was achieved using a new compartmental Schiff base ligand incorporating a tetrazine ring. Both the Dy and Gd analogues exhibit dominant ferromagnetic exchange interactions at low

temperature. The $\{Ln_2\}$ subunits of these tetranuclear complexes are sufficiently separated to be treated as individual dinuclear systems and can therefore be modelled as such. In addition to exhibiting ferromagnetic exchange, compound **1** exhibits SMM behaviour with a sizeable magnetization reversal barrier of 158 K. Although the strength of the interaction is weak, it is noteworthy in this system dominant ferromagnetic interactions are observed. If such ferromagnetically coupled systems are strongly coupled, high spin ground states with large energy barriers can be expected. With this in mind our ongoing studies focus on the reduction of the tetrazine ring in order to improve the strength of the Ln^{III}-Ln^{III} interactions through radical exchange coupling.

2.6 References

1. B. Rao, S. Dhokale, P. Rajamohanan and S. Hotha, *Chem. Commun.*, 2013, **49**, 10808.
2. APEX Software Suite v.2012; Bruker AXS: Madison, WI, 2005.
3. R. Blessing, *Acta. Crystallogr. A.*, 1995, **51**, 33.
4. M. Schwach, H. Hausen and W. Kaim, *Inorg. Chem.*, 1999, **38**, 2242.
5. D. Casanova, M. Llunel, P. Alemany and S. Alvarez, *Chem. Eur. J.*, 2005, **11**, 1479.
6. N. Shavaleev, S. Pope, Z. Bell, S. Faulkner and M. Ward, *Dalton. Trans.*, 2003, **5**, 808.
7. (*a*) F. Habib, G. Brunet, V. Vieru, I. Korobkov, L. Chibotaru and M. Murugesu, *J. Am. Chem. Soc.*, 2013, **135**, 13242; (*b*) F. Habib, P.-H. Lin, J. Long, I. Korobkov, W. Wernsdorfer and M. Murugesu, *J. Am. Chem. Soc.*, 2011, **133**, 8830; (*c*) P.-H. Lin, W.-B. Sun, Y.-M. Tian, P.-F. Yan, L. Ungur, L. Chibotaru and M. Murugesu, *Dalton Trans.*, 2012, **41**, 12349; (*d*) F. Yang, P. Yan, Q. Li, P. Chen and G. Li, *Eur. J. Inorg. Chem.*, 2012, 4287; (*e*) S.-Y. Lin, G.-F. Xu, L. Zhao, Y.-N. Guo, and J. Tang, *Dalton Trans.*, 2011, **40**, 8213; (*f*) A. Gorczynski, M. Kubicki, D. Pinkowicz,

R. Pelka, V. Patroniak and R. Podgajny, *Dalton Trans.*, 2015, **44**, 16833; (*g*) Y.-L. Chien, M.-W. Chang, Y.-C. Tsai, G.-H. Lee, W.-S. Sheu and E.-C. Yang, *Polyhedron*, 2015, **102**, 8; (*h*) P. Bag, C. Rastogi, S. Biswas, S. Sivakumar, V. Mereacre, and V. Chandrasekhar, *Dalton Trans.*, 2015, **44**, 4328; (*i*) M. Holyńska, R. Clérac and M. Rouzières, *Chem. Eur. J.*, 2015, **21**, 13321; (*j*) S. Xue, Y.-N. Guo, L. Ungur, J. Tang, and L. Chibotaru, *Chem. Eur. J.*, 2015, **21**, 14099; (*k*) C. Chen, J. Zhang, Y. Zhang, Z. Yang, H. Wu, G. Pana and Y. Bai, *J. Coord. Chem.*, 2015, **68**, 1054; (*l*) P.-H. Lin, W.-B. Sun, M.-F. Yu, G.-M. Li, P.-F. Yan and M. Murugesu, *Chem. Commun.*, 2011, **47**, 10993; (*m*) J.-P. Costes, F. Dahan and F. Nicodeme, *Inorg. Chem.*, 2003, **42**, 6556; (*n*) J. Chakraborty, A. Ray, G. Pilet, G. Chastanet, D. Luneau, R. Ziessel, L. Charbonnière, L. Carrella, E. Rentschler, M. Fallah and S. Mitra, *Dalton Trans.*, 2009, 10263; (*o*) F. Gao, Y.-Y. Li, C.-M. Liu, Y.-Z. Li and J.-L. Zuo, *Dalton Trans.*, 2013, **42**, 11043; (*p*) L. Natrajan, P. Timmins, M. Lunn and S. Heath, *Inorg. Chem.*, 2007, **46**, 10877; (*q*) P.-H. Lin, M. Leclère, J. Long, T. Burchell, I. Korobkov, R. Clérac and M. Murugesu, *Dalton. Trans.*, 2010, **39**, 5698; (*r*) T. Balashova, A. Pushkarev, V. Ilichev, M. Lopatin, M. Katkova, E. Baranov, G. Fukin and M. Bochkarev, *Polyhedron*, 2013, **50**, 112; (*s*) V. Chandrasekhar, P. Bag, M. Speldrich, J. van Leusen and P. Kogerler, *Inorg. Chem.*, 2013, **52**, 5035; (*t*) X. Mei, X. Wang, J. Wang, Y. Ma, L. Li and D. Liao, *New. J. Chem.*, 2013, **37**, 3620; (*u*) L. Zhao, J. Wu, H. Ke and J. Tang, *Cryst. Eng. Comm.* 2013, **15**, 5301; (*v*) N. Anastasiadis, D. Kalofolias, A. Philippidis, S. Tzani, C. Raptopoulou, V. Psycharis, C. Milios, A. Escuer, and S. Perlepes, *Dalton. Trans.*, 2015, **44**, 10200; (*w*) Y.-C. Liu and Z.-Y. Yang, *Eur. J. Med. Chem.*, 2009, **44**, 5080; (*x*) J. Zhu, H.-F. Song, P.-F. Yan, G.-F. Hou and G.-M. Li, *Cryst. Eng. Comm.*, 2013, **15**, 1747; (*y*) H.

Wang, C. Liu, T. Liu, S. Zeng, W. Cao, Q. Ma, C. Duan, J. Dou and J. Jiang, *Dalton Trans.*, 2013, **42**, 15355; (*z*) C.-J. Kuo, R. Holmberg, and P.-H. Lin, *Dalton Trans.*, 2015, **44**, 19758.

8. P.-H. Lin, T. Burchell, R. Clérac and M. Murugesu, *Angew. Chem. Int. Ed.*, 2008, **47**, 8848.
9. (*a*) Y.-C. Chen, J.-L. Liu, L. Ungur, J. Liu, Q.-W. Li, L.-F. Wang, Z.-P. Ni, L. Chibotaru, X.-M. Chen and M.-L. Tong, *J. Am. Chem. Soc.*, 2016, **138**, 2829; (*b*) J. Liu, Y.-C. Chen, J.-L. Liu, V. Vieru, L. Ungur, J.-H. Jia, L. Chibotaru, Y. Lan, W. Wernsdorfer, S. Gao, X.-M. Chen and M.-L. Tong, *J. Am. Chem. Soc.*, 2016, **138**, 5441. (c) M. U. Anwar, L. N. Dawe, S. S. Tandon, S. D. Bunge and L. K. Thompson, *Dalton Trans.*, 2013, **42**, 7781.
10. D. Pinkowicz, H. Southerland, C. Avendaño, A. Prosvirin, C. Sanders, W. Wernsdorfer, K. Pedersen, J. Dreiser, R. Clérac, J. Nehrkorn, G. Simeoni, A. Schnegg, K. Holldack and K. Dunbar, *J. Am. Chem. Soc.*, 2015, **137**, 14406.
11. W. Wernsdorfer, *Supercond. Sci Technol.*, 2009, **22**, 064013
12. N. Chilton, D. Collison, E. McInnes, R. Winpenny and A. Soncini, *Nat. Commun.*, 2013, **4**, 2551.
13. L. Ungur and L. Chibotaru, *Phys. Chem. Chem. Phys.*, 2011, **13**, 20086.

Chapter 3: Dinuclear and Octanuclear Lanthanide Complexes

From further experimentation with different bases and metal salts complexes with varying topologies and nuclearities were also discovered. Complexes of the general formula **[Ln_2(μ-OH)(vht)$(MeOH)_8$]Cl_3•1.5MeOH**, abbreviated **Ln_2** (where Ln = Dy, Er, Y) were synthesized and characterized using SQUID magnetometry and Single Crystal X-ray Diffraction. While the dinuclear complexes of the H_2vht did not exhibit magnet-like behaviour, field-induced SMM behaviour was observed in an octanuclear Dy^{III} cluster composed of two Dy_4 cubane structures. The octanuclear Dy^{III} complex (**Dy_8**) has the general formula **[Dy_8(μ_4-O)(μ_3-OH)$_8$(NO_3)$_2$(vht)$_4$(H_2O)$_8$](NO_3)$_4$** and possesses an energy barrier of 18 K.

3.1 Experimental

Materials. All manipulations were performed under aerobic conditions using chemicals and solvents from commercial sources (TCI, Alfa Aesar, and Strem Chemicals). Triethylamine was dried with KOH, distilled and stored over Linde type 4A molecular sieves before use. All other chemicals were used as received without further purification.

X-ray powder diffraction (XRPD). XRPD experiments were performed using a RIGAKU Ultima IV, equipped with a Cu-Kα radiation source (λ = 1.541836 Å) and a graphite monochromator. Scanning of the 2θ range was performed from 4-40°. XRPD patterns were consistent with simulated 2θ values generated from SCXRD data, with slight discrepancies in intensity attributed to preferred orientation.

Single-Crystal X-ray Diffraction Analysis. The crystals were mounted on a thin glass fibre using paraffin oil. Prior to data collection crystals were cooled to 200 K. Data were collected on a Bruker AXS SMART single-crystal diffractometer equipped with a sealed Mo tube source (λ = 0.71073 Å) APEX II CCD detector. Raw data collection and processing were performed with the APEX II software package from BRUKER AXS.[1] Semi empirical absorption corrections based on equivalent reflections were applied.[2] Direct methods yielded all non-H atoms, which were refined with anisotropic thermal parameters. All hydrogen atoms were calculated geometrically and were riding on their respective atoms. Crystallographic data for the **Dy_2**, **Er_2**, **Y_2** and **Dy_8** are depicted in Table 3.1.

Magnetic Measurements. Magnetic susceptibility measurements were collected using a MPMS-XL7 Quantum Design SQUID magnetometer. Direct current (dc) susceptibility data measurements were performed at temperatures ranging from 1.9 to 300 K, and between applied fields of -5 to 5 T. Measurements were performed on 16.0 (**Dy_2**), 20.1 (**Er_2**) and 14.4 mg (**Dy_8**) of crushed polycrystalline sample. The sample was wrapped in a polyethylene membrane. Alternating current (ac) susceptibility measurements were performed under an oscillating ac field of 3.78 Oe and ac frequencies ranging from 0.1 to 1488 Hz. Magnetization *vs.* field measurements were performed at 100 K in order to check for the presence of ferromagnetic impurities, which were found to be absent. Magnetic data was corrected for diamagnetic contributions using Pascal's constants.

Table 3.1. Crystallographic Data for compounds **Dy_2**, **Er_2**, **Y_2** and **Dy_8**

Compound	**Dy_2**	**Er_2**	**Y_2**	**Dy_8**
Empirical Formula	$C_{27.5}H_{55}Cl_3N_8O_{14.5}Dy_2$	$C_{27.5}H_{55}Cl_3N_8O_{14.5}Er_2$	$C_{27.5}H_{55}Cl_3N_8O_{14.5}Y_2$	$C_{72}H_{88}Dy_8N_{38}O_{51}$
Crystal system	Monoclinic	Monoclinic	Monoclinic	Monoclinic
Space group	$P2_1/n$	$P2_1/n$	$P2_1/n$	C2/c
a (Å)	11.7335(5)	11.7032(6)	11.6969(6)	30.488(5)
b (Å)	21.9355(8)	21.9069(11)	21.9005(12)	16.925(3)
c (Å)	18.3868(7)	18.3167(9)	18.3463(11)	26.054(6)
α (°)	90	90	90	90
β (°)	107.757(1)	107.699(2)	107.743(3)	114.901(1)
γ (°)	90	90	90	90
V (Å^3)	4506.9(3)	4473.8(4)	4476.2(4)	12194(4)
Z	4	4	4	4
ρ_{calc} (g cm^{-3})	1.711	1.738	1.505	1.962
λ (Å)	0.71073	0.71073	0.71073	0.71073
T (K)	200(2)	200(2)	200(2)	200(2)
μ (mm^{-1})	3.533	3.971	2.825	4.936
F (000)	2300	2316	2084	6888.0
Reflections Collected	42554	202879	67571	58380
Independent Reflections	10667	10704	10727	11050
Reflections with I > 2σ(I)	9819	9915	7922	7039
Goodness of fit on F^2	1.096	1.343	1.032	1.114
R_1, wR_2 (I > 2σ(I))[a]	0.0487, 0.1283	0.0344, 0.0847	0.0502, 0.1248	0.0728, 0.1770
R_1, wR_2 (all data)	0.0522, 0.1327	0.0387, 0.0877	0.0801, 0.1402	0.1240, 0.2273

[a] $R = R_1 = \sum||F_o| - |F_c||/\sum|F_o|$; $wR_2 = \{\sum[w(F_o^2 - F_c^2)^2]/\sum[w(F_o^2)^2]\}^{1/2}$; $w = 1/[\sigma^2(F_o^2)+(ap)^2 + bp]$,

where $p = [\max(F_o^2, 0) + 2F_c^2]/3$.

Synthesis of $[Ln_2(\mu\text{-}OH)(vht)(MeOH)_8]Cl_3 \bullet 1.5MeOH$ (Ln = Dy, Er, Y). To a solution of H_2vht (0.125 mmol, 51 mg) and $LnCl_3 \cdot 6H_2O$ (0.250 mmol) in 5 mL of MeOH, was added triethylamine (0.250 mmol, 35 µL). The mixture then turned a dark brown colour over the course of one minute. After 5 minutes the mixture was filtered and placed in a diethyl ether bath to facilitate crystal growth. After 3 days, black prismatic crystals suitable for X-ray diffraction were formed. (Yield = 54 mg, 37 %). IR for **Ln_2** (ATR, cm^{-1}): 3176 (br), 3066 (w), 3011 (w), 2838 (w), 2946 (w), 1604 (m), 1574 (m), 1520 (m), 1463 (m), 1408 (m), 1324 (w), 1292 (w), 1241 (w), 1221 (s), 1172 (w), 1111 (m), 1081 (m), 1051 (m), 1008 (m), 975 (m), 906 (w), 855 (m), 783 (w), 737 (m), 656 (m).

Synthesis of $[Dy_8(\mu_4\text{-}O)(\mu_3\text{-}OH)_8(NO_3)_2(vht)_4(H_2O)_8](NO_3)_4$ (Dy_8). To a stirred suspension of $Dy(NO_3)_3 \bullet 6H_2O$ (114 mg, 0.25 mmol) and H_2vht (51 mg, 0.125 mmol) in ethanol (10 mL, 95%) was added triethylamine (36 µL, 0.25 mmol). Several minutes after the addition the mixture takes on a dark brown colour. The mixture was allowed to continue stirring for 16 hours. The reaction was then filtered through Celite into a vial, sealed and left to stand at room temperature. After 3 days, black plate-shaped crystals suitable for X-ray diffraction were obtained. Yield = (25 mg, 20%). The IR and XRPD spectra of **Dy_8** are given in Figure 3.1.

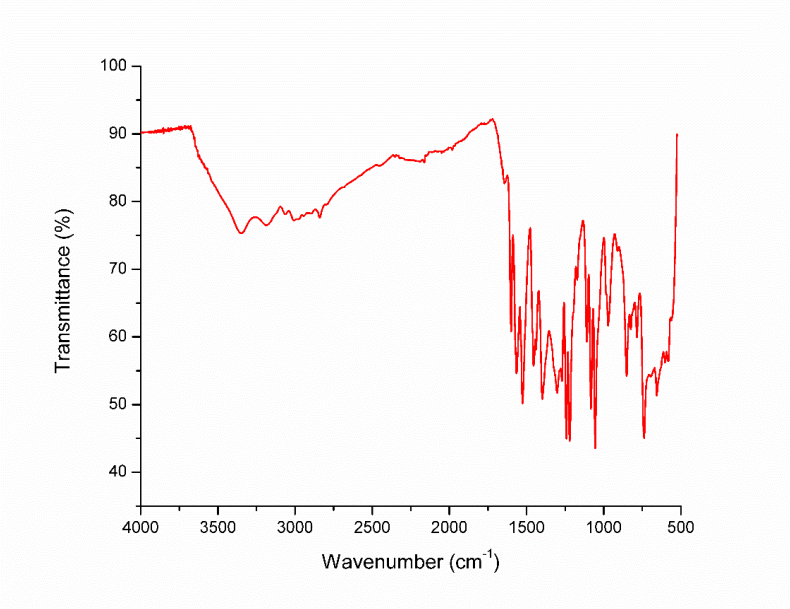

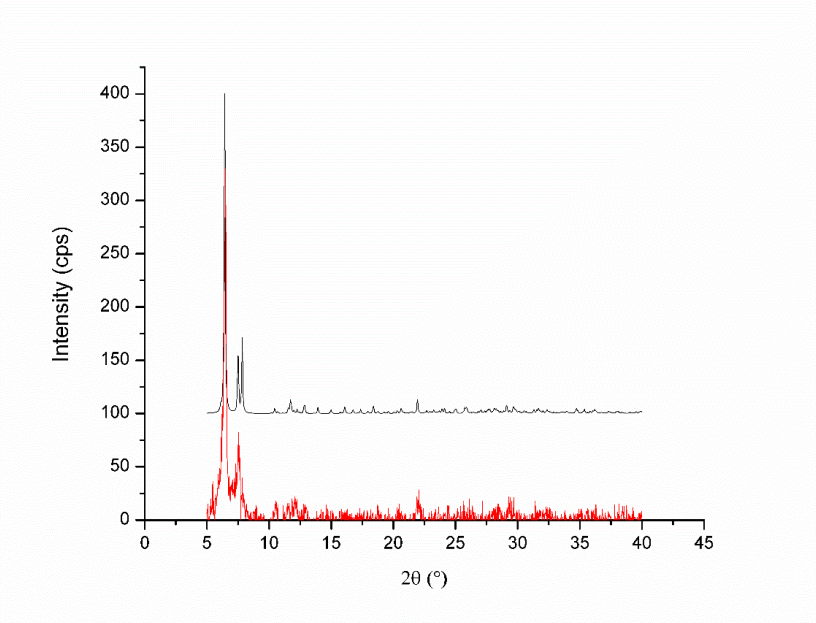

Figure 3.1. Infrared spectrum of **Dy_8** (top). X-ray powder diffraction spectrum of **Dy_8** (red) in the 5-40° 2θ region, as compared to the simulated pattern from Single Crystal X-ray Diffraction data (black) (bottom).

3.2 Structural Details of Dy_2. Due to all three complexes being isostructural the **Dy_2** analogue will be selected to be discussed in detail. Crystallographic data for the **Ln_2** compounds are given in Table 3.1. The complex crystallizes in the monoclinic $P2_1/n$ space group with Dy^{III} ions bridged by two substituents:

the central tetrazine ring of the vht^{2-} framework and a μ-hydroxido ligand (Figure 3.2). The intramolecular Dy^{III}-Dy^{III} distance is 4.25 Å, which is significantly longer than the Dy^{III}-Dy^{III} distance shown in the tetranuclear complex in the previous chapter. This larger intramolecular distance is also responsible for the large Dy1-O31-Dy2 bond angle of 141.9°. The tetrazine ring also exhibits a similar degree to distortion as the tetranuclear complex as a consequence of the coordination of Dy^{III}. Each of the two Dy^{III} ions is encapsulated within the tridentate pockets of the vht^{2-} ligand. For Dy1, donor atoms O9, N11 and N18 contribute to the coordination sphere from the vht^{2-}. The remainder of the coordination sphere of Dy1 is occupied by the bridging hydroxide O31 along with four methanol solvent molecules, rendering the ion eight-coordinate. Dy2 essentially mirrors the coordination geometry of Dy1 with both of the coordination polyhedra correlating best to triangular dodecahedra (D_{2d}) in accordance with SHAPE (Table 3.2).[3] The chloride ions Cl1 and Cl2 lie directly above and below the tetrazine ring. The average distance between Cl1 and the tetrazine N atoms is 3.51 Å and for Cl2 the average distance is 3.65 Å. These distances are evidence for moderately strong anion-π interactions between the chloride ions and the tetrazine ring.[4]

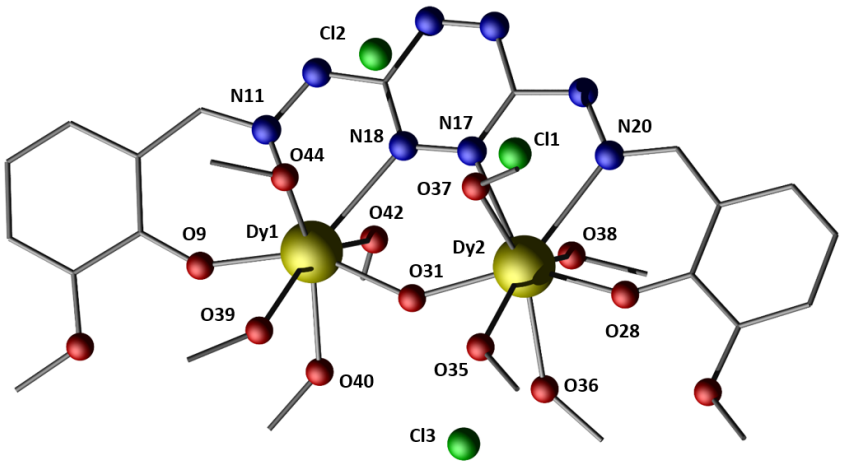

Figure 3.2. Partially labelled crystal structure of **Dy_2**. Colour code: yellow (Dy), red (O), blue (N), green (Cl). Hydrogen atoms are omitted for clarity. All unfilled vertices are carbon atoms.

Table 3.2. SHAPE constants for the Dy^{III} centers in **Dy_2**. The lowest SHAPE constants are highlighted in yellow.

SHAPE Code	Point Group	Description	Dy1	Dy2
OP-8	D8h	Octagon	31.253	31.279
HPY-8	C7v	Heptagonal bipyramid	23.724	23.604
HBPY-8	D6h	Hexagonal bipyramid	16.609	16.877
CU-8	Oh	Cube	10.428	10.335
SAPR-8	D4d	Square Antiprism	3.069	3.115
TDD-8	D2d	Triangular dodecahedron	0.480	0.502
JGBF-8	D2d	Johnson gyrobifastigium J26	12.800	12.533
JETBPY-8	D3h	Johnson elongated triangular bipyramid J14	28.159	27.992
JBTPR-8	C2v	Biaugmented trigonal prism J50	2.574	2.466
BTPR-8	C2v	Biaugmented trigonal prism	2.328	2.303
JSD-8	D2d	Snub diphenoid J84	1.758	1.618
TT-8	Td	Triakis tetrahedron	10.778	10.590
ETBPY-8	D3h	Elongated trigonal bipyramid	24.741	24.662

3.3 Magnetic Properties of Dy_2 and Er_2. The direct current (dc) magnetic susceptibility of **Dy_2** and **Er_2** were probed with a 1000 Oe magnetic field in the temperature range of 1.9 to 300 K (Figure 3.3). The room temperature χT value for the complexes are 28.2 and 22.5 cm^3 K mol^{-1} for **Dy_2** and **Er_2**, respectively. These values are in agreement with the expected values of 28.34 and 22.96 cm^3 K mol^{-1} (Dy^{III}: $^6H_{15/2}$, S = 5/2, L = 5, g = 4/3, χT = 14.17 cm^3 K mol^{-1}; Er^{III}: $^4I_{15/2}$, S = 3/2, L = 6, g = 6/5, χT = 11.48 cm^3 K mol^{-1}). Upon lowering the temperature the χT product of **Dy_2** steadily decreases with a notable downturn to 21.3 cm^3 K mol^{-1} at low temperature. In the case of **Er_2** the χT product begins to rapidly decrease at 50 K until reaching a final value of 11.4 cm^3 K mol^{-1}.

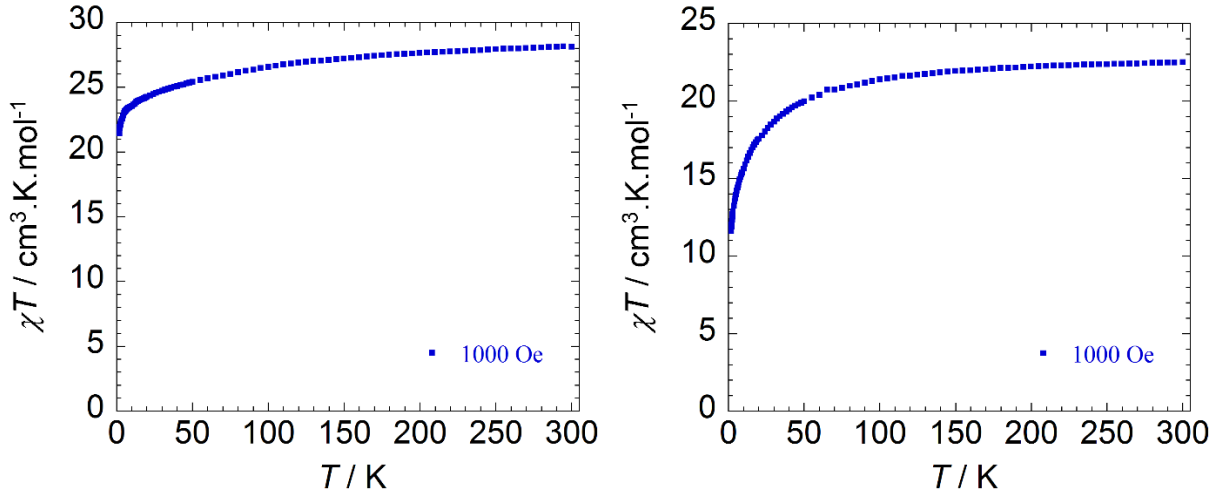

Figure 3.3. χT *vs. T* plots for **Dy_2** (left) and **Er_2** (right) under applied dc fields of 1000 Oe.

The elucidation of the exchange coupling for anisotropic lanthanide systems is not as straightforward as for isotropics systems (i.e Gd^{III}). The weak crystal field induces splitting of the m_j states of the lanthanide ions. The populations of these higher energy states progressively decrease with decreasing temperature, resulting in a decrease in magnetic moment that resembles antiferromagnetic coupling on a χT *vs.* T plot.[5] Without complete knowledge of the electronic structure of the lanthanide ions it is impossible to distinguish the exchange coupling from the thermal depopulation of excited states. Attempts to synthesize the Gd^{III} analogue were unsuccessful so an isotropic spin Hamiltonian could not be used to quantify the exchange coupling.

The field dependence of the magnetization was measured at temperatures between 1.8/1.9 and 7K (Figure 3.4). The M *vs.* H plots display a rapid increase in magnetization up to 1 T. In the case of **Dy_2** to the curve begins to approach saturation after 1 T and reaches a final value of 10.8 μ_B at 7 T. The M *vs.* H. plot for **Er_2** does not approach a saturation value but steadily rises to a value of 10.8 μ_B at 7 T. Both sets of M *vs.* HT^{-1} curves deviate from one another, indicating the presence of non-negligible magnetic anisotropy and/or low lying excited states for both **Dy_2** and **Er_2** (Figure 3.5).

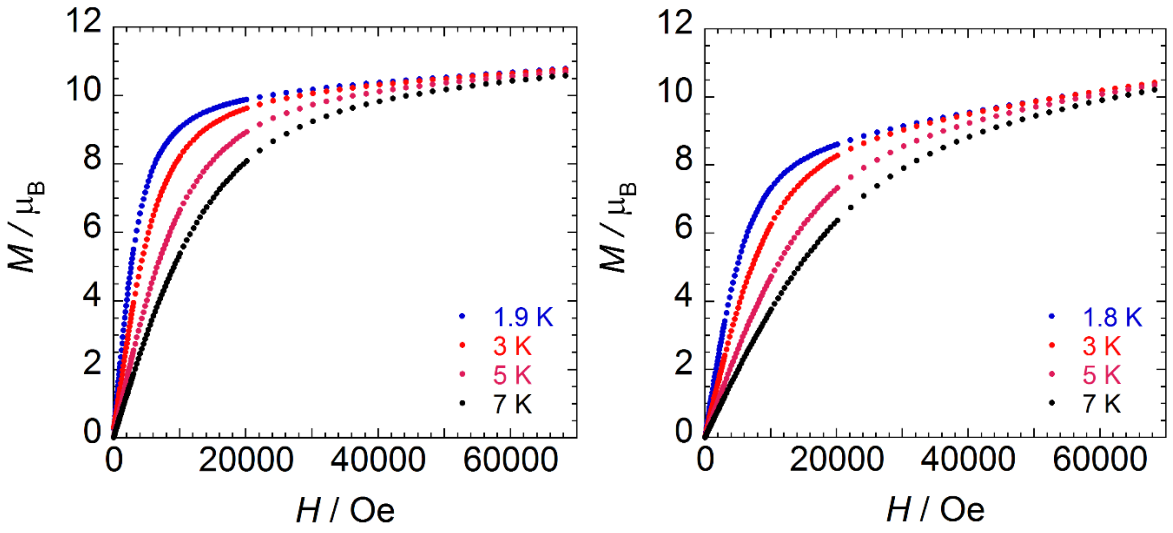

Figure 3.4. Field dependence of the magnetization, *M*, between 1.9 and 7 K for **Dy_2** (left) and 1.8 and 7 K for **Er_2** (right).

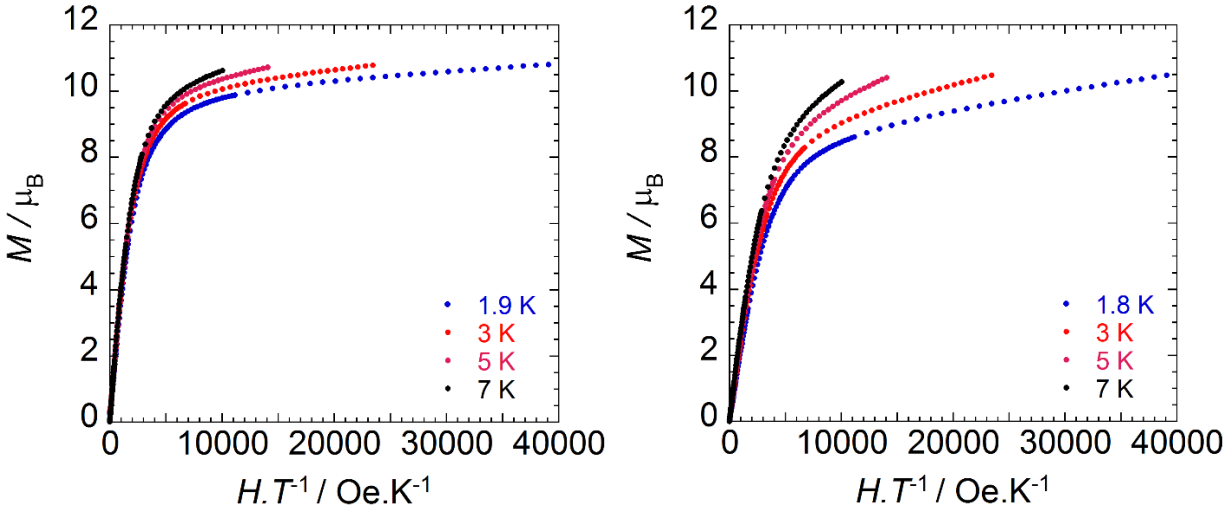

Figure 3.5. Reduced magnetization plots from 1.9 and 7 K for **Dy_2** (left) and 1.8 and 7 K for **Er_2** (right).

No peaks in the ac susceptibility measurements could be resolved with wave frequencies up to 1488 Hz for either of these compounds. This may be attributed to the large intramolecular distance between the two Ln^{III} ions which would diminish the strength of the dipolar coupling.

3.4 Structural Details of Dy_8. The complex crystallizes in the monoclinic space group C2/c, with the lanthanide ions arranged into two $[Dy_4(\mu_3\text{-}OH)_4]^{8+}$ cubane structures, with one cubane within each asymmetric unit (Figure 3.6). Crystallographic Data for **Dy_8** are given in Table 3.3. To date there are only 3 previously reported Dy_8 complexes that possess this $[Dy_4(\mu_3\text{-}OH)_4]^{8+}$ structure.[6] The bond distances pertaining to these cubanes range from 2.32 to 2.49 Å with Dy^{III}-O-Dy^{III} angles ranging from 97.2 to 111.6°, depicting highly distorted cubane structures. The coordination geometries of the Dy^{III} metal centers were assessed using SHAPE.[7] The Dy1 and Dy3 metal centers possess an intermediate geometry between a square antiprism (D_{4d}) and a triangular dodecahedron (D_{2d}) (Figure 3.7). Both the Dy2 and Dy4 metal centers possess more distorted geometries correlating best to a Johnson gyrobifastigium (D_{2d}) and a biaugmented trigonal prism (C_{2v}), respectively (Table 3.4). Linking these two cubanes together is a central $\mu_4\text{-}O^{2-}$ ligand accompanied by all four vht^{2-} ligands providing μ-phenoxido bridging motifs. Each vht^{2-} ligand encapsulates two Dy^{III} ions within both of the large coordination pockets which consist of an imine nitrogen, a phenoxide oxygen and a tetrazine nitrogen as donor atoms.

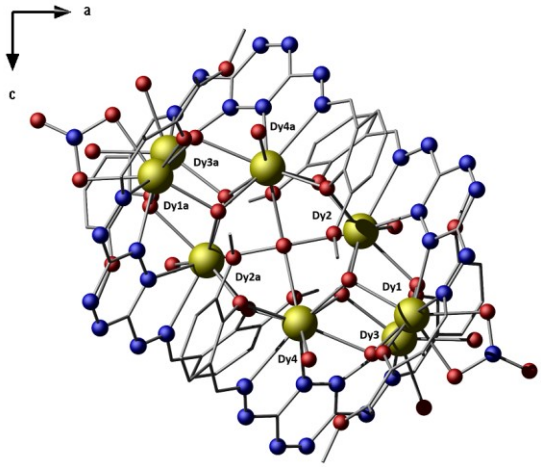

Figure 3.6. Crystal structure of **Dy_8** viewed along the b axis. Colour code: yellow (Dy), red (O), blue (N). Hydrogen atoms are omitted for clarity. All unfilled vertices are carbon atoms.

The coordination spheres of Dy1 and Dy3 are completed by a terminal, bidentate nitrate anion and two water molecules, respectively, while both the coordination spheres Dy2 and Dy4 are completed by one water molecule each. This renders all of the Dy^{III} ions to be 8-coordinate. Four non-coordinating nitrate anions occupy the lattice to balance the charge of the cationic complex, ultimately leading to the complete formula of $[Dy_8(\mu_4\text{-}O)(\mu_3\text{-}OH)_8(NO_3)_2(vht)_4(H_2O)_8\}(NO_3)_4$ for the molecule. The electron density corresponding to approximately 19.4 highly disordered water molecules observed during the data refinement was removed using the SQUEEZE routine implemented in PLATON.[8]

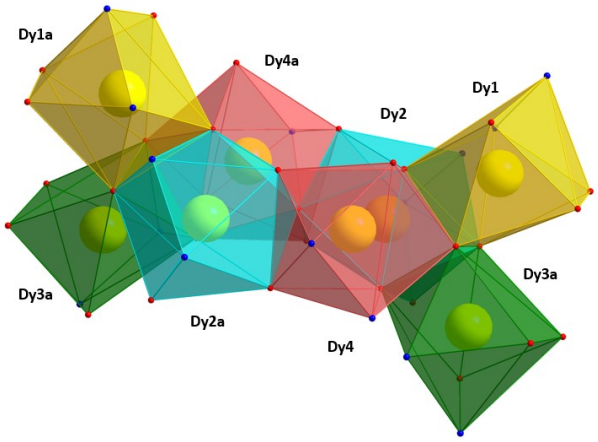

Figure 3.7. Coordination polyhedra of **Dy_8**. Colour code: yellow (Dy), red (O), blue (N)

Table 3.4. SHAPE constants for the Dy^{III} centers in **Dy_8**. The lowest shape constants are highlighted in yellow.

SHAPE Code	Point Group	Description	Dy1	Dy2	Dy3	Dy4
OP-9	D8h	Octagon	31.111	27.309	29.970	28.024
HPY-8	C7v	Heptagonal pyramid	20.989	18.040	20.534	18.069
HBPY-8	D6h	Hexagonal bipyramid	13.794	12.442	13.655	13.006
CU-8	Oh	Cube	9.046	18.640	7.809	18.457
SAPR-8	D4d	Square antiprism	2.175	12.697	1.495	11.537
TDD-8	D2d	Triangular dodecahedron	2.289	10.336	2.353	9.298
JGBF-8	D2d	Johnson gyrobifastigium J26	14.099	7.226	14.567	7.728
JETBPY-8	D3h	Johnson elongated triangular bipyramid J14	26.813	21.578	26.801	21.266
JBTPR-8	C2v	Biaugmented trigonal prism J50	3.833	9.853	4.037	8.932
BTPR-8	C2v	Biaugmented trigonal prism	3.045	8.445	3.299	7.427
JSD-8	D2d	Snub diphenoid J84	5.696	11.302	6.048	10.645
TT-8	Td	Triakis tetrahedron	9.877	19.014	8.544	18.968
ETBPY-8	D3h	Elongated trigonal bipyramid	21.980	17.165	21.583	16.813

3.5 Magnetic Properties of Dy_8. The direct current (dc) magnetic susceptibility of the complex was probed with a 1000 Oe magnetic field in the temperature range of 1.9 to 300 K (Figure 3.8). The room temperature χT value for the complex is 112.3 cm^3 K mol^{-1} which is in good agreement with the theoretical value of 113.36 cm^3 K mol^{-1} for eight non-interacting Dy^{III} ions (Dy^{III}: $^6H_{15/2}$, S = 5/2, L = 5, g = 4/3, χT = 14.17 cm^3 K mol^{-1}). Upon lowering the temperature the χT product gradually decreases and then quickly declines to a value of 80.0 cm^3 K mol^{-1}. This decrease is attributed to the thermal depopulation of excited Stark levels by crystal field splitting and/or antiferromagnetic coupling between the Dy^{III} metal centers.[5] The field dependence of the magnetization was measured at temperatures between 1.8 and 7K (Figure 3.8). The M *vs.* H plot displays a rapid increase in magnetization up to 1 T

where the curves begin to approach saturation. At saturation the curves reach a magnetization of 40.1 μ_B. The corresponding M *vs.* HT^{-1} curves deviate from one another, indicating the presence of non-negligible magnetic anisotropy and/or low lying excited states (Figure 3.8).

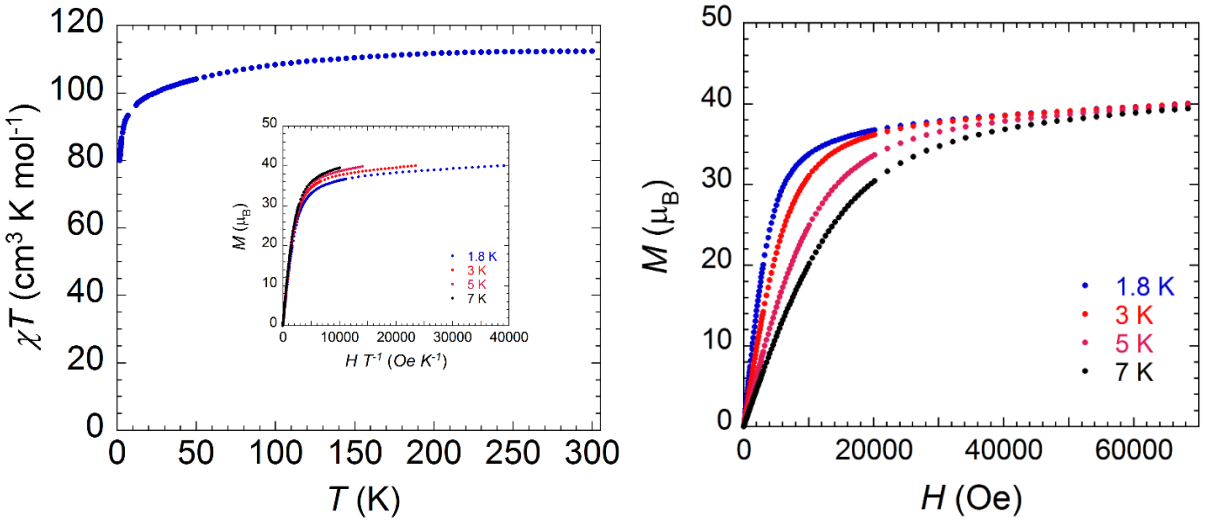

Figure 3.8. Temperature dependence of the χT product at 1000 Oe; Inset: M *vs.* HT^{-1} plot from 1.8 to 7 K (left). Field dependence of the magnetization, *M*, between 1.8 and 7 K for **Dy_8** (right).

In order to assess the relaxation dynamics of the complex, alternating current (ac) susceptibility measurements were performed with an ac field of 3.78 Oe oscillating at frequencies up to 1488 Hz along with an applied dc field of 1500 Oe. As shown in Figure 3.9, the shifting of peak maxima in both the in-phase and out-of-phase susceptibility curves are indicative of slow magnetic relaxation.

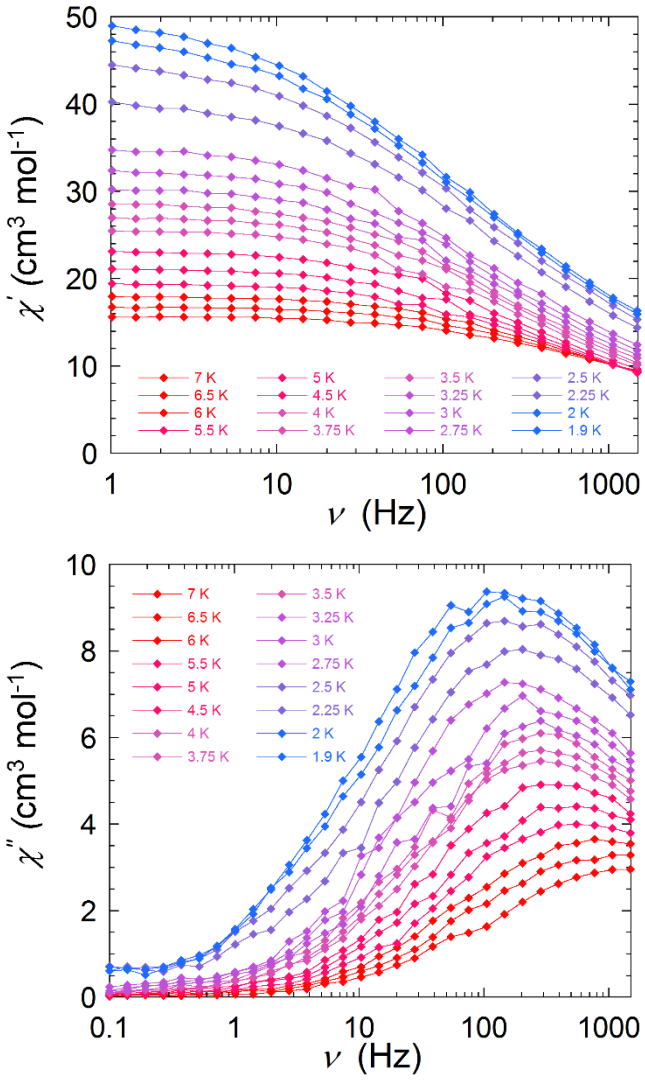

Figure 3.9. In-phase magnetic susceptibility (χ') *vs.* frequency (top) and out-of-phase magnetic susceptibility *vs.* temperature (bottom) for **Dy_8**.

The magnetization reversal barrier (U_{eff}) and pre-exponential factor (τ_0) were obtained by fitting the shifting peak maxima with an Arrhenius equation ($\tau = \tau_0 \exp(U_{eff}/k_BT)$, which yielded a barrier of U_{eff}/k_B = 18 K with $\tau_0 = 9.39 \times 10^{-6}$ s (Figure 3.10).

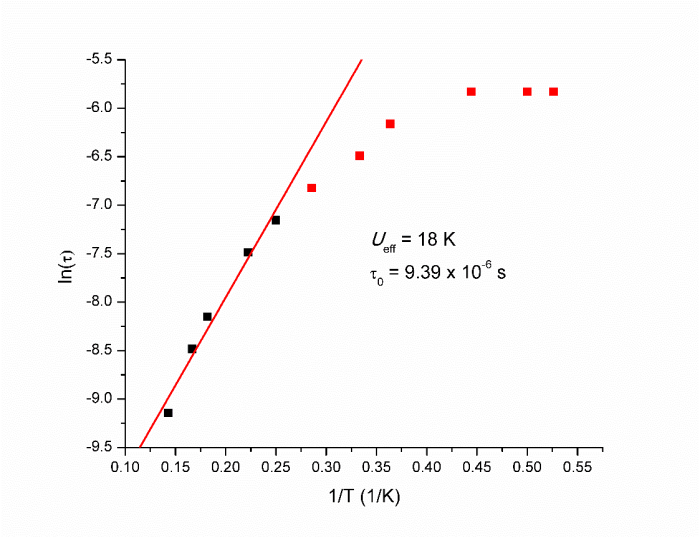

Figure 3.10. ln(τ) *vs.* 1/*T* Arrhenius plot for **Dy_8**.

The relaxation dynamics were also represented using a Cole-Cole plot (Figure 3.11). The semi-circular shape of the curves at varying temperatures is indicative of a single relaxation process.

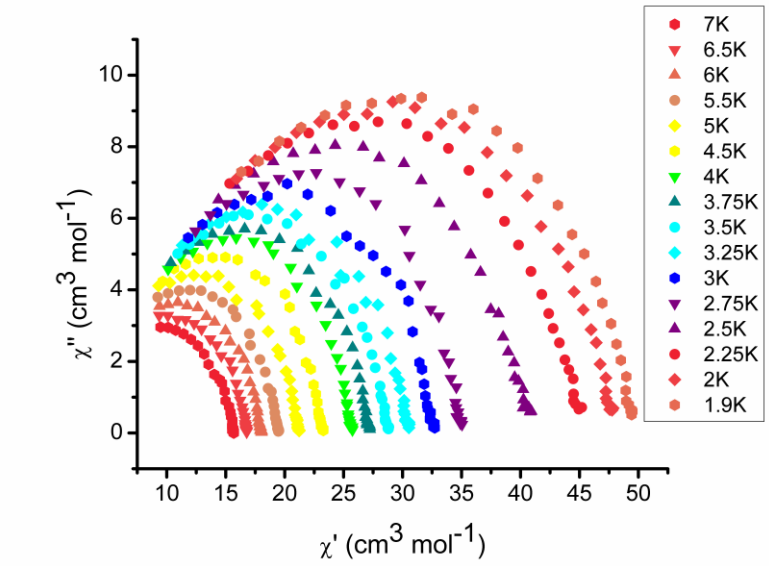

Figure 3.11. Cole-Cole plot for frequency dependent ac susceptibility data of **Dy_8**

Electrostatic modelling of the lowest lying Kramers doublets for each Dy^{III} ion using Magellan[12] reveals that the anisotropy axes of Dy2 and Dy4 are oriented towards the central O^{2-} bridging ligand O67. The Dy1 and Dy3 axes align with the most adjacent phenoxide donor atoms O9 and O39, respectively (Figure 3.12).

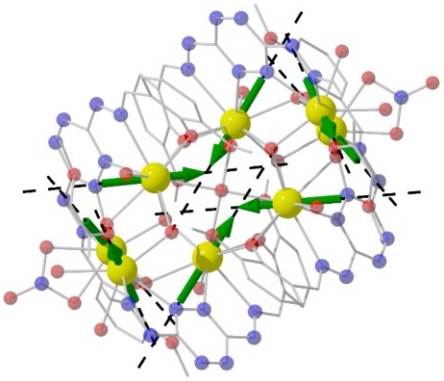

Figure 3.12. Orientation of the magnetic anisotropy of the $m_j = \pm 15/2$ states of the Dy^{III} ions. Colour code: yellow (Dy), red (O), blue (N). Hydrogen atoms are omitted for clarity. All unfilled vertices are carbon atoms.

3.6 Conclusions. Through slight variations in reaction conditions two different lanthanide complexes were formed from H_2vht. The lack of SMM behaviour of the **Ln_2** complexes is attributed to the large intramolecular distances between the metal ions. An octanuclear Dy^{III} field-induced SMM was obtained with an unprecedented μ_4-oxo bridge between two cubane motifs. The **Dy_8** complex ultimately yielded a modest energy barrier of 18 K.

3.7 References

1. APEX Software Suite v.2012; Bruker AXS: Madison, WI, 2005.
2. R. Blessing, *Acta. Crystallogr. A.*, 1995, **51**, 33.
3. D. Casanova, M. Llunel, P. Alemany and S. Alvarez, *Chem. Eur. J.*, 2005, **11**, 1479.

4. A. Robertazzi, F. Krull, E.-W. Knapp and P. Gamez, *Cryst. Eng. Comm.*, 2011, **13**, 3293.

5. M. L. Kahn, R. Ballou, P. Porcher, O. Kahn and J. P. Sutter, Chem.–Eur. J., 2002, 8, 525–531.

6. (*a*) Y.-L. Miao, J.-L. Liu, J.-Y. Li, J.-D. Leng, Y.-C. Ou and M.-L. Tong, *Dalton Trans.*, 2011, **40**, 10229; (*b*) H. Ke, P. Gamez, L. Zhao, G.-F. Xu, S. Xue and J. Tang, *Inorg. Chem.*, 2010, **49**, 7549; (*c*) M. Fang, H. Zhao, A. Prosvirin, D. Pinkowicz, B. Zhao, P. Cheng, W. Wernsdorfer, E. Brechin and K. Dunbar, *Dalton Trans.*, 2013, **42**, 14693.

7. D. Casanova, M. Llunel, P. Alemany and S. Alvarez, *Chem. Eur. J.*, 2005, **11**, 1479.

8. (*a*) A. Spek, PLATON; University of Utrecht: Utrecht, The Netherlands, 2008. (*b*) A. Spek, *Acta Crystallogr. D*. 2009, **65**, 148.

9. N. Chilton, D. Collison, E. McInnes, R. Winpenny and A. Soncini, *Nat. Commun.*, 2013, **4**, 2551.

Chapter 4: The Design of Tetrazine-Containing Schiff Base Ligands

In order to promote strong exchange coupling between lanthanide ions and radicals the ligand design would have to incorporate a moiety that readily undergoes a one-electron redox process to form a radical species. Tetrazines appear to be the most promising candidate for this role since they not only undergo reversible one-electron reductions to form anion radicals but they also exhibit remarkable stability. There are multiple examples of stabilized tetrazine radical coordination complexes.[1]

To observe direct metal-radical interactions a terpyridine-like motif was sought after. To achieve this topology, 3-hydrazinyl-tetrazine was prepared *in situ* as the source of the tetrazine by nucleophilic substitution of the precursor 3-(3,5-dimethyl-1H-pyrazol-1-yl)-1,2,4,5-tetrazine with hydrazine. A subsequent Schiff base condensation with 2-pyridinecarboxaldehyde yielded the target tridentate tetrazine ligand named (2-pyridinylmethylidene)-3-hydrazinyl-1,2,4,5-tetrazine (Htzpy) (Scheme 4.1).

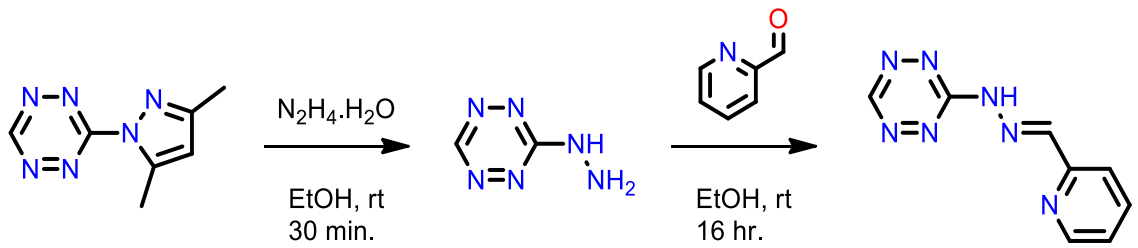

Scheme 4.1. Synthesis of (2-pyridinylmethylidene)-3-hydrazinyl-1,2,4,5-tetrazine (Htzpy).

4.1 Synthesis of (2-pyridinylmethylidene)-3-hydrazinyl-1,2,4,5-tetrazine (Htzpy). 3-(3,5-dimethyl-1H-pyrazol-1-yl)-1,2,4,5-tetrazine was synthesized according a previously reported procedure,[2] with an additional purification step performed by recrystallization from EtOH. To a stirred suspension of 3-(3,5-

dimethyl-1H-pyrazol-1-yl)-1,2,4,5-tetrazine (1.76 g, 0.01 mol) in EtOH (20 mL, 99%) was added hydrazine monohydrate (0.485 mL, 0.01 mol). Upon addition the reaction takes on a dark red colour. The reaction was allowed to stir for 30 minutes at room temperature. 2-pyridinecarboxaldehyde (0.951 mL, 0.01 mol) was then added to the mixture. The reaction mixture continued to stir at room temperature for an additional 16 hours, during which a bright orange precipitate slowly began to form. The mixture was then filtered, the solid was rinsed with EtOH, and dried under vacuum. Yield (80%, 1.61 g). ^{1}H NMR (DMSO-d_6, 400 MHz) δ = 7.39 (m, 1H, Py), 7.86 (m, 1H, Py), 7.97 (m, 1H, Py), 8.34 (s, 1H, N=CH), 8.59 (m, 1H, Py), 10.02 (s, 1H, Tz), 12.60 (s, 1H, NH) Anal. Calcd. For $C_8H_7N_7$: C, 47.76; H, 3.51; N, 48.73. Found: C, 48.05; H, 3.20; N, 48.52.

4.2 Structural Details of Htzpy. In order to obtain precise structural details of Htzpy single-crystal X-ray diffraction was performed. Crystals suitable for X-ray diffraction were formed by recrystallization from acetone. The ligand Htzpy crystallizes in the monoclinic $P2_1/c$ space group (Figure 4.1). The ligand is comprised of three key moieties: the pyridine ring, the hydrazone linker and the terminal tetrazine ring. The C-N bond distances in the tetrazine ring vary from 1.35 to 1.41 Å, giving rise to a significantly distorted tetrazine structure. However the N-N bond distances of 1.32 and 1.33 Å are consistent with previously reported tetrazine compounds.[1b] The ligand possesses a large tridentate coordination pocket with donor atoms consisting of the pyridyl N atom, N1,the hydrazone N atom, N2, and either tetrazine N atoms, N4 or N6. This pocket has a similar topology to that of the 2,2':6',2''-terpyridine coordination pocket. The ^{1}H NMR of Htzpy consists of three singlets and four pyridyl multiplets (Figure 4.2). The characteristic imine proton of the ligand gives a singlet at 8.34 ppm. The proton from the terminal tetrazine moiety gives a singlet at 10.02 ppm. The remaining N-H proton gives a singlet at 12.60 ppm.

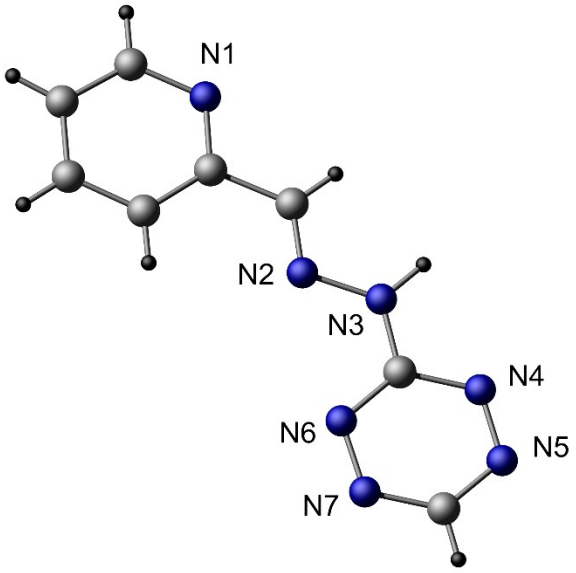

Figure 4.1. Crystal structure of Htzpy. Colour code: Blue (N), Gray (C), Black (H).

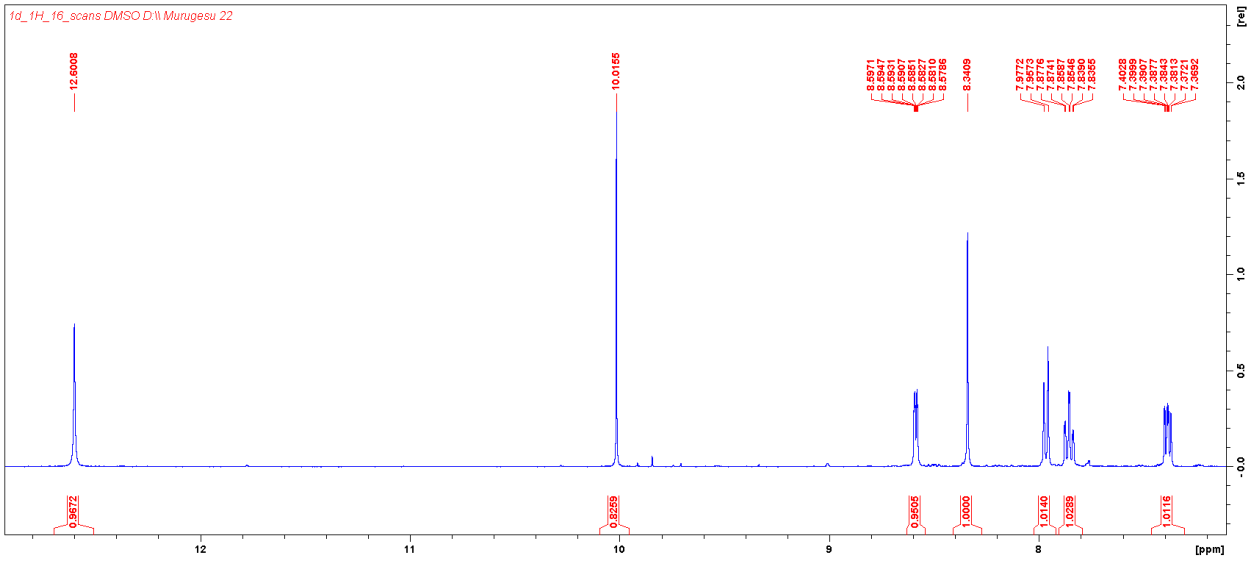

Figure 4.2. ^{1}H NMR spectrum of Htzpy in DMSO-d_6.

4.3 Electrochemical Properties of Htzpy. The electrochemical properties of Htzpy were then assessed by cyclic voltammetry in order to observe the reduction potential of the ligand and to see whether or not the ligand confers stability to the anion radical species (Figure 4.3). Cyclic voltammetry was performed

using a BASi Epsilon potentiostat employing a glass cell and platinum wires for working, counter and pseudo-reference electrodes. The measurements were carried out in acetonitrile which was dried by an Innovative S3 Technology PureSolv solvent system and stored over 4 Å molecular sieves. The solution consisted of 0.1 M tetrabutylammonium hexafluorophosphate as a supporting electrolyte. The measurements were taken with a sweep rate of 100 mV/s. Ferrocene was used as an internal standard and the potentials are referenced to the Fc/Fc+ redox couple.

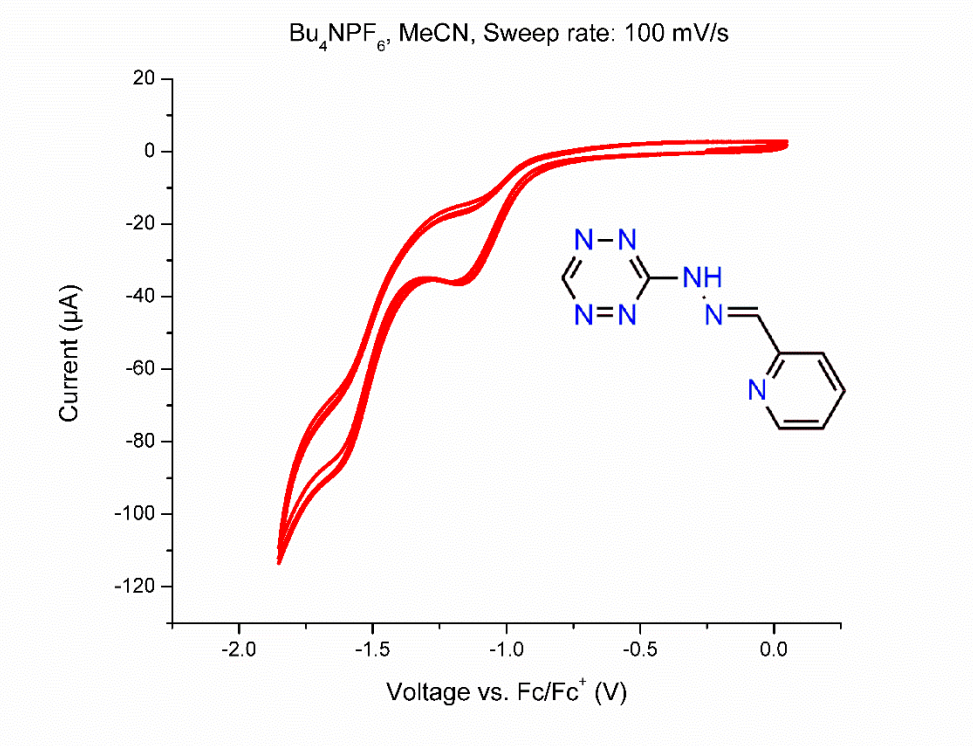

Figure 4.3. Cyclic voltammogram of (2-pyridinylmethylidene)-3-hydrazinyl-1,2,4,5-tetrazine (Htzpy).

Upon reduction Htzpy undergoes an irreversible process at -1.13 V, indicating that the ligand does not sufficiently stabilize the anion radical intermediate. Further investigation was employed in an attempt to understand this reduction process.

In order to replicate the electrochemical reduction of Htzpy, cobaltocene was used as a one-electron reducing agent (Scheme 4.2). The redox couple of cobaltocene lies at -1.33 V *vs.* ferrocene,[3] which is a sufficiently large reduction potential to invoke the irreversible process displayed in the cyclic voltammagram. The resulting compound from this reaction was in fact not an anion radical species but instead a deprotonated $tzpy^-$ with a cobaltocenium cation.

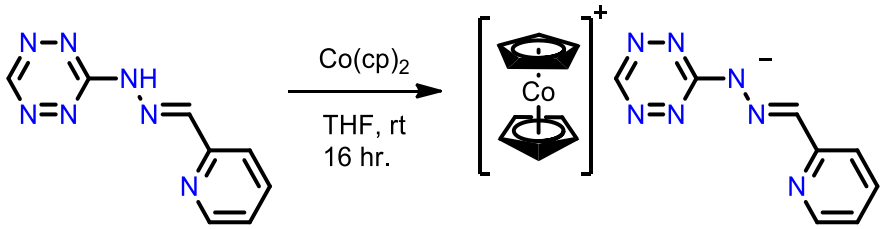

Scheme 4.2. Synthesis of $[Co(cp)_2][tzpy]$.

4.4 Synthesis of $[Co(cp)_2][tzpy]$. To a stirred suspension of Htzpy (1.00 g, 4.97 mmol) in THF (20 mL) was added cobaltocene (0.99 g, 5.22 mmol) under nitrogen. Upon addition the reaction mixture changes to a dark brown colour. The reaction mixture was allowed to stir for 16 hours at room temperature. The mixture was then filtered, the solid was rinsed with THF, and dried under vacuum. The product was then used without further purification. Yield (75 %, 1.45 g).

In looking for paramagnetic shifting from a potential radical species within the ^1H NMR spectrum the spectral window was expanded to -300 and +300 ppm on an a Bruker Avance II 300 spectrometer (Figure 4.4). No evidence of paramagnetic shifting was observed. However, slight broadening of the proton signals was observed which may be attributed trace paramagnetic impurities from the cobaltocene. Due to this broadening the coupling of the pyridyl multiplets could not be resolved and so the identity of most of the peaks cannot be determined. The only clearly identifiable signals in the spectrum are the chloroform solvent peak at 7.26 ppm and the peak from the cp ring protons at 5.74

ppm which has an integration corresponding to 10 protons. When comparing the spectrum of $[Co(cp)_2][tzpy]$ to Htzpy the integration for $[Co(cp)_2][tzpy]$ without the cp ring accounts for six protons, indicating that there is one less proton than in the Htzpy spectrum, which indicates the loss of the NH proton.

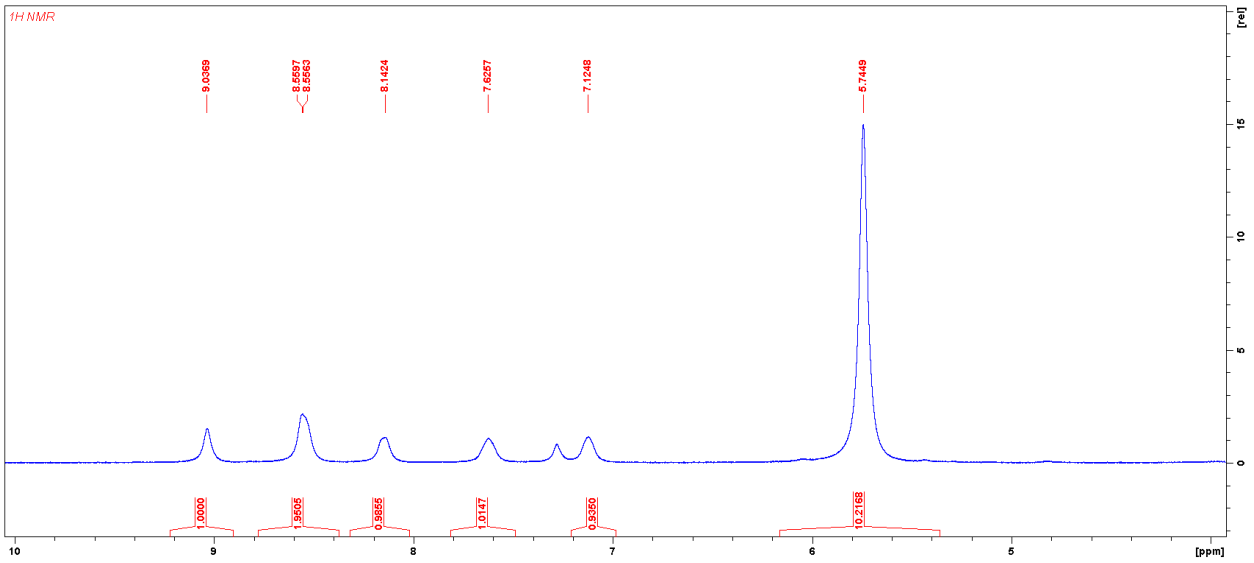

Figure 4.4. ^1H NMR spectrum of $[Co(cp)_2][tzpy]$ in $CDCl_3$.

4.5 Structural Details of $[Co(cp)_2][tzpy]$. Further investigation of the structure of $[Co(cp)_2][tzpy]$ was carried out by SCXRD. Crystals suitable for X-ray diffraction were obtained by dissolving $[Co(cp)_2][tzpy]$ in neat acetonitrile followed by diffusion of neat diethyl ether over two days. Upon refinement of the crystal structure no q peaks were observed in the vicinity of the hydrazinyl nitrogen atom, N3, which is a further indication of deprotonation (Figure 4.5). The compound $[Co(cp)_2][tzpy]$ crystallizes in the triclinic P-1 space group. The mean Co-C bond distance of the cobaltocenium cations of 2.02 Å is in excellent agreement with the mean Co-C bond distances of 142 previously reported structures containing $[Co(cp)_2]^+$ (2.020(25) Å), solidifying that the Co ions are in the 3+ oxidation state. As an additional comparison the crystal structure of cobaltocene itself has a mean value of 2.100(9) Å for its Co-C

distances,[4] which is significantly larger compared to the cation. The The N-N bond distances of the tetrazine ring range from 1.30 to 1.32 Å, indicating that the tetrazine ring is not in the semi-reduced state. In comparison, the N-N bond distances for known coordination complexes containing tetrazine anion radicals can range from 1.38 to 1.43 Å.[5] Crystallographic data for Htzpy and $[Co(cp)_2][tzpy]$ are given in Table 4.1.

The irreversible reduction process could then be attributed to the cobaltocene reducing the NH proton to a hydrogen radical which then immediately combines with another hydrogen radical to form hydrogen gas. In order to unambiguously determine that deprotonation of N3 has occurred a methylation was performed using $[Co(cp)_2][tzpy]$ and methyl iodide (Scheme 4.3). This reaction resulted in the regioselective methylation of the $tzpy^-$ fragment at nitrogen N3 since the deprotonated nitrogen is the most nucleophilic donor atom. This reaction yielded the compound (2-pyridinylmethylidene)-3-(methylhydrazinyl)-1,2,4,5-tetrazine (Metzpy). Attempts to methylate Htzpy using sodium hydride as a base were unsuccessful and attempts to perform a one-pot synthesis using cobaltocene resulted in methylation of multiple sites of the $tzpy^-$ framework.

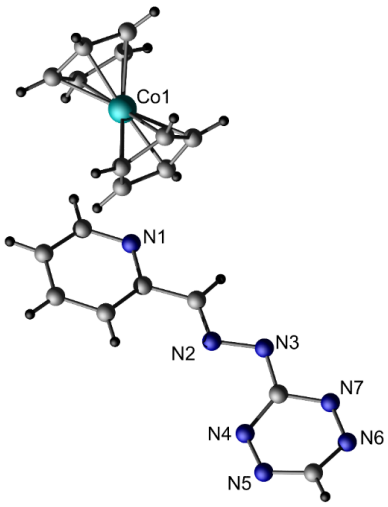

Figure 4.5. Crystal structure of $[Co(cp)_2][tzpy]$ Colour code: Turquoise (Co), Blue (N), Gray (C), Black (H).

Table 4.1. Crystallographic Data for Htzpy and $[Co(cp)_2][tzpy]$.

Compound	Htzpy	$[Co(cp)_2][tzpy]$
Empirical Formula	$C_8H_7N_7$	$C_{18}H_{16}CoN_7$
Crystal system	Monoclinic	Triclinic
Space group	$P2_1/c$	P-1
a (Å)	6.863(9)	8.8529(11)
b (Å)	19.77(3)	11.0425(14)
c (Å)	7.125(10)	18.499(2)
α (°)	90	90.727(2)
β (°)	109.804(15)	90.789(2)
γ (°)	90	108.245(2)
V (Å^3)	910(2)	1717.07(4)
Z	4	4
ρ_{calc} (g cm^{-3})	1.469	1.506
λ (Å)	0.71073	0.71073
T (K)	200(2)	239(2)
μ (mm^{-1})	0.103	1.017
F (000)	416	800
Reflections Collected	14910	20666
Independent Reflections	14910	8239
Reflections with I > 2σ(I)	7485	4686
Goodness of fit on F^2	0.974	0.985
R_1, wR_2 (I > 2σ(I))[a]	0.0578, 0.1359	0.0385, 0.0802
R_1, wR_2 (all data)	0.1302, 0.1700	0.0956, 0.1015

[a] $R = R_1 = \sum||F_o| - |F_c||/\sum|F_o|$; $wR_2 = \{\sum[w(F_o^2 - F_c^2)^2]/\sum[w(F_o^2)^2]\}^{1/2}$; $w = 1/[\sigma^2(F_o^2)+(ap)^2 + bp]$, where $p = [\max(F_o^2, 0) + 2F_c^2]/3$.

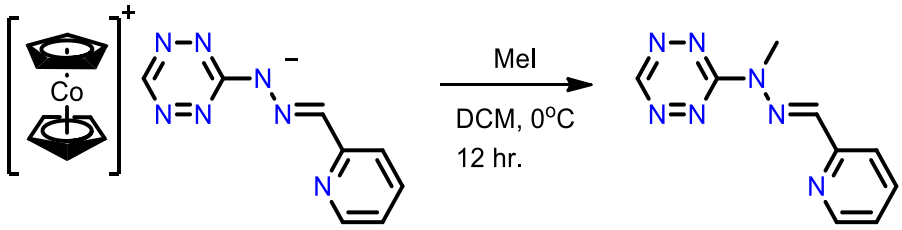

Scheme 4.3. Synthesis of (2-pyridinylmethylidene)-3-(methylhydrazinyl)-1,2,4,5-tetrazine (Metzpy).

4.6 Synthesis of (2-pyridinylmethylidene)-3-(methylhydrazinyl)-1,2,4,5-tetrazine (Metzpy). A stirred solution of $[Co(cp)_2][tzpy]$ (1.45g, 3.72 mmol) in DCM (30 mL) was cooled to 0°C under nitrogen. Methyl iodide (232 μL, 3.72 mmol) was added to the solution and upon complete addition the reaction was allowed to warm to room temperature. The reaction mixture continued to stir for 12 hours. The reaction mixture was then filtered through silica gel with subsequent additions DCM as eluent. The solvent was removed under reduced pressure to afford a bright red solid. Yield (90%, 0.72 g). ^{1}H NMR ($CDCl_3$, 400 MHz) δ = 3.86 (m, 3H, CH_3), 7.25 (m, 1H, Py), 7.73 (m, 1H, Py), 8.14 (s, 1H, N=CH), 8.19 (m, 1H, Py), 8.58 (m, 1H, Py), 9.83 (s, 1H, Tz) Anal. Calcd. for $C_9H_9N_7$: C, 50.23; H, 4.22; N, 45.56. Found: C, 50.15; H, 3.95; N, 44.68. ^{13}C ($CDCl_3$, 400 MHz) δ = 162.4, 154.4, 153.5, 149.3, 143.0, 136.8, 124.2, 120.9, 30.9.

4.7 Structural details of Metzpy. Since the crystal structure of Metzpy is yet to be obtained. The structural description will therefore be made based on spectroscopic methods. ^{1}H NMR reveals that Metzpy shows similar signals to Htzpy where both spectra have a tetrazine singlet, an imine singlet and four pyridyl multiplets, albeit at different chemical shifts (Figure 4.6). In the case of Metzpy the singlets at 9.83 and 8.14 ppm correspond to the tetrazine proton and the imine proton, respectively. The difference in the spectra arises from the disappearance of the N-H proton signal and the appearance of a methyl singlet at 3.86 ppm.

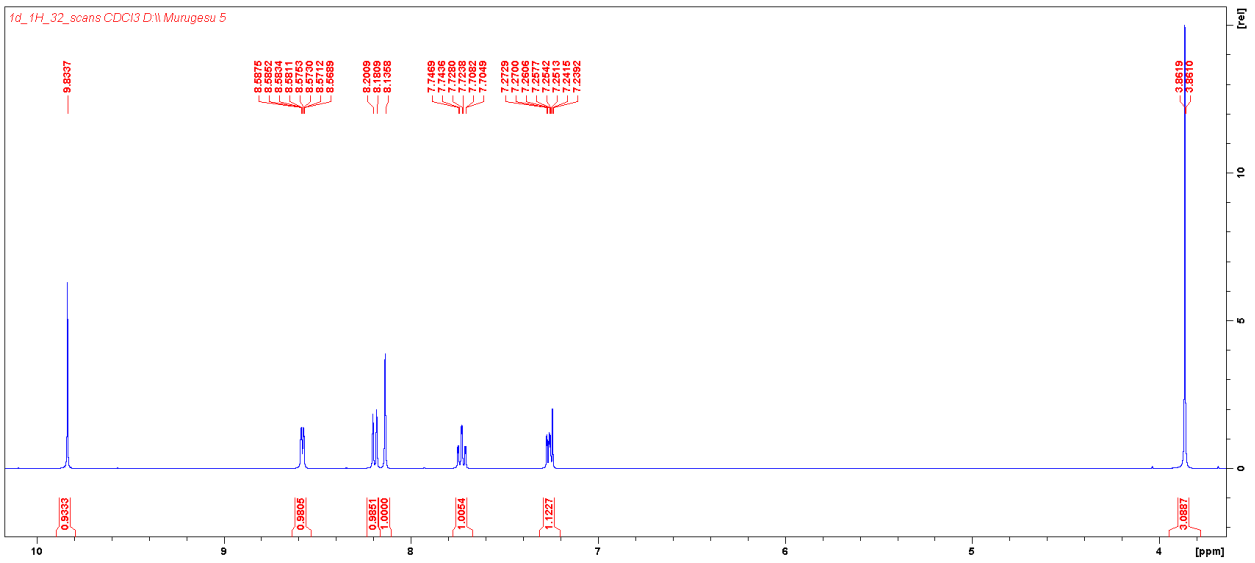

Figure 4.6. ^{1}H NMR spectrum of Metzpy in $CDCl_3$

Comparison of the IR spectra of Htzpy, $[Co(cp)_2][tzpy]$ and Metzpy highlights the successive changes in functionality of the compounds (Figure 4.7). When comparing Htzpy to $[Co(cp)_2][tzpy]$ the N-H stretching bands from 2750 to 3250 cm^{-1} of Htzpy disappear and are replaced by the C-H stretching bands of the cp ring from 2875 cm^{-1} to 3200 cm^{-1}. The successive methylation to Metzpy then results in C-H stretching bands that are significantly weaker in intensity within the same range.

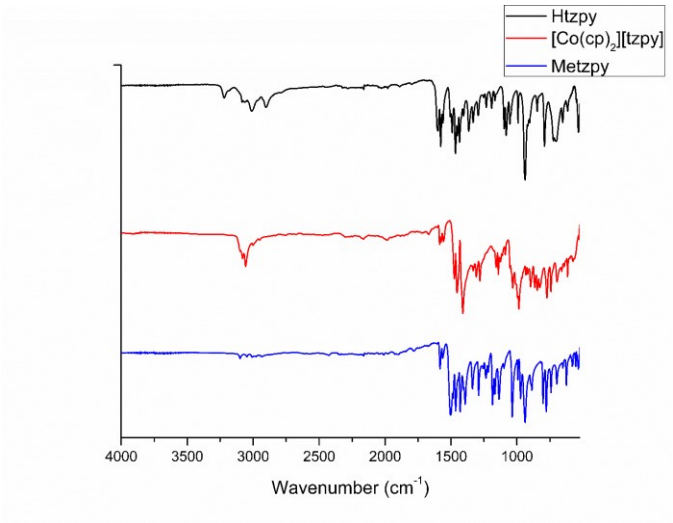

Figure 4.7. IR spectra for Htzpy, $[Co(cp)_2][tzpy]$ and Metzpy

A simpler, alternative route to Metzpy that does not involve cobaltocene was also found. Instead of performing a methylation, nucleophilic substitution with methylhydrazine was employed on the same initial precursor for Htzpy (Scheme 4.4).

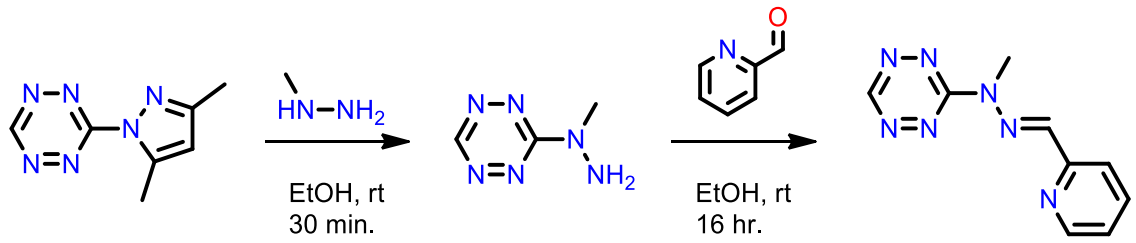

Scheme 4.4: Alternative synthesis of (2-pyridinylmethylidene)-3-(methylhydrazinyl)-1,2,4,5-tetrazine (Metzpy).

4.8 Alternative Synthesis of Metzpy. To a stirred suspension of 3-(3,5-dimethyl-1H-pyrazol-1-yl)-1,2,4,5-tetrazine (0.726 g, 4.12 mmol) in EtOH (20 mL, 99%) was added methylhydrazine (0.216 mL, 4.12 mmol). Upon addition the reaction takes on a dark red colour. The reaction was allowed to stir for 30 minutes at room temperature. 2-pyridinecarboxaldehyde (0.392 mL, 4.12 mmol) was then added to the mixture. The reaction mixture continued to stir at room temperature for an additional 16 hours, during which a bright red precipitate slowly began to form. The mixture was then filtered, the solid was rinsed with EtOH, and dried under vacuum. Yield (41%, 0.360 g).

While this method of preparation for Metzpy does not require neat conditions and can done in a one-pot procedure the yield of Metzpy is not as high as the first method. This can be rationalized by the lack of selectivity of the nucleophilic substitution step with methylhydrazine. During the substitution two different products can form depending on whether the methylated or the non-methylated hydrazine nitrogen attacks the tetrazine ring (Scheme 4.5). Since Schiff bases can only form from

primary amines only the top product in Scheme 4.5 can react with the 2-pyridinecarboxaldehyde and subsequently precipitate out of solution.

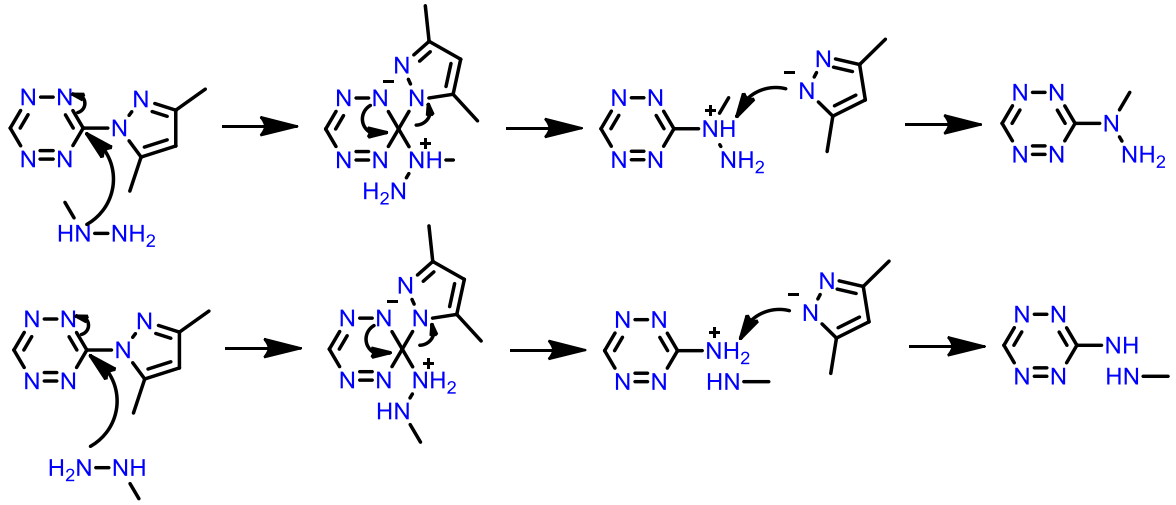

Scheme 4.5. S_NAr with methylhydrazine forming two different products.

4.9 Electrochemical Properties of Metzpy. After the successful selective methylation of the tzpy$^-$ structure at nitrogen N3 the electrochemical properties of Metzpy were then assessed. Cyclic voltammetry was performed in dry dichloromethane with 0.1 M tetrabutylammonium hexafluorophosphate as the supporting electrolyte (Figure 4.8). Upon reduction a quasi-reversible process was observed, indicating that the ligand Metzpy does confer stability to the generated anion radical. However since the redox couple lies at -1.42 V *vs.* ferrocene and the redox couple of cobaltocene lies at -1.33 V a stronger one-electron reducing agent than cobaltocene would be required to generate the radical species. Decamethylcobaltocene has its redox couple lie at -1.87 V *vs.* ferrocene,[6] and would therefore be a sufficiently powerful reducing agent for synthesizing the radical anion.

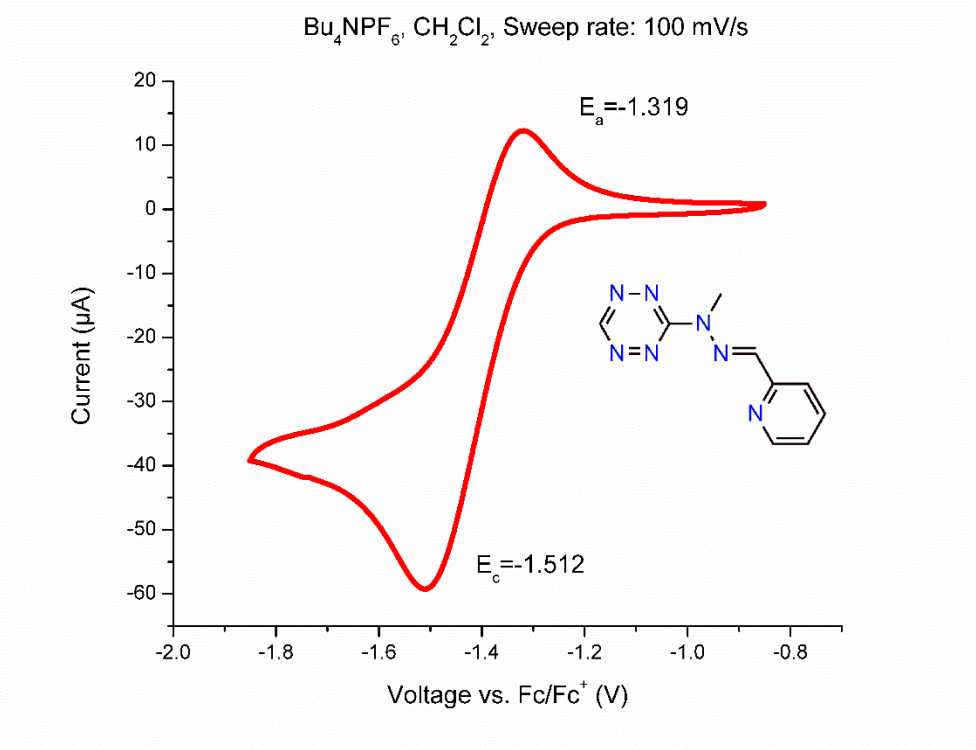

Figure 4.8. Cyclic voltammogram of Metzpy.

4.10 Conclusions. With this structural motif the ligand Metzpy can potentially be used to make nine-coordinate lanthanide complexes akin to the structures of White and coworkers.[7] The reversible reduction of the ligand Metzpy also gives rise to potential applications in photoredox catalysis upon making coordination complexes with Ru^{II}.[8] Ultimately, both the ligands Htzpy and Metzpy offer great opportunity for rich coordination chemistry for both lanthanides and transition metals and further work with these ligands should be explored. Work is currently being undertaken for coordinating both Htzpy and Metzpy to both transition metals and lanthanides. The work of Kimia Kojouri has already rendered several coordination complexes, with Figure 4.9 as just one example of the possibilities of these ligands.

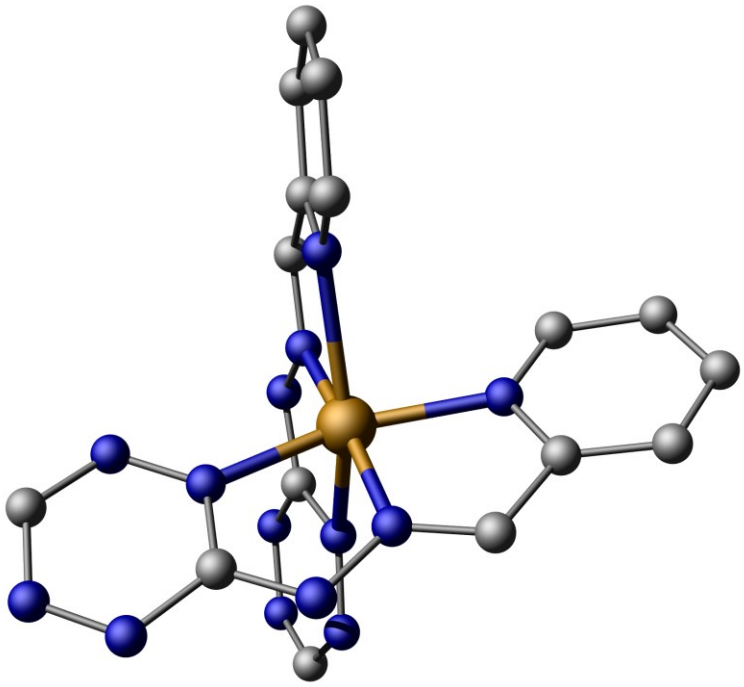

Figure 4.9. Crystal structure of $Cu(tzpy)_2$ taken with permission. Colour code: Orange (Cu), blue (N), Gray (C). Hydrogen atoms are omitted for clarity

4.11 References

1. (*a*) T. Woods, M. Ballesteros-Rivas, S. Ostrovsky, A. Palii, O. Reu, S. Klokishner and K. Dunbar, *Chem. Eur. J.*, 2015, **21**, 10302; (*b*) M. Schwach, H. Hausen and W. Kaim, *Inorg. Chem.*, 1999, **38**, 2242; (*c*) B. Sarkar, S. Frantz, W. Kaim and C. Duboc, *Dalton Trans.*, 2004, 3727; (*d*) S. Tripathy, M. van der Meer, A. Sahoo, P. Laha, N. Dehury, S. Plebst, B. Sarkar, K. Samanta and S. Patra, *Dalton Trans.*, 2016, **45**, 12532.
2. D. E. Chavez and M. A. Hiskey, *J. Heterocyclic Chem.*, 1998, **35**, 1329.
3. J. Aranzaes, M.-C. Daniel and D. Astruc, *Can. J. Chem.*, 2006, **84**, 288.
4. M. Antipin, R. Boese, N. Augart and G. Schmid, *Struct. Chem.*, 1993, **4**, 91.

5. K. Parimal, S. Vyas, C.-H. Chen, C. Hadad and A. Flood, *Inorg. Chim. Acta*, 2011, **374**, 620.

6. J. Aranzaes, M.-C. Daniel and D. Astruc, *Can. J. Chem.*, 2006, **84**, 288.

7. L. Semenova, A. Sobolev, B. Skelton and A. White, *Aust. J. Chem.*, 1999, **52**, 519.

8. J. Narayanam and C. Stephenson, *Chem. Soc. Rev.*, 2011, **40**, 102.

Concluding Statement:

The incorporation of tetrazines into Schiff base ligands brings forth a whole new way to explore the radical exchange coupling with metal complexes. While a tetrazine radical complex was not obtained in this work there is still great promise for these types of ligands to generate polynuclear lanthanide complexes with reduced or non-reduced tetrazines. Even without the presence of a tetrazine anion radical the tetranuclear Dy^{III} complex in this work exhibited substantial magnetic properties in the form of ferromagnetic interactions and an energy barrier of 158 K. By small alterations in the reaction conditions various lanthanide complexes can also be formed like in the examples of the **Dy_2** and **Dy_8** complexes. The Metzpy ligand shows potential for stable radical complexes with its quasi-reversible reduction process. The structure of this ligand will likely result in the formation of both nine-coordinate lanthanide and six-coordinate transition metal complexes. In conclusion, I hope that this work has brought insight towards the role of tetrazines in the field of molecular magnetism and that this work can be explored further in the pursuit of high-performance Single-Molecule Magnets.